Technische Universität München
Institut für Energietechnik

Lehrstuhl für Thermodynamik

# Radiation from High Pressure Hydrogen-Oxygen Flames and its Use in Assessing Rocket Combustion Instability

**Thomas Fiala**

Vollständiger Abdruck der von der Fakultät für Maschinenwesen der Technischen Universität München zur Erlangung des akademischen Grades eines

DOKTOR – INGENIEURS

genehmigten Dissertation.

Vorsitzender:
Univ.-Prof. Dr.-Ing. Oskar J. Haidn
Prüfer der Dissertation:
1. Univ.-Prof. Dr.-Ing. Thomas Sattelmayer
2. Univ.-Prof. Dr. rer. nat. Michael Oschwald
Rheinisch-Westfälische Technische Hochschule Aachen

Die Dissertation wurde am 17.03.2015 bei der Technischen Universität München eingereicht und durch die Fakultät für Maschinenwesen am 25.06.2015 angenommen.

# Vorwort

Die vorliegende Arbeit entstand während meiner Tätigkeit am Lehrstuhl für Thermodynamik der Technischen Universität München. Sie wurde von der Deutschen Forschungsgemeinschaft (DFG) im Rahmen des Sonderforschungsbereichs Transregio 40 ideell und finanziell gefördert.

Ich bedanke mich herzlich bei Prof. Dr.-Ing. Thomas Sattelmayer für die Betreuung der Arbeit und die Übernahme des Hauptreferats. Ich schätze das mir entgegengebrachte Vertrauen und die Freiheit, die er mir bei der Ausgestaltung und Bearbeitung der Projektziele ließ, sehr. Gleichzeitig gaben mir die engagierten Besprechungen immer die entscheidenden Impulse und halfen mir, nie den Fokus aus den Augen zu verlieren. Darüber hinaus bedanke ich mich für die spannende und lehrreiche Möglichkeit, die Lehrveranstaltung Thermodynamik I als Zentralübungsleiter betreuen und koordinieren zu dürfen.

Prof. Dr. rer. nat. Michael Oschwald danke ich besonders für die Übernahme des Koreferats, aber auch für die stets hilfreichen und motivierenden Projekttreffen. Für den Vorsitz in der Prüfungskommission möchte ich Prof. Dr.-Ing. Oskar Haidn meinen Dank aussprechen.

Die Zeit am Lehrstuhl für Thermodynamik war vor allem aufgrund der freundschaftlichen Atmosphäre unter den Kollegen so angenehm und produktiv. Zusammen mit meinen Bürokollegen Moritz Bruder M.Sc., Dr.-Ing. Patrick Dems, Dr.-Ing. Christoph Jörg und Dipl.-Ing. Wolfram Ullrich konnte ich viele kleine Herausforderungen schnell und unkompliziert lösen. In der kreativen Raumfahrt-Gruppe am Lehrstuhl bestehend aus Dr.-Ing. Robert Kathan, Dr.-Ing. Daniel Morgenweck, Dr.-Ing. Martin Schmid, Dipl.-Ing. Moritz Schulze und Dipl.-Ing. Attila Török sowie mein Projektpartner Dipl.-Ing. Stefan Gröning vom DLR Lampoldshausen war immer Zeit für hilfreiche Diskussionen und konstruktives Feedback. Die Hilfe von Dipl.-Ing. Lorenz Böck war besonders beim Betrieb des LIF-Lasers unerlässlich, ohne ihn hätte ich wohl keine TDLAS-Messungen durchgeführt. Ihnen allen und ebenso allen nichtgenannten Kollegen danke ich für die schöne Zeit am Lehrstuhl.

Bei Prof. William Anderson Ph.D. wie auch bei allen Organisatoren des Sonderforschungsbereichs bedanke ich mich für die Möglichkeit, einen Monat an der Purdue University zu verbringen.

Abschließend danke ich von ganzem Herzen meiner Familie, insbesondere meiner Frau und meinen Eltern für ihre unermüdliche Unterstützung.

München, im Juli 2015

Thomas Fiala

## Abstract

Visible and ultraviolet radiation is a readily measurable property of a flame. This study investigates the radiation of non-premixed hydrogen-oxygen flames at elevated pressure, which often power liquid rocket engines. Such flames mainly emit UV radiation from excited OH* radicals and exhibit a broad-band radiation peaking in the blue spectrum. Both types of radiation are examined experimentally and numerically in a laminar jet flame at pressures ranging from 1 bar to 40 bar. Emission and absorption are measured spectrally and spatially. Physical models for numerically simulating either radiation are summarized and extended by new methods. Their practical use and limitations are assessed by comparison with experimental data. Especially the difference between chemical an thermal excitation of OH* as well as its self-absorption are scrutinized. Additionally, the radiation is compared to the volumetric heat release rate, which is an important parameter in studying combustion instabilities. Generally, both quantities are found to be quantitatively uncorrelated for non-premixed flames. Studies of counterflow flame ensembles reveal that in coarsely resolved turbulent flames with low optical density, a qualitative relation between line-of-sight integrated radiation and heat release rate exists. To quantitatively measure heat release rate, radiation measurements must be corrected for the influence of flame straining. Due to this fact, alternate methods are presented to assess combustion instabilities by radiation data.

## Kurzfassung

Die sichtbare und ultraviolette Strahlung ist eine einfach messbare Kenngröße von Flammen. Diese Studie behandelt die Strahlung von nicht vorgemischten Wasserstoff-Sauerstoff-Flammen unter hohem Druck, welche häufig Flüssigkeitsraketen antreiben. Solche Flammen emittieren UV-Strahlung des angeregten OH*-Radikals sowie eine breitbandige Strahlung im blauen Spektrum. Beide Arten werden sowohl experimentell als auch numerisch anhand einer laminaren Strahlflamme zwischen 1 bar und 40 bar untersucht. Die Emission und die Absorption der Strahlungen werden spektral und räumlich aufgelöst vermessen. Zur numerischen Simulation der Strahlung werden physikalische Modelle aus der Literatur zusammengetragen und um neue Methoden erweitert. Durch Vergleich mit Messwerten werden die Möglichkeiten und Grenzen der Modelle beurteilt. Insbesondere wird auf den Unterschied der chemischen und thermischen Anregung des OH*-Radikals und die Selbstabsorption der OH*-Strahlung eingegangen. Außerdem wird die Strahlung mit der volumetrischen Wärmefreisetzungsrate verglichen, welche für die Untersuchung von Verbrennungsinstabilitäten wichtig ist. Im Allgemeinen existiert keine quantitative Korrelation zwischen beiden Größen. In grob aufgelösten turbulenten Flammen mit geringer optischer Dichte hängt

die linienintegrierte Flammenstrahlung qualitativ mit der Wärmefreisetzungsrate zusammen. Um quantitativ die Wärmefreisetzungsrate zu messen, ist zusätzlich zu Strahlungsmessungen die Bestimmung der Flammenstreckungsratenverteilung notwendig. Aus diesem Grund werden weitere Möglichkeiten vorgestellt, Flammenstrahlung zur Beurteilung von Verbrennungsinstabilität zu verwenden.

# Contents

# List of Figures

# List of Tables

# Nomenclature

**Latin Characters**

| | |
|---|---|
| $A$ | Einstein coefficient of emission [ $kmol^n/s$ ] |
| $A$ | Arrhenius pre-exponential factor [ $1/s$ ] |
| $a$ | Strain rate [ $1/s$ ] |
| $B$ | Einstein coefficient of absorption [ $1/s$ ] |
| $c$ | Speed of light [ $m/s$ ] |
| $c_f$ | Correlation factor [ $W/kmol$ ] |
| $d_c$ | Lance inner diameter [ $m$ ] |
| $e$ | Emission coefficient [ $W/m^3/sr$ ] |
| $e_\lambda$ | Spectral emission coefficient [ $W/m^3/sr$ ] |
| $E$ | Energy [ $J$ ] |
| $E_a$ | Arrhenius activation energy [ $J/kmol$ ] |
| $Fr$ | Froude number [—] |
| $g$ | Gravity of earth [ $m/s^2$ ] |
| $\tilde{g}$ | Degeneracy [—] |
| $g_m^\ominus$ | Standard-state molar Gibbs energy [ $J/kmol$ ] |
| $h$ | Planck constant [ $J\,s$ ] |
| $h$ | Specific Enthalpy [ $J/kg$ ] |
| $k$ | Absorption coefficient [ $1/m$ ] |
| $k_\lambda$ | Spectral absorption coefficient [ $1/m^2$ ] |
| $k$ | Reaction rate [ $kmol^n/s$ ] |
| $k_B$ | Boltzmann constant [ $J/K$ ] |
| $K$ | Equilibrium constant [ $kmol^n$ ] |
| $l$ | Luminous flame length [ $m$ ] |
| $L$ | Radiance [ $W/m^2/sr$ ] |
| $L_\lambda$ | Spectral radiance [ $W/m^3/sr$ ] |
| $M$ | Molar mass [ $kg/kmol$ ] |
| $\dot{m}$ | Mass flow rate [ $kg/s$ ] |
| $\mathring{m}$ | Mass flux [ $kg/m^2/s$ ] |
| $n$ | Index of refraction [—] |
| $n$ | Arrhenius temperature exponent [—] |
| $\vec{n}$ | Normal vector [—] |

| | |
|---|---|
| $N$ | Number of molecules [–] |
| $N$ | Number of flamelets [–] |
| $p$ | Pressure [ Pa ] |
| $Q$ | Quantum efficiency of the detector [–] |
| $\dot{q}$ | Volumetric heat release rate [W/m$^3$/K] |
| $r$ | Radial coordinate [ m ] |
| $Re$ | Reynolds number [–] |
| $R_m$ | Gas constant [ J/kmol/K ] |
| $s$ | Location [ m ] |
| $T$ | Temperature [ K ] |
| $u$ | Velocity [ m/s ] |
| $v$ | Vibrational quantum number [–] |
| $x$ | Coordinate [ m ] |
| $X$ | Mole fraction [kmol/kmol] |
| $Y$ | Mass fraction [kg/kg] |
| $z$ | Coordinate [ m ] |

**Greek Characters**

| | |
|---|---|
| $\delta$ | Cell width [ m ] |
| $\delta$ | Flame thickness [ m ] |
| $\Lambda$ | Radial pressure curvature [ N/m$^4$ ] |
| $\lambda$ | Wavelength [ m ] |
| $\mu$ | Dynamic viscosity [ Pa s ] |
| $\nu$ | Kinematic viscosity [ m$^2$/s ] |
| $\nu$ | Frequency [ Hz ] |
| $\bar{\nu}$ | Spectroscopic wave number [ 1/cm ] |
| $\rho$ | Density [ kg/m$^3$ ] |
| $\sigma_\lambda$ | Spectral scattering tensor [ 1/m$^2$ ] |
| $\tau$ | Transmittance [–] |
| $\tau_\lambda$ | Spectral transmittance [1/m] |
| $\dot{\omega}_m$ | Molar volumetric production rate [ kmol/m$^3$/s ] |

**Subscripts**

| | |
|---|---|
| $_\lambda$ | Spectral quantity [ …/m ] |
| $_{ad}$ | Adiabatic |
| $_{air}$ | In air |
| $_c$ | center |
| $_{ch}$ | Chemical excitation |
| $_{diss}$ | Dissociation |
| $_f$ | Fuel |

| | |
|---|---|
| $_{LoS}$ | Line of Sight |
| $_{o}$ | Oxidizer |
| $_{Q}$ | Quenching |
| $_{th}$ | Thermal excitation |
| $_{vac}$ | In vacuum |

**Superscrips**

| | |
|---|---|
| $^{*}$ | Excited molecule |

**Operators**

| | |
|---|---|
| [M] | Concentration of molecule M [ kmol/m$^3$ ] |
| $\overline{\phantom{x}}$ | Ensemble averaging |
| $_{f}$ | Flamelet integration |

**Abbreviations**

| | |
|---|---|
| DC | Detailed Chemistry Radiation Model |
| EFRM | Equilibrium Filtered Radiation Model |
| FFT | Fast Fourier Transform |
| FWHM | Full Width at Half Maximum |
| IR | Infra-red |
| LIF | Laser Induced Fluorescence |
| PIV | Particle Image Velocimetry |
| SM | Spectral Modeling |
| TDLAS | Tunable Dye Laser Absorption Spectroscopy |
| UV | Ultra-violet |

# 1. Introduction

The investigation of combustion processes is challenging. The extreme temperatures reached within flames form a hostile environment, which often prohibits conventional mechanic measurement techniques. Therefore, non-invasive optical techniques like Particle Image Velocimetry (PIV), Laser Induced Fluorescence (LIF), or Schlieren are frequently applied in combustion diagnostics. However, also these techniques require a certain instrumentational effort, which, in some situations, is unfeasible.

Such a case is the combustion in liquid rocket engines: The temperatures reached by typical fuel-oxidizer combinations are hazardous to every solid material. Besides withstanding the thermal loads, the combustion chamber walls also have to resist high pressures. Access to the flame for lasers or other illumination is hard to achieve.

A parameter by comparison readily obtainable from a flame is its own radiation. Flames show a distinct spectrum which yields a variety of information. Furthermore, radiation is a property naturally originating from flames, thus its measurement truly is non-invasive. The use of small optical fibers can provide sufficient optical access to poorly accessible flames.

However, the measurement of flame radiation has two disadvantages: First, it is a line-of-sight integrated measurement. Local measurements are not directly possible but require complicated post-processing. Self-absorption, i.e. the absorption of flame radiation by the flame itself, further increases complexity. The rear end of the line of sight, usually the wall of the combustion chamber, can glow and distort the measurement. Second and more importantly, radiation is a quantity not directly associated with a single thermodynamic property. This heavily reduces the physical significance of its measurement and allows for a great possibility of interpretation.

A field of study where flame radiation is often measured is combustion instability. Being the most important subset of general thermo-acoustic instability, combustion instability describes the interaction between acoustics and heat release by combustion. Oscillating combustion results in locally fluctuating density which can be interpreted as an acoustic source. The acoustic field, physically expressed by pressure and density fluctuations, can influence the combustion process itself. This represents a closed feedback loop which can result in very high sound pressure levels. This phenomenon can be employed to enhance heat transfer, but in most cases it should be avoided. The resulting combustion noise typically is undesirable.

The high sound pressure levels can induce unwanted vibrations of the device. However, the technically most dangerous effect is the enhanced heat transfer, which can result in thermal loads exceeding the design specifications.

The latter is particularly important in liquid rocket combustion [61, 124]. In spacecraft engines, security margins are very small. Combustion instability can lead to pressure oscillations up to several bar peak-to-peak amplitude, resulting in an enormous stress of the combustion chamber. The extreme temperatures reached in rocket propulsion cannot be sustained by any material. An effective cooling is crucial. Even so, the wall temperatures of the combustion chamber are close to the maximum technically achievable values. The increase in heat transfer produced by combustion instability can lead to failure of the engine, and further to failure of the entire mission and loss of both rocket and payload.

This problem has occurred ever since the development of liquid rockets, starting off with the A-4 engine in the late 1930s [138]. During the space race, both American and Russian rockets faced this problem. The development of the F-1 engine for the Saturn V rocket required more than 2000 full-scale tests to reach flight qualification [145]. The Aestus upper stage engine of the Ariane 5 rocket failed during flight 142 due to combustion instability, which caused the mission to miss the desired orbit.

It is evident that combustion instability is a major threat for liquid rockets. To minimize expensive and time-consuming full-scale testing, this phenomenon should be included early in the design process, favorably using engineering approaches or numerical simulations. However, the underlying physics are too complicated and minor modifications have too large an impact on the acoustics such that crude engineering methods are not suitable. Numerical tools available today for predicting stability are neither accurate nor efficient enough for industrial applications. Especially the interaction between the acoustic field and the combustion process is not yet fully understood. This implies a major uncertainty in combustion instability modeling. To resolve this problem, experimental studies are necessary.

The models describing the interaction between combustion and acoustics are mostly based on the Rayleigh criterion. The Rayleigh criterion states that a fluctuating heat release can drive the acoustic field if the heat release is in phase with the acoustic pressure fluctuation. To investigate this interaction experimentally, both the pressure field and the heat release fluctuations have to be measured [102].

In combustion, heat is added to the flow by exothermic combustion processes. The local volumetric heat release rate $\dot{q}$ is a property defined theoretically and cannot be measured directly. It is only possible to obtain it indirectly using the first law of thermodynamics by measuring the exact flow velocities, temperature, pressure, and species concentrations [81]. This task is not achievable in most situations.

Instead, the flame radiation, particularly OH* and CH* chemiluminescence, has of-

ten been used as a marker for the heat release rate. However, most studies investigating such a correlation have been applied to premixed combustion of hydrocarbons at moderate pressures and temperatures. Non-premixed flames at high pressure and temperature levels have not been scrutinized in this respect. Hydrogen-oxygen flames, which often power rocket combustion due to the high efficiency of this fuel-oxidizer combination, in addition burn at such high temperatures that radiating radicals are thermally excited. The direct applicability of results from literature, in which chemical excitation is the source of radiation, is, therefore, questionable.

## 1.1. Scope of this Thesis and Overview

The scope of this work is on the radiation of non-premixed hydrogen-oxygen flames at elevated pressures. To assess combustion instability, its use in determining the volumetric heat release rate is of particular interest. However, the focus of this thesis is not restricted to just this correlation. In the course of study it was found that the knowledge on radiation from high pressure hydrogen flames is sparse. This thesis is, therefore, broadened to summarize and extend the general knowledge on hydrogen flame radiation and its simulation.

Infrared emission is excluded from this study. While important for heat transfer, it is unsuitable for flame measurement due to its interference with thermal background radiation from hot walls, the significant and complex self-absorption, and measurement difficulties. Instead, this thesis focuses on radiation in the visible and ultraviolet (UV) range. In hydrogen-oxygen flames, the two dominant sources of radiation are the excited hydroxyl radical (OH*), which shows a typical band spectrum in the UV, and a yet unexplored radiation, which leads to a continuous spectrum peaking at 430 nm. The latter is commonly referred to as the *continuous* or the *blue* radiation of hydrogen flames.

Radiation of flames has been studied over a long time and much knowledge is already available in this field. Therefore, the objective is first approached by an extensive literature review presented in Chapter 2. Compared to common flames, combustion of hydrogen with oxygen in liquid rockets has specific features because of the high temperature and pressure levels. The difference from common flames is carved out and results from literature are assessed accordingly.

The physical flame radiation is studied in a lab-scale, laminar, hydrogen-oxygen jet flame experiment. It is operated at pressures up to 40 bar to approximate the conditions in practical rocket combustion. The design of the experiment as well as the operating parameters and measurement devices are described in Chapter 3. This chapter also features the accompanying numerical simulations. A laminar setup is chosen for the experimental investigation, because it yields a better insight into the radiation physics and additionally can be simulated reliably.

In Chapters 4 and 5, the experimentally observed spectra, transmittances, and radiances of the OH* radiation and the blue radiation are presented. To understand the underlying physical processes, these data are compared to the results from the numerical simulations. A specific focus of this thesis is placed on the modeling of the radiation, which can be the basis for future work. For OH*, different models are analyzed and their usability with respect to liquid rocket combustion is discussed. Up to now, the origin of the blue radiation is not known. Chapter 5 attempts to provide further evidence on this topic.

The relation between heat release and the types of radiation is discussed in Chapter 6. As the heat release can hardly be accurately measured in experiments, the analysis is purely based on numerical observations. The comparison is first made on the laminar level already described in the previous chapters. However, combustion in liquid rocket engines is always highly turbulent. Nevertheless, it is known to have flamelet character, which implies that the turbulent flame consists of ensembles of laminar counterflow flames. The findings on the laminar level, therefore, still hold on the fundamental level. By evaluating stochastic counterflow flame ensembles, the results from laminar flames are transferred to turbulent combustion.

The thesis will be concluded by a summary in Chapter 7, condensing the key findings of this thesis.

# 2. Fundamentals of Flame Radiation

The most familiar type of visible flame radiation probably is that of paraffin candles (see Figure 2.1). In the visible range, candles emit two dominant types of radiation: The blue center-near emission is due to chemiluminescence of the excited methylidyne radical CH*. The broader yellow radiation originates from hot soot, which consists of unburnt carbon particles still present due to incomplete combustion. In addition, all hydrocarbon flames emit a broad band variety of less intense continuous spectra from the UV to the infra-red due to the vast number of species existing in the flame zone.

**Figure 2.1.:** A paraffin candle flame.

Hydrogen-oxygen flames, in contrast, show a very different spectrum. Lacking any carbon atoms, both CH* chemiluminescence and soot are not observable. The number of different molecules within the flame is limited, as they may contain only hydrogen and oxygen atoms. The spectrum of hydrogen flames is, therefore, much less complex. It is dominated by the hydroxyl (OH) system in the UV, a broad-band continuum in the visible, and radiation originating from vibrational excitation of water vapor and OH in the near infra-red. Additionally, the Schumann-Runge bands of $O_2$ are present in the deep UV. If present, nitrogen impurities can result in a yellow-green continuum. A comprehensive review on the radiation from hydrogen flames can be found in the books by Gaydon [49] or Mavrodineanu and Boiteux [92].

To clarify the physical terms and assumptions used later on in this thesis, the fundamentals of radiation transfer and flame spectroscopy are briefly summarized in this chapter. The two main sources of radiation in the visible and UV, the OH* radiation and the blue continuum, are reviewed in detail. The literature available on the relation between radiation and the heat release rate is analyzed at the end of this chapter.

## 2.1. Radiation Transfer

The transfer of mono-chromatic radiation is best described by the radiative transfer equation [95, 96]:

$$\frac{1}{c}\frac{\partial L_\lambda(\vec{s})}{\partial t} + \vec{n}\cdot\nabla L_\lambda(\vec{s}) = -(k_\lambda(\vec{s})+\sigma_\lambda(\vec{s}))\ L_\lambda(\vec{s}) + e_\lambda(\vec{s}) \tag{2.1}$$

This equation describes the radiation by its spectral radiance $L_\lambda$, which is the radiant flux per solid angle, illuminated area, and wavelength. The equation shows a total derivative (divided by the speed of light) on the left hand side. However, the spreading of the radiation is at the speed of light. Typically, engineering timescales are much larger than the time required for the radiation to spread. The phenomenon is, therefore, assumed to be quasi-stationary and the unsteady term is commonly neglected. The right hand side yields three phenomenological mechanisms by which the radiance can be influenced: It can be attenuated with a spectral absorption coefficient $k_\lambda$. The spectral emissivity $e_\lambda$ represents a source term for the radiance. Finally, the radiance can be scattered by the spectral scattering cross-section $\sigma_\lambda$, which can also be a source term along a certain direction if radiation is scattered from other directions.

Typically, the radiation is approximated to follow the laws of geometrical optics. Here, the radiation is assumed to propagate along straight rays, each of them showing a quasi-one-dimensional character (see Figure 2.2).

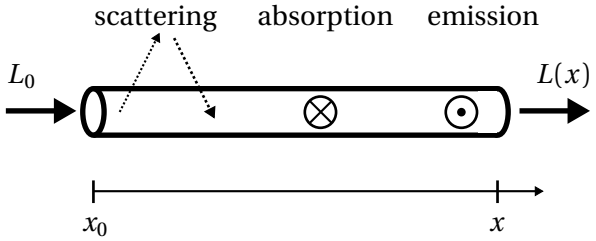


**Figure 2.2.:** Illustration of the processes relevant for radiation transfer.

If only transport along a quasi-one-dimensional ray is considered, scattering is neglected (which is justified in molecular gases, see [96]), and the system is assumed to be steady with respect to the radiative time scale, the above equation can be reduced to [10]:

$$\frac{d\,L_\lambda(x)}{d\,x} = -k_\lambda(x)\ L_\lambda(x) + e_\lambda(x) \tag{2.2}$$

If absorption is neglected, i.e. $k_\lambda(x)$ approaches 0, Equation (2.2) can be solved by integration:

$$L_\lambda(x) = \int_{x_0}^{x} e_\lambda(\xi)\,d\,\xi + L_{\lambda,0} \tag{2.3}$$

Inversely, if only absorption would be considered in the above equation, i.e. $e_\lambda(x) = 0$, it becomes a homogeneous first-order differential equation. Its solution is:

$$L_\lambda(x) = L_{\lambda,0} \exp\left(-\int_{x_0}^{x} k_\lambda(\xi)\, d\xi\right) \tag{2.4}$$

which is a general form of the well-known Lambert-Beer law. By reshaping this equation, the spectral transmittance $\tau_\lambda$ is defined:

$$\tau_\lambda = \frac{L_\lambda(x)}{L_{\lambda,0}} = \exp\left(-\int_{x_0}^{x} k_\lambda(\xi)\, d\xi\right) \tag{2.5}$$

The transmittance represents the fraction of radiation which is transmitted through a field. It is a dimensionless property and simple to measure quantitatively. The transmittance is related to the absorption coefficient $k$ just by geometry. Therefore, if the geometry is known, quantitative measurements of the absorption coefficient are possible.

By taking the natural logarithm of Equation (2.5) and multiplying it by $-1$, the equation can be further transformed into:

$$-\ln(\tau_\lambda) = \int_{x_0}^{x} k_\lambda(\xi)\, d\xi \tag{2.6}$$

This equation shows a very similar form to Equation (2.3). Their simple spatial integrations on the right hand sides are the fundamental assumption for state-of-the-art reconstruction techniques like standard Abel transformations, which will be used in Chapters 4, 5, and 6.

If both emission and absorption are important, the general solution of Equation (2.2) is more complicated [10, 94]:

$$L_\lambda(x) = \int_{x_0}^{x} e_\lambda(\xi) \exp\left(-\int_{\xi}^{x} k(\zeta)\, d\zeta\right) d\xi \tag{2.7}$$

$$+ L_{\lambda,0} \exp\left(-\int_{x_0}^{x} k(\zeta)\, d\zeta\right)$$

This general case applies for flame radiation with significant self-absorption, like the OH* radiation in this study. The solution of Equation (2.7) will be addressed in Section 3.5.

### 2.1.1. Total Quantities

Up to this point, all radiometric quantities have been discussed for monochromatic radiation, i.e. radiation at a single wavelength. Practical measurement devices like

digital cameras or photo diodes cannot detect these directly, but instead always register the radiation over a certain wavelength band. These *total quantities* are obtained by multiplying the spectral quantities with the quantum efficiency of the detector $Q(\lambda)$, which is a function of the wavelength. Additionally, if an optical filter or other components with a wavelength-dependent transmittance $\tau_F(\lambda)$ (or, for a mirror, a corresponding wavelength-dependent reflection factor) are used, their effects are also contained. The mathematical representation of this operation is a simple integration [96]:

$$L = \int_0^\infty \tau_F(\lambda)\, Q(\lambda)\, L_\lambda(\lambda)\, d\lambda \tag{2.8}$$

This operation is always performed when converting the radiance into the measured signal. Before this step, within the media the radiation is passing through, the wavelength-dependent equations described previously still hold.

The above integration collapses the wavelength-dependent data onto a single value. If both emissivities and absorption coefficients within the investigated volumes are not functions of wavelength with respect to the filtered band, they do not carry additional information. In this case, all the above formulas are applicable to the total quantities by just removing the index $_\lambda$. However, if either the emissivities or the absorption coefficients depend on the wavelength, this detailed information is lost and cannot be recovered afterwards. It is evident that a band-pass filtered measurement of the flame radiation can only give the information if the flame is radiating somewhere within the pass band of the filter, but not what the spectrum looks like.

At least, for measurements of just emission (without self-absorption), this problem is often not severe, as the integrations can be interchanged. If no background illumination is present ($L_0 = 0$), the recorded radiance is defined as

$$\begin{aligned} L(x) &= \int_0^\infty \tau_F(\lambda)\, Q(\lambda) \int_{x_0}^x e_\lambda(\lambda,\xi)\, d\xi\, d\lambda \\ &= \int_{x_0}^x \int_0^\infty \tau_F(\lambda)\, Q(\lambda)\, e_\lambda(\lambda,\xi)\, d\lambda\, d\xi \\ &= \int_{x_0}^x e(\xi)\, d\xi \end{aligned} \tag{2.9}$$

where $e$ now represents the emissivity integrated in the same way as the overall radiance $L$ in Equation (2.8).

For pure absorption measurements (without emission), the integration over wavelength has to be done based on the radiances that are compared. This yields a new

definition of the transmittance $\tau$:

$$\tau = \frac{L}{L_0} = \frac{\int_0^\infty L_{\lambda,0}(\lambda) \cdot \exp\left(-\int_{x_0}^{x} \tau_\mathrm{F}(\lambda)\, Q(\lambda)\, k_\lambda(\xi)\, d\xi\right)\, d\lambda}{\int_0^\infty \tau_\mathrm{F}(\lambda)\, Q(\lambda)\, L_{\lambda,0}(\lambda)\, d\lambda} \tag{2.10}$$

It is important to notice that the transmittance $\tau$ now does not just depend on the optical filter curve and the quantum efficiency of the detector, but also on the spectrum of the background radiance $L_{\lambda,0}$. Thus, the interpretation of the transmittance $\tau$ obtained from measurements using an arbitrary or complex background spectrum is difficult. However, two special cases are of particular interest:

- The illumination light source exhibits a single narrow peak: This is the fundamental assumption in Tunable Dye Laser Absorption Spectroscopy (TDLAS), where the background light source is a narrow-band tunable dye laser. If the width of the peak is smaller than the variations in the absorption spectrum, then the transmittance is $\tau = \tau_\lambda\ \lambda_\mathrm{Laser}$.
- The spectrum of the illumination light source is non-zero over the wavelength within the measured wavelength band, and no total absorption is observed: This implies that the investigated medium does not absorb radiation in the measured wavelength band at any wavelength.

If both emission and absorption are wavelength-dependent and non-zero within the recorded wavelength band, no unambiguous information can be extracted from measurements. Instead, all deductions rely on assumptions. A distinct evidence of wavelength-varying emission or absorption is only possible with measurements that fully resolve the spectrum.

## 2.2. Flame Spectra

Flames can be well characterized by their emission or absorption spectra. These are defined by the distributions of the emitted or absorbed radiance as a function of wavelength $\lambda$.[1]

To understand the origin or the absorption of radiation within flames, it is advantageous to not consider the radiation as a wave phenomenon but rather as a particle phenomenon. From this point of view, each single wavelength can be attributed to a stream of photons, each having the energy[2]:

$$E_\mathrm{Photon} = h\ \nu = \frac{h\ c}{\lambda} \tag{2.11}$$

[1] In literature, also the spectroscopic wavenumber $\tilde{\nu} = 1/\lambda$ in $\mathrm{cm}^{-1}$ or the frequency $\nu = c/\lambda$ in Hz is sometimes used.

[2] Note that the wavelength $\lambda$ varies with the speed of light $c$ for a given energy $E_\mathrm{Photon}$.

The approach to treat the radiation as a particle phenomenon is especially helpful when describing the interaction between radiation and matter.

In gaseous flames, the substance that interacts with radiation typically consists of single separated molecules (an exception being soot, which is not considered in this work). Radiation from flames is thus a sub-division of molecular spectroscopy.

A photon can be produced by the state change of a molecule from a higher energy (or ionized or dissociated) state $j$ to a lower energy state $i$. The energy difference $\Delta E_{j-i}$ between the higher and lower states $j$ and $i$ corresponds exactly to the energy $E_{\text{Photon}}$ of the photon. Inversely, a photon can be absorbed by a molecule by raising its energy level by the energy of the photon.

From quantum theory, a regular (un-ionized and non-dissociated) molecule or atom can only occupy discrete energy states. Each state is characterized by its electronic, vibrational, rotational, and spin quantum numbers. A molecule can transition from a higher energy state $i$ to a lower energy state $j$ spontaneously, if it is not forbidden by the selection rules of quantum mechanics. The probability of such a transition is known as the Einstein coefficient $A_{i\rightarrow j}$ [96]. The Einstein coefficient is a constant for each transition and not a function of temperature or pressure [4].

The pure emission spectrum (without self-absorption) is defined by these Einstein coefficients and the number densities of the excited states. In thermal equilibrium, the number density of the molecular states is defined by the equilibrium temperature. Thermal equilibrium is reached by collisions of the molecules. It typically takes $10^1$ collisions to reach translational equilibrium (i.e. the velocities of the molecules are distributed according to Maxwell's distribution), $10^3$ collisions to reach equilibrium between the rotational states, $10^5$ collisions for the vibrational, and $10^7$ collisions for the electronic states [92]. Thermal equilibrium is reached faster the shorter the mean free time is, which is proportional to $1/(p\sqrt{T})$. At high temperatures and pressures, thermal equilibrium often is a good assumption.

If a system is thermalized, the temperature is known, and the Einstein coefficients are tabulated, then the emission spectrum of a molecule can be calculated. There exist several computer softwares for this purpose, such as HITRAN/HITEMP [121], LIFBASE [90], SpectralCalc [43], or LASKIN [14].

### 2.2.1. Line Shapes

Even though the radiation of a line is attributed to a specific transition between states with an exact energy difference, it is not exactly mono-frequent. Instead, each spectral line is broadened by two effects: *Doppler* and *lifetime broadening* [4]. The first is due to the translational motion of the molecules and, therefore, a function of the (translational) temperature. Depending on the velocity between the observer

and the emitting molecule, the frequency of the radiation is Doppler shifted. As the Brownian motion of the molecules is isotropic, this effect cancels out on average, resulting in the exact mean wavelength. However, the radiation now shows a distribution over the wavelength. In wavenumber space[3], the distribution follows a Gaußian profile [4].

Lifetime broadening originates from the uncertainty principle, which relates the energy uncertainty $\delta E_{\text{Photon}}$ to the lifetime $\tau_{\text{Lifetime}}$ of the excited state:

$$\delta E_{\text{Photon}} \sim \frac{h/(2\,\pi)}{\tau_{\text{Lifetime}}} \tag{2.12}$$

The effective lifetime is determined by two effects: The natural lifetime and the collisional lifetime. The natural lifetime is constant over temperature and pressure and typically of the order of $10^{-8}$ s for an electronic excited state [4][4]. This is much longer than the ordinary lifetime reduction induced by collisions. As the number of collision increases with pressure, the mean time between collisions is reduced and the linewidth is increased. This type of broadening is, therefore, often also referred to as pressure broadening. The distribution in wavenumber space is a Lorentz or Breit-Wiegner profile [4].

In flames above 3000 K and at elevated pressures, both Doppler and pressure broadening are significant. The effects can be combined into a Voigt profile in wavenumber space [4, 120]. When simulating spectra, numerical routines for computing this distribution can be applied (see Section 4.1.3)

### 2.2.2. Absorption Spectrum

Flames do not only emit radiation, but also absorb it. An example is a candle in direct sunlight, which throws a shade. Photons can be absorbed by molecules by the reverse process to emission. For molecules with discrete energy states, only photons matching the energy of the allowed transitions can be absorbed. If the flame is illuminated by a broad-band light source, the characteristic absorption spectrum can be observed.

The wavelength-dependent absorption coefficient $k_\lambda$ again depends on a corresponding transition probability, known as the Einstein coefficient $B_{i\rightarrow j}$, as well as the number density of molecules in the corresponding ground state. The absorption spectrum is, therefore, qualitatively similar to the emission spectrum for a single molecule. The computer softwares mentioned before are capable of computing them as well.

[3] This is the reason why spectral modeling typically is performed in wavenumber space.

[4] This would result in a natural linewidth in wavenumber of $5.3 \times 10^{-4}$ cm$^{-1}$, which corresponds to 4.8 fm in wavelength (for radiation at 300 nm). This is usually not resolvable.

### 2.2.3. Overall Spectrum

The overall observable spectrum of a flame generally is a function of both emission and absorption[5]: The radiation emitted from excited molecules is subject to absorption by the same molecules present in the ground state. This process is known as self-absorption [12].

As described in the previous section, the absorption coefficient is a function of the constant Einstein coefficient $B_{i\rightarrow j}$ and the concentration of the corresponding molecule [M]. The concentration is proportional to the pressure and the mole fraction of the molecule. For the radiation resulting from radicals with very small concentrations like CH or $C_2$, self-absorption typically is not significant. The opposite is the case for the radiation resulting from molecules substantially present in flames, like the infrared radiation from $H_2O$ or $CO_2$. Self-absorption becomes more important with increasing pressure.

Hydroxyl (OH) is a special case: In the combustion of hydrocarbons, its mole fraction is generally low. Therefore, its absorption is often insignificant, especially for low-pressure and atmospheric flames. However, in the combustion of hydrogen with oxygen, OH can reach mole fractions up to 15% in the reaction zone. For elevated pressures, self-absorption has a significant impact on to the spectrum, see Figure 2.4.

### 2.2.4. Typical Flame Spectra

Each flame has its own spectrum. A comprehensive overview can be found in the book by Gaydon [49]. To illustrate the typical possible types of spectra, the UV to visible spectrum of a flame burning methane with decomposed hydrogen peroxide recorded ad Purdue University is shown in Figure 2.3.

Several peaks can be identified in the spectrum: The two single lines at 328 nm and 338 nm originate from thermally excited silver atoms [62, 141], which are present as impurities introduced by the hydrogen peroxide catalyst bed. The single lines are typical for the spectrum of single atoms: As they can only be excited electronically (neglecting the electron spin), the distinct energy levels correspond to the sharp lines.

The systems around 310 nm and 431 nm are attributed to the diatomic electronically excited molecules OH* and CH*, respectively. In addition to the electronically excited states, diatomic molecules show a rotational and a vibrational degree of freedom. Each electronically excited state hosts several vibrational states, each

[5] In theory, there also exists the phenomenon of induced emission which describes the de-excitation of a molecule by the interaction with a photon. However, in flames this effect generally is negligible [9].

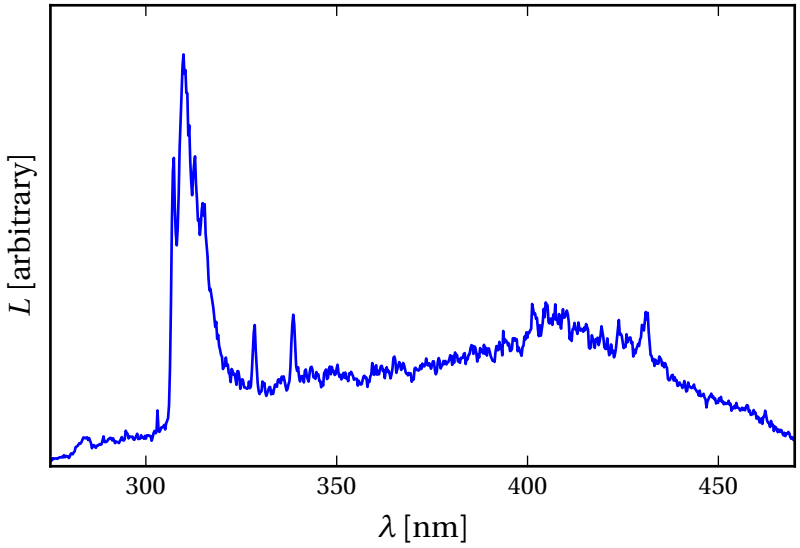


**Figure 2.3.:** Spectrum of methane burning in decomposed hydrogen peroxide (a mixture of hot oxygen and water vapor) at approximately 15 bar. Record at the Purdue University CVRC combustion chamber [7].

again exhibiting rotational states[6]. The great number of different states offers many possible state transitions, resulting in a complex spectrum. At low pressures and temperatures and when using a high-resolution spectrograph, the individual spectral lines can mostly be resolved because they do not overlap.

All the above spectra showing up in Figure 2.3 are superimposed on a broad-band background. In non-sooting flames, this is due to molecules consisting of three or more atoms. Their great number of degrees of freedom and therefore different states yield a spectrum in which the single transition lines overlap even at low pressures and temperatures and cannot be separated from each other. The overlap leads to an almost continuous spectrum, still exhibiting a fine wavelength-dependent structure. In flames which burn molecules containing carbon, the continuous background is most often attributed to $CO_2$* [27]. However, doubts about the origin exist in literature [79]. HCO* or $CH_2O$* are also sometimes suggested as the source of this continuous background.

In sooting flames, soot radiates as a continuous spectrum following a Planckian energy distribution. It is often so strong that it masks the radiation of excited molecules completely. This is one of the reasons why non-premixed flames, which tend to soot, are less often studied with respect to their molecular radiation than premixed flames.

[6] Vibrational and rotational states are sometimes summarized by the term ro-vibrational states.

### 2.2.5. Filtered Flame Spectra

In most practical situations, it is not possible to measure a fully resolved flame spectrum. Instead, band-pass filters are often used: An optical filter which transmits only a certain (typically narrow) wavelength band is mounted in front of the detector and only radiation originating from this band is recorded. The filter is typically chosen to have a narrow pass band centered around the dominant wavelength of the emission of a molecule. For example, a band-pass filter centered around 308.501 nm with a FWHM[7] of 10.646 nm is used in this work to represent the OH* radiation.

The advantage of band-pass filtered measurements is that the measurement effort is drastically reduced: A spectrograph to resolve the wavelength is not necessary and the camera does not have to sacrifice a spatial dimension for the wavelength. Additionally, the intensity of the radiation filtered over a certain band is larger by several orders of magnitude compared to the radiation of individual lines. This is essential for time-resolved measurements. Besides, an optical filter has a much lower cost compared to a spectrograph.

However, this simplification has two major drawbacks: First, all measurements are sensitive to the spectral transmittance of the optical filter and the overall wavelength-dependent quantum efficiency of the measurement setup. There are not two filters that have exactly the same transmittance due to manufacturing. Therefore, results vary depending on which filter is used. In literature, even the two key properties of the filter, the center wavelength and FWHM, are sometimes not given. This is a significant source of uncertainty when comparing different measurements.

Additionally, the lumped filtered signal does not ensure that the recorded radiation originates from a single kind of excited molecules. For example, if a band-pass filter centered around 431 nm with a FWHM of 10 nm is used to measure the CH* radiation of a flame with the spectrum shown in Figure 2.3, mostly the continuous background would contribute to the recorded signal. The radiation originating from the CH* molecule would only have a minor impact on the overall intensity. The interpretation that the filtered radiance directly corresponds to the CH* radiation would hence be false. This problem can be addressed by a correction technique described by Lauer and Sattelmayer [81]. However, the typical spectrum of the flame under investigation has to be known beforehand to apply this technique.

[7] Full Width at Half Maximum.

## 2.3. Excitation Mechanisms, Chemiluminescence, and Quenching

The previous section revealed that radiation from flames originates from the existence of excited molecules M* (see Section 2.2). The emissivity $e$ of a volume element is proportional to the number of excited molecules present within the volume, thus its concentration:

$$e_{\mathrm{M}^*} \sim [\mathrm{M}^*] \tag{2.13}$$

To investigate the origin of the radiation, it is therefore sufficient to clarify how the excited molecule M* is being produced and how the chemical steady-state concentration is reached. As M* is a sub-species of the ground species M, such an investigation is called *detailed balancing* [39, 99]. This is the focus of the following section.

Generally, the excited species can be produced by three reactions:

1. Thermal collision with another molecule Q, thereby transferring translational energy into excitation energy:

$$\mathrm{M} + \mathrm{Q} \underset{k_{\mathrm{Q}}}{\overset{k_{\mathrm{th}}}{\rightleftharpoons}} \mathrm{M}^* + \mathrm{Q} \tag{2.14}$$

2. Absorption of a photon:

$$\mathrm{M} + h\nu \underset{A_{\mathrm{M}^*\to\mathrm{M}}}{\overset{B_{\mathrm{M}\to\mathrm{M}^*}}{\rightleftharpoons}} \mathrm{M}^* \tag{2.15}$$

3. Chemical reaction of substances A and B forming the species M in the excited state:

$$\mathrm{A} + \mathrm{B} \underset{k_{\mathrm{diss}}}{\overset{k_{\mathrm{ch}}}{\rightleftharpoons}} \mathrm{M}^* \tag{2.16}$$

   This reaction can also take place in presence of a third reactant:

$$\mathrm{A} + \mathrm{B} + \mathrm{Q} \underset{k_{\mathrm{diss}}}{\overset{k_{\mathrm{ch}}}{\rightleftharpoons}} \mathrm{M}^* + \mathrm{Q} \tag{2.17}$$

All of the above reactions can also progress in the reverse direction, which de-excite the excited state. The reverse reaction of the thermal excitation (2.14) is often referred to as quenching. The de-excitation process corresponding to the absorption reaction (2.15) is essentially the spontaneous emission. The reverse of the chemical formation of the excited species M* (2.16,2.17) is a dissociation reaction.

By setting up a detailed balance for M* and evaluating it at infinite time, the steady-state concentration of the exited molecule M* can be derived[8,9]:

$$[\mathrm{M}^*] = \frac{k_{\mathrm{th}}\,[\mathrm{M}]\,[\mathrm{Q}] + B_{\mathrm{M}\to\mathrm{M}^*}\,[\mathrm{M}]\int_{\Delta\lambda}\omega_\lambda\,d\lambda + k_{\mathrm{ch}}\,[\mathrm{A}]\,[\mathrm{B}]}{\left(k_{\mathrm{Q}} + k_{\mathrm{diss}}\right)[\mathrm{Q}] + A_{\mathrm{M}^*\to\mathrm{M}}} \tag{2.18}$$

Typically, the excitation due to absorption is much smaller than chemical or thermal excitation ($B_{\mathrm{M}\to\mathrm{M}^*}\,[\mathrm{M}]\int_{\Delta\lambda}\omega_\lambda \ll k_{\mathrm{th}}\,[\mathrm{M}]\,[\mathrm{Q}] + k_{\mathrm{ch}}\,[\mathrm{A}]\,[\mathrm{B}]$). Also, dissociation is commonly neglected ($k_{\mathrm{diss}} \ll k_{\mathrm{Q}}$) [80].

Starting off from this general equation, two extreme cases are discussed in the following.

### 2.3.1. Thermal Excitation

If thermal excitation is much larger than chemical excitation and quenching is much larger than spontaneous emission, thermal excitation and quenching are the only remaining contributors to the population of M*. Therefore, Equation (2.18) can be simplified using the equilibrium constant $K$:

$$[\mathrm{M}^*] = \frac{k_{\mathrm{th}}\,[\mathrm{M}]\,[\mathrm{Q}]}{k_{\mathrm{Q}}\,[\mathrm{Q}]} = \frac{k_{\mathrm{th}}}{k_{\mathrm{Q}}}\cdot[\mathrm{M}] = K\cdot[\mathrm{M}] = \exp\left(\frac{-\Delta_{\mathrm{M}^*-\mathrm{M}}g_m^{\ominus}}{R_m\,T}\right)\cdot[\mathrm{M}] \tag{2.19}$$

In this case, M* is in thermal equilibrium with M, and its concentration (and, therefore, its emission) is a function of the temperature and the ground state concentration [M] only. The difference in the standard state enthalpies $\Delta_{\mathrm{M}^*-\mathrm{M}}g_m^{\ominus}$ between M* and M can be computed from the wavelength of the radiation corresponding to the transition. If the molecule is in thermal equilibrium, the populations in both ground and excited states are thermalized. The emission and absorption spectrum exist according to the description in Section 2.2. In flames, this is typically the case for temperatures above 2700 K [47, 77, 63, 72].

### 2.3.2. Chemical Excitation and Chemiluminescence

In comparably cold flames (below 2500 K), radiation from excited molecules is observed which is much larger than the equilibrium radiation at that temperature. This is due to chemical excitation (2.16), and the resulting radiation is, therefore, called chemiluminescence. When modeling chemiluminescence, both thermal

[8] For simplicity, only a single quenching species Q and a single chemical excitation $\mathrm{A}+\mathrm{B} \rightleftharpoons \mathrm{M}^*$ is considered.

[9] The term $\int_{\Delta\lambda}\omega_\lambda\,d\lambda$ represents the wavelength-integrated radiant energy density.

excitation and absorption is often ignored [100]:

$$[\mathrm{M}^*] = \frac{k_{\mathrm{ch}}\,[\mathrm{A}]\,[\mathrm{B}]}{k_{\mathrm{Q}}\,[\mathrm{Q}] + A_{\mathrm{M}^*\rightarrow\mathrm{M}}} \tag{2.20}$$

The chemiluminescent radiation is mainly influenced by the rate constant of the chemical excitation $k_{\mathrm{ch}}$ and the concentration of the reactants. If quenching is negligible, then the denominator in Equation (2.20) becomes the constant Einstein coefficient $A_{\mathrm{M}^*\rightarrow\mathrm{M}}$ and the emission is directly proportional to the rate of progress of reaction (2.16). However, quenching is often significant and has to be taken into account following the above relation. The equation shows the characteristic form of a Stern-Volmer equation [4, 103]. The rate constant of the quenching reaction $k_{\mathrm{Q}}$ is commonly split into the product of the quenching cross section, which is weakly depending on the temperature, and the average thermal collision velocity, which varies with the square root of temperature [6, 105, 133]. Under dominant chemical excitation, the excited state M* is not electronically thermalized with respect to the ground state M. The spectrum is thus not necessarily the equilibrium spectrum. However, as pointed out in Section 2.2, rotational and vibrational states are thermalized much faster than electronic states. The rotational distribution is commonly thermalized in flames, while vibrational non-equilibrium is sometimes observable in the spectrum [44, 46, 49].

All of the above modeling of the thermal and chemical excitation can be made on a state-to-state basis with M and M* being two distinctive quantum states. In this case, quenching and thermal excitation can be subdivided into rotational and vibrational transfer rates. However, this approach also describes the wavelength-filtered total emission of “an” electronically excited molecule M*. For the OH molecule, this will be discussed in detail in Section 4.2. Additionally, intermediate balances are theoretically possible, e.g. considering the transitions between electronic and vibrational states but not rotational states [89].

## 2.4. OH* Radiation

The radiation from the excited hydroxyl radical OH* is the most distinct radiation of flames in the UV. It is often used as a flame marker because its spectrum around 310 nm is so far in the UV that thermal background radiation does not influence the measured signal. OH is a key species and present in the combustion of all fuels containing hydrogen. Hydroxyl also is an important radical for many other chemical processes. Its spectral properties are very well known. A comprehensive summary on the OH* radiation from flames is given by Gaydon [49] or Mavrodineanu and Boiteux [92].

### 2.4.1. The OH Spectrum

Besides a ro-vibrational spectrum in the infrared, which is not discussed in this thesis, the dominant part is the UV system with a band head at 306.4 nm. It originates from a transition between the first electronically excited state ($A^2\Sigma^+$) and the ground state ($X^2\Pi_i$)[10]. A typical emission spectrum is shown in Figure 2.4. The simulated data is blurred with two Gaussian kernels of different FWHM to illustrate measurement data obtained from a coarse and a fine grated spectrograph.

The strongest features of the OH band are the bands from transitions with equal vibrational quantum number $v$: $v' = 0 \rightarrow v'' = 0$ transitions with a head at 306.36 nm, $v' = 1 \rightarrow v'' = 1$ transitions with a head at 312.16 nm, and $v' = 2 \rightarrow v'' = 2$ transitions with a head at 318.47 nm. They overlap mostly in the range between 306 nm and 330 nm. Transitions with a vibrational state difference of $\Delta v = -1$ peak between 281 nm and 300 nm, transitions with a vibrational state difference of $\Delta v = 1$ between 343 nm and 360 nm [49].

The determination of the exact spectral properties of OH has been the subject of numerous publications. The first comprehensive line list was published by Dieke and Crosswhite [28]. The Einstein coefficients of the ro-vibrational transitions are summarized by Dimpfl and Kinsey [29]. A coarser subset of vibrational transition probabilities only is given by Luque and Crosley [89]. The thermodynamic parameters of the single excited state $A^2\Sigma^+$ is tabulated as a function of temperature in the database of Burcat and Ruscic [15] based on the values summarized by Huber and Herzberg [66]. Non-equilibrium effects relevant for Laser-Induced Fluorescence like vibrational and rotational energy transfer can be found in the work by Kohse-Höinghaus [76] and Lee et al. [85].

These values have been incorporated into standard spectroscopic software. The most sophisticated data for OH from Luque and Crosley [89] is tabulated in the Lifbase program [90]. This data is also the basis for the tables stored in the extensive HITRAN/HITEMP data base [50, 121]. While Lifbase is able to compute emission and absorption spectra separately, HITRAN/HITEMP can also compute emission spectra which account for self-absorption in homogeneous media (see also Section 2.2.3). This is also possible with the Specair software, which again relies on the HITRAN/HITEMP data base [128]. Another software package to simulate the spectrum of OH is LASKIN [14, 12]. This package can also account for rotational and vibrational energy transfer important for LIF.

[10] $A^2\Sigma^+$ and $X^2\Pi_i$ describe the orbital shape of the states [4].

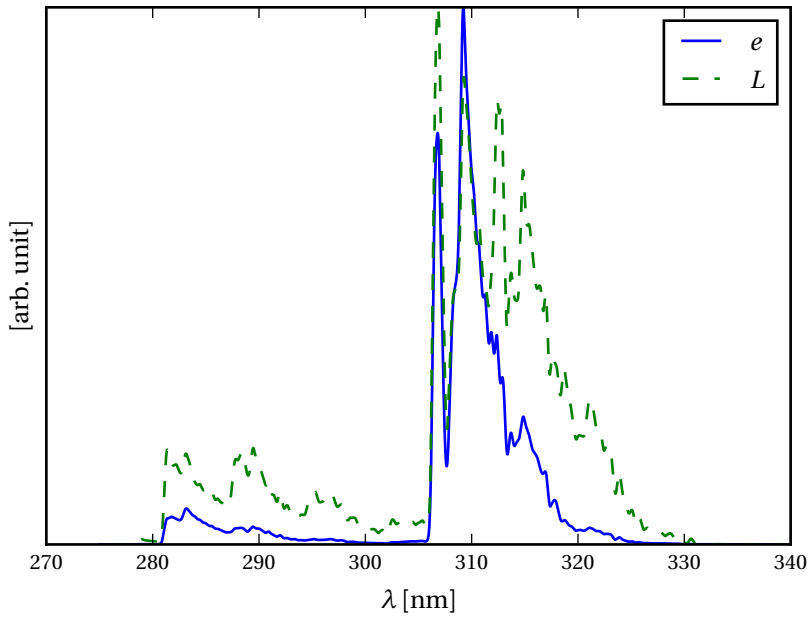


**(a)** Spectrum blurred with a Gaußian kernel with a FWHM of 0.2 nm

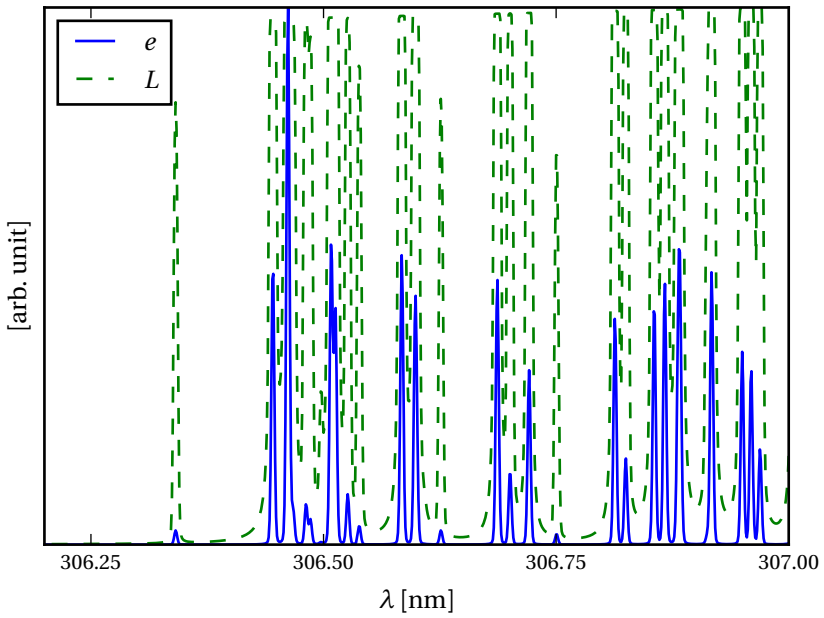


**(b)** Spectrum blurred with a Gaußian kernel with a FWHM of 1 pm

**Figure 2.4.:** Spectrum of pure OH at 3000 K and 1 bar in a 10 mm thick cell, calculated using an own implementation of the HITRAN/HITEMP software (see Section 4.1.3). The fundamental data is based on the HITRAN/HITEMP data base [50, 121]. The pure emission spectrum ($e$) is compared to the radiance spectrum $L$ which takes into account self-absorption.

| **Reference** | **A** [$cm^9\ mol^{-3}\ s$] | **n** [-] | $\mathbf{E_a}$ [$kJ\ mol^{-1}$] |
|---|---|---|---|
| Kaskan [71] (1959) [10] | $3.63 \cdot 10^{13}$ | 0 | 0 |
| Hidaka et al. [63] (1982) | $1.2 \cdot 10^{13}$ | 0 | 29.0 |
| Koike and Morinaga [77] (1982) | $1 \cdot 10^{13.92 \pm 0.17}$ | 0 | 34.73±5 |
| Dandy and Vosen [24] (1992) [11] | 0 | 0 | 0 |
| Petersen et al. [110] (2003) | $3 \cdot 10^{14}$ | 0 | 29.0 |
| Smith et al. [127] (2005) [12] | $5.45 \pm 2.3 \cdot 10^{12}$ | 0 | 0 |
| Hall and Petersen [57] (2006) | $3.1 \cdot 10^{14}$ | 0 | 41.84 |
| Kathrotia et al. [72] (2010) | $1.5 \cdot 10^{13}$ | 0 | 25 |

**Table 2.1.:** Overview of reaction rate constants $k = A\,T^n\,\exp(-E_a/(R_m\,T))$ for reaction (2.21) from various references.

### 2.4.2. OH* Chemiluminescence

While OH is reported to be in thermal equilibrium above approximately 2700 K [42, 47, 63, 72, 77, 86], the radiation from colder flames is mostly due to chemiluminescence. The chemical reactions probable to form OH* in the excited state have been investigated in many studies [71, 49, 127, 24, 63, 77, 72, 57, 111, 21, 8, 55, 42, 86]. For hydrogen flames, most authors came to the conclusion that the dominant reaction is [63, 77, 72, 57, 111, 86]:

$$O + H + Q \longleftrightarrow OH^* + Q \tag{2.21}$$

Gaydon and co-workers spectrally investigated OH* chemiluminescence and found an abnormality in low-pressure hydrogen-air flames [44, 46, 49]. However, most literature deals with the band-pass filtered radiation as described in Section 2.2.5. In order to model this radiation, the reaction rate of Equation (2.21) has to be known by its Arrhenius parameters. An overview of this data in literature is stated in Table 2.1. In most cases, the rate coefficients were determined for low-pressure flames in shock tubes. A great scatter in the reaction rates is evident. This is possibly due to the problems arising from filtering of radiation as discussed in Section 2.2.5, differences in the underlying detailed reaction mechanisms, and neglecting of self-absorption. Still, even recently published reaction rates vary within one order of magnitude. The accuracy of these values is, therefore, questionable.

To correctly model chemiluminescence, also the reaction rates of the quenching reactions have to be known. The most recent data is available from Tamura et al. [133], who re-evaluated studies by Paul [106] and tuned the low-temperature range. All recent chemiluminescence publications are based on this work.

[13] In combination with Davis et al. [26]; reanalyzed in Smith et al. [126] and Panoutsos et al. [104], recommended by Leo et al. [86].

[14] Does not consider reaction (2.21), but instead $O_2 + H \longrightarrow OH^* + O$, $O + H_2O \longrightarrow 2OH^*$, and $H_2O + Q \longrightarrow OH^* + H + Q$.

[15] Considers also reaction $OH + OH + H \longrightarrow OH^* + H_2O$.

As will be shown later, OH* is mainly thermally excited in high-pressure hydrogen-oxygen flames (see Section 4.2). Therefore, the problem of the attested uncertainty is not significant for this study.

### 2.4.3. Pressure Effects on the OH* Radiation

The behavior of the overall OH* radiation at high pressures is ambiguously described in literature. One would expect the intensity to grow with pressure, because the adiabatic flame temperature is higher. This trend has early been confirmed by Liveing and Dewar [88]. They found out that the radiation intensity of a non-premixed oxygen-in-hydrogen flame increased with approximately $p^2$, and that of a hydrogen-in-oxygen flame with a slightly smaller exponent. Experiments by Diederichsen and Wolfhard [27] showed that a hydrogen-oxygen diffusion flame at 40 bar has an OH* emission about 400 times higher than the flame at 1 bar. Recently, Petersen et al. [111] published that in a premixed methane flame at about 2200 K, OH* radiation increased by a factor of 1.7 at a pressure of 14 atm compared to 10.3 atm. In LOX-$H_2$ rocket motors, Burrows and Povinelli [18] observed an exponential increase in OH* radiation with pressure, with the exponent ranging from 3.2 to 2.0. Mayer and Tamura [93] confirmed this observation in the DLR combustion chamber C.

Surprisingly, Klimenko et al. [75] measured a different trend in the very same combustion chamber: At two different locations, OH* radiation remained constant or even decreased for an increase in pressure. They estimated that this effect is due to recirculated products around the flame absorbing radiation. Higgins et al. [64] reported the intensity of OH* radiation in a premixed methane flame to be proportional to $p^{-0.86}$, thus decreasing.

This summary shows that the pressure influence on the OH* radiation cannot be trivially described, but varies strongly depending on the test and measurement conditions. An explanation for this apparently inconsistent data will be given in Section 4.4.4.

## 2.5. The Blue (Continuous) Radiation

In addition to the well-known OH system in the UV, hydrogen flames emit a broadband radiation spectrum which peaks at approximately 440 nm. Therefore, it is often labeled *blue* or *continuous* hydrogen flame radiation [27, 49, 103]. This radiation is weak in comparably cold and low-pressure flames. At elevated pressures and high temperatures, it can contribute significantly to the overall emission. The spectrum shows a continuous shape with a superimposed fine structure. It extends from 220

nm to about 600 nm, showing a flat maximum at 440 nm. The blue radiation is the most distinct radiation of hydrogen flames visible to the human eye. A well-known example is the bluish plume of the Space Shuttle Main Engine or the Vulcain Engine.

Even though it was observed earlier than the OH* radiation [49], very little literature covers the blue radiation. It is first mentioned as "well known" by Frankland in 1867 [40]. The strong increase of the blue radiation with pressure is reported by Liveing and Dewar in 1890 [88]. An overview spectrum is shown by Diederichsen and Wolfhard [27] as well as by Mayer and Tamura [93]. Schefer et al. [123] recently showed the fine-structure of the radiation between 400 nm and 500 nm.

The origin of the blue radiation is still unclear. Gaydon [48] summarized three possible sources: It could be 1) an unresolved structure of the OH bands, 2) radiation from ionisable impurities (which was formerly also proposed by Finkelnburg [38]), or 3) a chemiluminescent reaction. Diederichsen and Wolfhard [27] were able to rule out the first two options, and Schefer at al. [123] again showed that the blue continuum radiation indeed originates from the hydrogen-oxygen system and is not due to impurities. This leaves a chemiluminescent reaction as the only possibility. Gaydon [48] proposed the following reaction forming water vapor:

$$\mathrm{OH} + \mathrm{H} \longrightarrow \mathrm{H_2O^*} \longrightarrow \mathrm{H_2O} + h\nu \tag{2.22}$$

In addition, Diederichsen and Wolfhard [27] suggested a reaction forming hydrogen peroxide, which was in slightly better agreement with their observed pressure dependency:

$$\mathrm{OH} + \mathrm{OH} \longrightarrow \mathrm{H_2O_2}^* \longrightarrow \mathrm{H_2O_2} + h\nu \tag{2.23}$$

Both reactions were studied by Padley [103] and Vanpee and Mainiero [137]. Padley recorded the total emission of a non-premixed hydrogen-oxygen flame diluted with nitrogen. By varying the nitrogen content, he was able to control the flame temperature. His comparison of equilibrium radical concentrations with the recorded intensity yielded a better description by Equation (2.22). In contrast, Vanpee and Mainiero came to the opposite conclusion: They studied the radiation from argon-diluted non-premixed hydrogen-oxygen flames, premixed hydrogen-oxygen flames, and premixed hydrogen-nitric oxide flames, each at varying equivalence ratios. Their comparison with equilibrium radical concentrations shows a better agreement with Equation (2.23).

The small number of investigations and their partially contradicting results illustrate that the origin of the blue radiation is not yet fully clarified. Further research on this topic clearly is necessary to thoroughly understand the blue radiation to derive conclusions from its measurement. This is attempted in Chapter 5.

## 2.6. Radiation and Heat Release

As pointed out in Chapter 1, the key parameter to study the interaction between combustion and acoustics is the local volumetric heat release rate $\dot{q}$. However, this quantity is hard to measure experimentally and practically unfeasible in many situations. Instead, numerous authors used the chemiluminescent radiation of excited radicals, mostly OH* and CH*, as a marker for it [7, 31, 41, 56, 58, 60, 84, 140, 142, 143]. This approach is based on the crude assumption that chemiluminescence occurs in zones where chemical reactions take place, and heat release is also defined by chemical reactions. However, there is no physical model behind such a correlation.

Many studies have been performed in the past to investigate this convenient relation. The focus commonly is on premixed combustion of hydrocarbon fuels with air, because thermo-acoustic instability is a potential hazard in lean premixed gas turbine combustors, which are favored due to their low nitric oxides emission. A detailed review on the correlation between heat release and flame emission for premixed hydrocarbon flames is given by Lauer [80]. It is generally agreed that both OH* and CH* chemiluminescence are poor quantitative markers in turbulent flames for the local volumetric heat release rate [97, 5], but that the overall flame emission is linked to the overall heat release [22, 58]. Much effort has been made to the development of heat release imaging, which claims to yield the spatial heat release rate from the measurement of several chemically excited species [59].

The key problem is the influence of turbulence and curvature which results in flame strain. This has a significant non-linear effect on the relation between heat release and OH* and CH* radiation in premixed flames. Lauer et al. [82] proposed a method to correlate OH* chemiluminescence and the heat release rate which relies on the knowledge of the strain rate distribution within the flame. When studying the entire flame zone, the strain rate effects tend to neutralize, and the above observed proportionality is described.

On non-premixed combustion, as it is always used in liquid rocket engines, only sparse literature is available with respect to the relation between heat release rate and radiation. Panoutsos et al. [104] numerically investigated a counterflow non-premixed methane-air flame and came to the conclusion that OH* radiation can be used as a topological marker for heat release rate because the distance between the peak in heat release and chemiluminescence peak is small for this combination of fuel and oxidizer. They did not propose any quantitative relationship. Yoo et al. [147] performed a similar study on spherical low-pressure nitrogen-diluted hydrogen-air flames. In their study, the heat release rate and OH* peak at different locations. Recently, Hossain and Nakamura [65] compared the numerically simulated profiles of the heat release rate and the CH* concentration in atmospheric counterflow diffusion flames of methane and propane burning with air. Within the laminar flame, both CH* and the heat release rate peak at close spatial locations, but the

general shapes are very different from each other. They applied the procedure by Lauer et al. [82] to compare the flamelet-integrated heat release rate with the flamelet-integrated CH* radiation at varying strain rates. For low strain rates, a linear relationship (but not direct proportionality) is observed. It becomes highly non-linear near the extinction strain rate. The authors numerically studied the influences of fuel types, the chemical mechanisms used for the ground state and the excited species, the diluents, and the diffusion properties of CH* by parameter variation. They concluded that the computation of the precursors for the chemiluminescent reaction ($C_2H$ and $C_2H_2$) have the most significant impact on the modeled CH* radiation. Although Hossain and Nakamura [65] included OH* in their simulation, they did not elaborate on its radiation.

Experimentally, the relationship between OH* radiation and heat release rate has not been discussed thoroughly in literature for non-premixed flames. The only work touching this context is by Burrows and co-workers [19, 18, 17], who, however, only used the OH* radiation within a rocket combustion chamber to mark the reaction zone. Bedard et al. [7] recently published their first approach on this subject. Besides presenting the measured, time-resolved spectrum of a single injector burning methane with decomposed hydrogen peroxide (a mixture of hot oxygen and water vapor), they compared the heat release rate with the OH* and CH* radiation obtained from a numerical simulation. As the simulation was performed with a significantly reduced mechanism, the radiation was modeled in a post-processing step. The radiation was approximated by just taking into account chemical excitation rates, thus ignoring any thermal influence. While the comparison of the numerical data yields some spatial correlation between the heat release rate and radiation, the simulated radiation does not match the experimentally observed values. This questions their radiation modeling and thereby their interpretation. Nevertheless, they concluded that both CH* and OH* are insufficient to provide both the spatial and temporal detail to resolve the heat release rate in their combustor.

The blue continuous radiation from hydrogen flames has never been investigated as a potential marker for the local volumetric heat release rate.

There is a clear lack of knowledge concerning the relation between heat release rate and both OH* and blue radiation with respect to non-premixed flames, particularly ones burning hydrogen. Chapter 6 will provide experimental and numerical data to fill this gap.

# 3. Laminar Hydrogen-Oxygen Jet Flame Experiment and Simulations

To investigate flame radiation, a lab-scale combustor is designed. The flame is optically accessible. This allows for spectrally resolved measurements of flame radiation. To explore the origin of radiation, this data should be compared to the molecular structure of the flame. However, the determination of the molecular structure is not possible from the experiment alone with reasonable measurement effort. This similarly applies for the local volumetric heat release rate. To interpret the experiment, it is complemented by a numerical simulation which provides the additional information. To ensure that the numerical data is reliable, the flame is chosen to burn in the laminar regime. This avoids the great uncertainty of turbulence-chemistry interaction.

Typical liquid rocket combustion chambers run at 80 bar combustion chamber pressure and higher. Ideally, the same operating pressure should be reached in the experiment for best comparability. Nevertheless, to define manageable safety margins and to ensure reasonable cost, a pressure of 40 bar was decided to be reached at maximum. This permits the use of standardized components with nominal pressure (PN) of 46 bar. By studying flame radiation at various pressures between atmospheric conditions and 40 bar, all trends relevant for the investigation of rocket combustion should be captured.

The combustion in practical rockets is highly turbulent. However, the turbulent flames in rockets can be described by ensembles of laminar flamelets. To transfer the findings from laminar onto turbulent flames, counterflow flame simulations are conducted. Their setup is explained at the end of this chapter.

## 3.1. Design Approach of the Experimental Combustor

The design of a stationary laminar non-premixed combustion experiment at elevated pressures is more difficult than it might appear at first glance [2, 37, 70]. The main problem is the stability of the fragile equilibria between viscous, momentum, and volumetric forces maintaining its shape. Additionally, the increase in

the adiabatic temperature with pressure in combination with the reduction of the quenching distance is hazardous to any material near the flame zone.

For the latter reason, jet flames are the most common types for high pressure experiments in literature [20, 25, 37, 70, 134, 69]. Such a setup typically consists of a tubular vertical fuel lance housed inside an annular oxidizer co-flow (see Figure 3.1). The flame is stabilized at the tip of the fuel lance and shielded by a glass tube. It is usually under-ventilated (i.e. the medium in the co-flow is in excess of stoichiometric conditions [136]), preventing the flame from touching the outer shield. The pressure can be modified by placing the burner inside a pressurized housing.

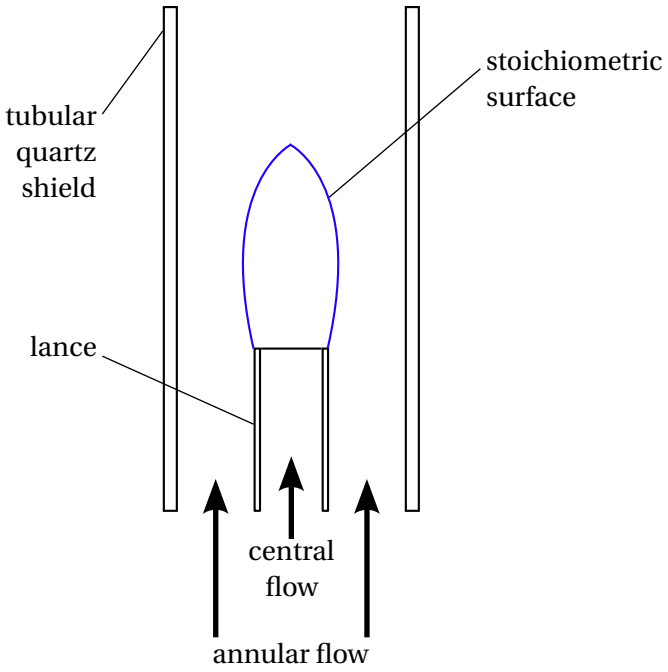


**Figure 3.1.:** Schematic setup of a typical under-ventilated jet flame with annular co-flow.

This general approach is also pursued in the design of this burner. To study the flame at pressures between 1 and 40 bar, several operating parameters are possible to be adjusted. However, there exist certain design constraints which should be fulfilled at all pressures:

1. **Geometry.** To ensure accurate and cost-efficient machining of the test rig, the components should have reasonable dimensions. Additionally, for simplicity and reproducibility, the geometry (characterized by the inner diameter $d_c$ of the lance) should be fixed, which implies that the diameter of the fuel lance does not change during test runs.

2. **Flame size.** To resolve the flame radiation optically with standard equipment, the radiating size of the flame $l$ should be between 10 mm and 100 mm. The size should be as constant as possible for different pressure levels.
3. **Optical access.** The flame should be accessible through quartz windows or components to study the entire visible and UV radiation spectrum.
4. **Heat release.** At all operating conditions, the heat release by the flame should be endurable. Additionally, as the heat released is generally proportional to the mass flow rates of the reactants, it should be kept at the lowest reasonable level to limit the cost of operation.
5. **Flow stability.** The flame should burn at stationary conditions and should not flicker. Instability due to both flow turbulence and buoyancy should be avoided.

The Roper correlation states that the size of a laminar jet flame (as defined by its luminous length $l$) normalized by the inner diameter $d_c$ of the lance is proportional to the Reynolds number of the pipe flow [16, 118, 132, 136, 70, 131]:

$$l/d_c \sim Re \tag{3.1}$$

Therefore, if requirements 1. and 2. are fulfilled and $d_c$ and $l$ are fixed, the Reynolds number is constant as well. The flame is thus inherently protected from laminar-turbulent transition, if the Reynolds number is sufficiently small under initial operating conditions. Furthermore, the Reynolds number is proportional to the mass flow rate $\dot{m}_c$ of the fluid in the lance:

$$Re = \frac{u_c\, d_c}{\nu_c} = \frac{\dot{m}_c}{\frac{1}{4}\pi\, d_c^2\, \rho_c} d_c \frac{\rho_c}{\mu_c} = \frac{4\dot{m}_c}{\pi\, d_c\, \mu_c} \tag{3.2}$$

The dynamic viscosity $\mu_c$ of the flow through the lance is in good approximation insensitive to the pressure. In order to ensure approximately constant flame length at constant inner lance diameter, the mass flow rate $\dot{m}_c$ thus has to be constant. Additionally, if the mass flow rate remains constant, also the total heat release rate is unchanged. Therefore, the described set of parameters already satisfies most of the requirements stated above.

The only remaining problem is instability due to buoyancy. This instability is known as *varicose mode* instability [11]. It arises from the radial density gradient in the plume of the flame. Typically, the gas in the plume has a low density because of the high temperature. Additionally, for a hydrogen flame, the plume consists of mostly water vapor which has a lower density compared to oxygen. If a fluid volume on the edge of the plume is considered as in Figure 3.2, gravity acting on the density gradient results in a torque. This tends to accelerate the flow on the centerline. Following mass conservation, the plume becomes narrower and the density gradient is increased. At some point, the viscous forces cannot resist the imposed shear stress and instabilities arise.

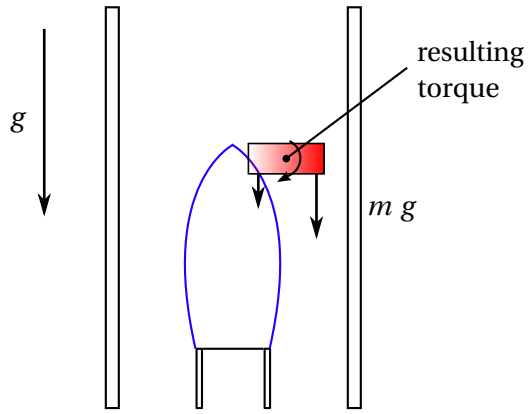


**Figure 3.2.:** Illustration of the varicose mode instability due to buoyancy following [11].

Every laminar plume becomes eventually unstable by the varicose mode instability. For this study, it is only important that the flow in the luminous zone is stationary and free of this instability. To compare the onset of the instability between flames, the dimensionless Froude number is used in literature [2, 11, 131][1]:

$$Fr = \frac{u_c^2}{g\ d_c} = \frac{16\dot{m}_c^2}{\pi^2\ g\ d_c^5 \rho_c^2} \tag{3.3}$$

The Froude number compares the momentum forces to the gravitational force. For high Froude numbers, the flame shape is controlled by momentum, whereas for low Froude numbers the flame is controlled by buoyancy.

Equation (3.3) shows that the buoyant forces become more significant compared to the momentum forces by the square of the center inflow density $\rho_c$. Applying the equation of state for ideal gases and assuming constant inflow temperature, the center inflow density $\rho_c$ is proportional to the chamber pressure $p$. A setup as described above, in which the geometry and the mass flow rate are kept constant to fulfill the constraints of turbulence, flame size, and heat release, therefore cannot be similar with respect to buoyancy effects at changing pressure.

To establish a stable laminar flame at a broad range of pressure, the problem of varicose mode instability has to be addressed by initial design: Instead of hydrogen burning in an oxygen co-flow, the two media are interchanged. The flame is established by a limited amount of oxygen which burns completely in a hydrogen co-flow. This alteration has two advantages: First, hydrogen has a significantly lower molecular weight than water vapor. The radial density gradient between the burnt gases and the ambient fluid is therefore reduced. Second, hydrogen is considerably more diffusive than oxygen and has a much higher heat conductivity. The temperature

[1] Sometimes, also the Richardson number is used, which is the inverse of the Froude number slightly modified by a temperature term [37].

and species gradients in the plume are thus able to be dissolved before the buoyant instability arises.

## 3.2. Combustor Setup and Parameters

A sketch of the experimental combustor is shown in Figure 3.3. The laminar flame is established by oxygen burning in a hydrogen co-flow. A mass flow rate of 40 mg/s oxygen is fed through a quartz fuel lance with an outer diameter of 10 mm and a wall thickness of 1 mm. This corresponds to a Reynolds number of 332 with respect to the lance inner diameter. At the tip of the lance, a steady anchored diffusion flame is stabilized. The hydrogen is supplied through an annular duct at a mass flow rate of 20 mg/s and a Reynolds number of 303 with respect to the hydraulic diameter of the duct. The great excess of hydrogen (equivalence ratio 4) leads to a manageable exhaust gas temperature.

The flame is shielded by a 1 mm thick quartz tube with an internal diameter of 20 mm. It is housed inside a partially water-cooled pressure vessel. Nitrogen flows between the flame shield and the vessel walls to prevent the test rig from overheating and to further reduce the exhaust temperature. The pressure inside the vessel is adjusted by the exhaust valve and the nitrogen flow rate. The test rig is designed to withstand pressures of up to 40 bar.

The pressure is built up and regulated by an electrically assisted needle valve (Swagelok MS-ETC38720 with Gulex N802/P7/4) in the exhaust. The pressure is monitored by a pressure transducer (Wagner P-05) mounted at the nitrogen inlet. Hydrogen, oxygen, and nitrogen are supplied by standard gas cylinders. Their mass flow rates are controlled by Bronkhorst mass flow controllers (Bronkhorst F-232M-RGD-33-V). The oxygen is fed into the burner through the lance which is long enough to establish a fully-developed Hagen-Poiseuille flow. The hydrogen flows through six radial jets into a plenum, from which it enters the annular duct through an open porous metal foam to ensure a homogeneous flow. The nitrogen enters the pressurized chamber directly through six radial jets.

To suppress back-flow at the end of the flame shield, the combustion products impinge onto a top quartz window. Here, the flow is reversed and mixed with nitrogen. Six peripheral holes vent the exhaust into an eccentric duct, which unites the gases into the exhaust pipe (see Figure A.3). Before entering the exhaust valve, the flow is cooled by an air-cooled heat exchanger.

The flame is ignited by a conventional spark plug located above the exhaust.

Optical access to the flame is provided through quartz windows on the top and on the sides of the burner. The top window is cooled by pressurized air impinging onto the sides and the outer front of the quartz window. The side windows are part of a

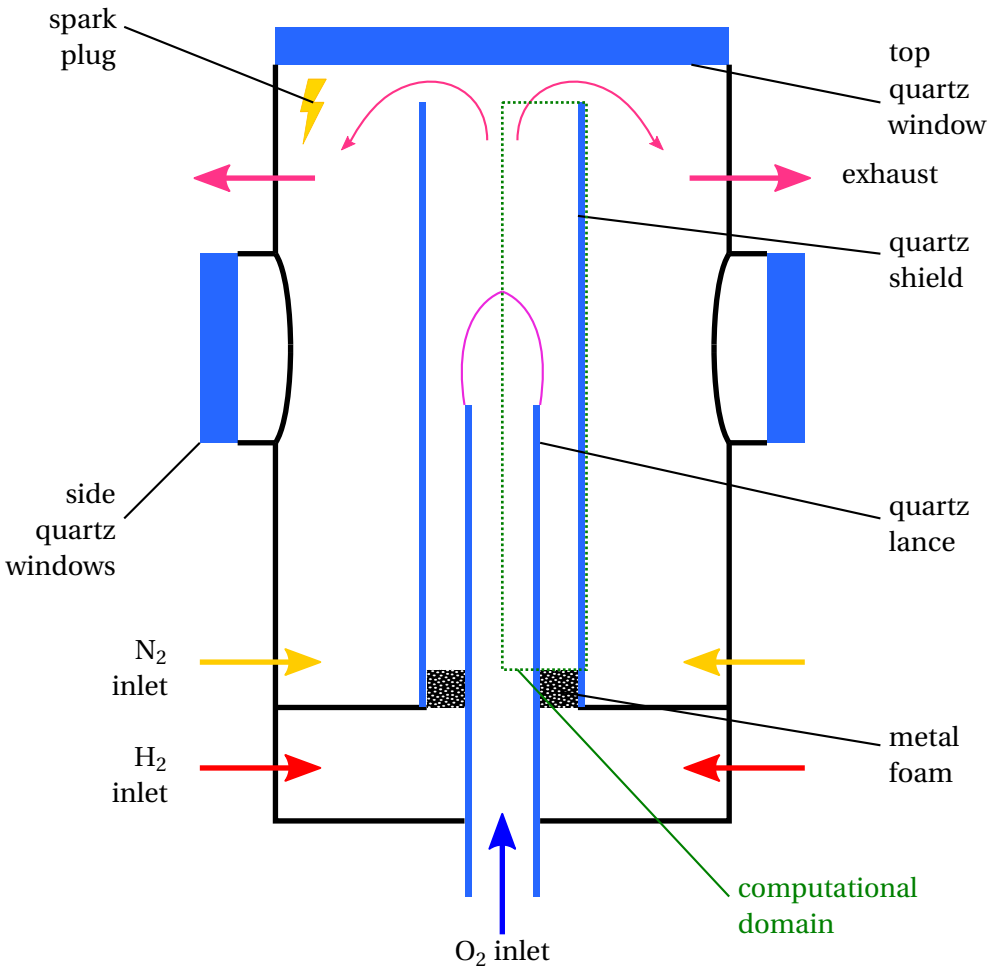


**Figure 3.3.:** Schematic drawing of the experimental high-pressure burner.

bought-in sight glass component. The tip of the burner lance and approximately 70 mm above it are visible looking perpendicular through these windows. One of the four windows of the sight glass component is replaced by a rupture disc.

A summary of the key parameters is provided in Table 3.1. Figure 3.4 shows a three-quarter section of the construction model as well as a photograph of the actual setup. Additional assembly drawings are found in Appendix A.

The design of the pressurized chamber and the regulating components was supported by Markus Lieflaender. Details on the selection of the regulating components and the structural analysis of the parts can be found in his Diploma thesis [87]. The security measures and procedures defined to ensure safe operation are also explained in his work.

In operation, a steady flame is observed up to approximately 33 bar for the described configuration and mass flow rates. For higher pressures, the flame becomes

| Parameter | Value |
|---|---|
| Inner diameter of the lance | 8 mm |
| Outer diameter of the lance | 10 mm |
| Overall length of the lance | 780 mm |
| Inner diameter of the shield | 20 mm |
| Outer diameter of the shield | 22 mm |
| Overall length of the shield | 465 mm |
| Length of the shield above the lance tip | 281 mm |
| Inner diameter of the pressure vessel | 65 mm |
| Total inner height of the pressure vessel | 533 mm |
| Oxygen inflow temperature | 296 K |
| Hydrogen inflow temperature | 295 K |
| Nitrogen inflow temperature | 296 K |
| Nominal oxygen mass flow rate | 40 mg/s |
| Nominal hydrogen mass flow rate | 20 mg/s |
| Nominal nitrogen mass flow rate | 200 mg/s |
| Nominal oxygen Reynolds number | 332 |
| Nominal hydrogen Reynolds number | 303 |
| Nominal nitrogen Reynolds number | 162 |
| Nominal pseudo equivalence ratio | 4 |
| Nominal heat release inside the burner | 600 W |
| Maximum design pressure | 40 bar |

**Table 3.1.:** Overview of the key parameters of the combustor. Reynolds numbers are based on the hydraulic diameters of the ducts.

unstable.

## 3.3. Optical Measurement Techniques and their Setup

To investigate the radiation of the flame, several measurement techniques are applied in this study. They all rely on conventional measurement devices, which are described in this section along with their setup.

### 3.3.1. Digital Camera

The simplest way to record flame radiation quantitatively is a digital camera. An image-intensified Photron Ultima APX $I^2$ CMOS camera is mainly used in this study. The camera is able to capture 2048 frames resolving 1024x1024 pixels at 10 bit in a series at a minimum frame rate of 50 frames/s. The maximum frame rate at full

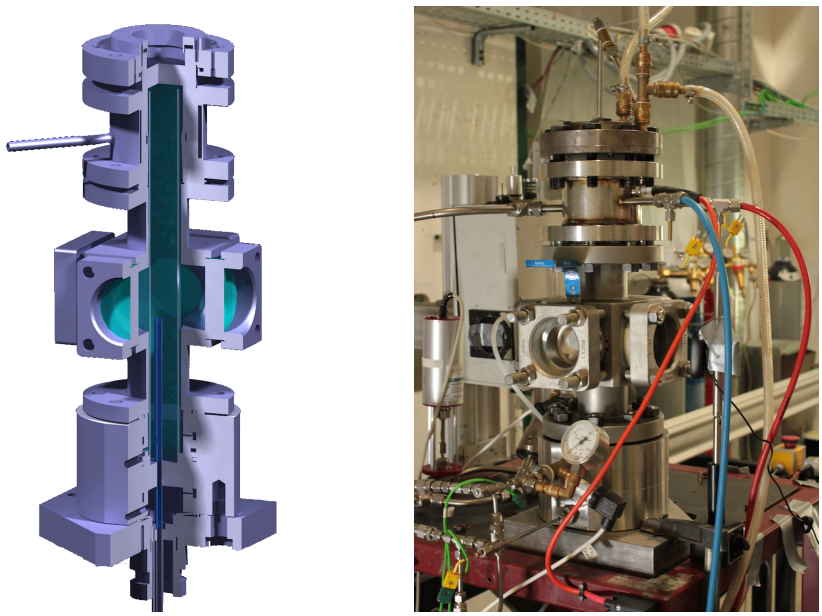

(a) (b)

**Figure 3.4.:** Construction sketch and photograph of the experimental setup.

resolution is 2000 frames/s. To record images of the stationary flame, the lowest frame rate and image intensifier gain are used to minimize random noise.

Two configurations are used: Either, the camera is mounted on top of the burner to record the total flame radiation. Additionally, the camera can view the flame from the side through the windows in the sight glass. As the entire luminous zone of the flame is visible, the overall radiation can also be recorded from this position.

To focus the flame on the camera sensor, a Nikkor 105 mm F/4.5 UV lens is used. The camera is placed 500 mm away from the flame center, which results in a resolution of 30 px/mm. The aperture of the lens is set to F/22 so that the detection system can be approximated as a pinhole camera. This is important to ensure that each pixel can be attributed to a single ray through the flame and that a (modified) inverse Abel transform can be applied (see Section 3.5).

Two optical filters can be mounted in front of the UV lens to record radiation at specific wavelength ranges: To record only the radiation of the OH spectrum, an Andover Corporation 307FS10-50 band-pass optical filter with a central wavelength of 308.501 nm and a FWHM of 10.501 nm is used. To distinguish the broad-band blue radiation from possible side effects, it is filtered by an Andover Corporation 020FC34-50/4560 band-pass optical filter with a central wavelength of 456.270 nm and a FWHM of 2.370 nm. The spectral transmittances of the filters used are attached in Appendix B.

### 3.3.2. Spectrograph

To record the spectrum of the flame, an Acton Research Cooperation SpectraPro 275 Czerny-Turner type diffraction spectrograph with a focal length of 275 mm is used. It is placed between the camera and the UV lens (without the above filter). The spectrograph is mounted such that the 10 µm wide entrance slit is horizontal. The lens focuses an approximately 0.5 mm thick horizontal slice of the flame 5 mm above the fuel lance onto the entrance slit of the spectrograph, thus containing the information along the horizontal direction.

Three diffraction gratings are installed in the spectrographs, with 2400, 600, and 150 groves/mm. In this study, the 150 grooves/mm grating with a blaze wavelength of 500 nm is used to record the overall spectrum of the flame. The optical setup for this spectrum provides a resolution of approximately 3 nm. The holographic 2400 grooves/mm grating is applied to record detailed spectra with a resolution of approximately 0.2 nm.

The wavelength range is determined from the positions of the spectral lines of a low-pressure mercury vapor lamp. To obtain quantitative results, the overall setup is calibrated against the known spectrum of a tungsten lamp [80].

### 3.3.3. Background Illumination

To study the absorption of the flame, the transmittance of radiation through the flame is investigated. Due to its high output in the UV, a LOT Quantum Design type LSB740 500 W mercury-xenon arc lamp with a broad-band spectrum is chosen as the source of radiation. The lamp is focused on to a quartz diffusor attached to the burner to provide a homogeneous diffuse background for the flame. The radiation is observed from the opposite side of the flame. The setup is illustrated in Figure 3.5.

The light source is shuttered periodically by an optical chopper to produce a harmonically fluctuating signal. By recording a time-resolved picture series and performing a pixel-wise fast Fourier transform (FFT), the signal from exclusively the background illumination can be extracted. This procedure removes any steady information as well as random noise at other frequencies than the shutter frequency, thus increasing the signal-to-noise ratio.

### 3.3.4. Tunable Dye Laser Absorption Spectroscopy Setup

To investigate the absorption of the OH radical with a high resolution in wavelength, Tunable Dye Laser Absorption Spectroscopy (TDLAS) in the UV is applied. The

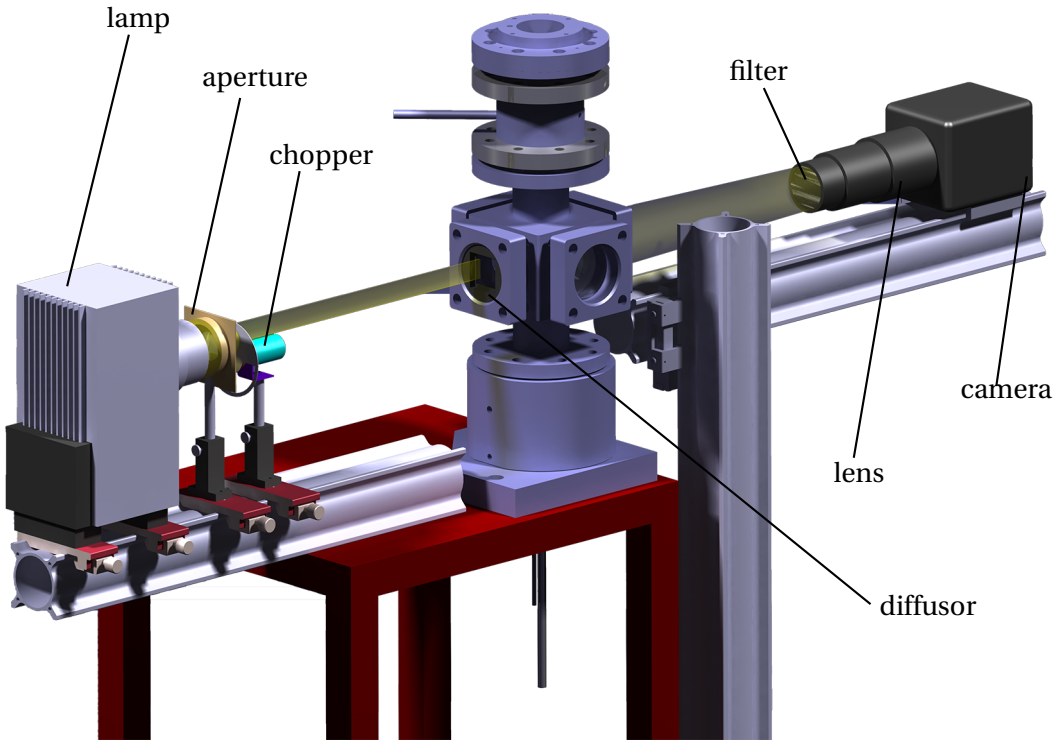


**Figure 3.5.:** Setup of the background illumination and camera.

system aims to measure the attenuation of radiation through the flame along a laser beam at a variable wavelength. The setup is illustrated in Figure 3.6.

The dye laser is pumped by a dual cavity Edgewave IS8II frequency-doubled Nd:YVO4 laser emitting radiation at 532 nm. For this study, only one cavity of the laser is used. It produces laser pulses with a design pulse energy of 2 mJ at 20 kHz repetition rate. The Sirah Credo tunable dye laser uses Rhodamine 6G dye to produce an output beam with a central wavelength between 279.5 nm and 288.5 nm and a FWHM of 1.8 pm. The manufacturer states an absolute wavelength accuracy of 30 pm. The wavelength is varied by turning the cavity end mirror inside the laser.

The beam with a diameter of approximately 0.5 mm passes through the center of the flame 5 mm above the lance. It is trapped into a sglux SG01S UV-sensitive photo diode equipped with a collimating lens and diffuser. The recorded output current is amplified using a transimpedance amplifier and recorded as a voltage signal at 50 kSamples. The averaged signal correlates well with the incoming radiance. The measurement is calibrated against a set of refractive UV filters with known transmittances for each wavelength studied.

The transmittance along the laser beam is computed by dividing the radiance measured at the flame established at a certain operating pressure by the radiance measured with the flame turned off. As the output of the laser varies with time, a

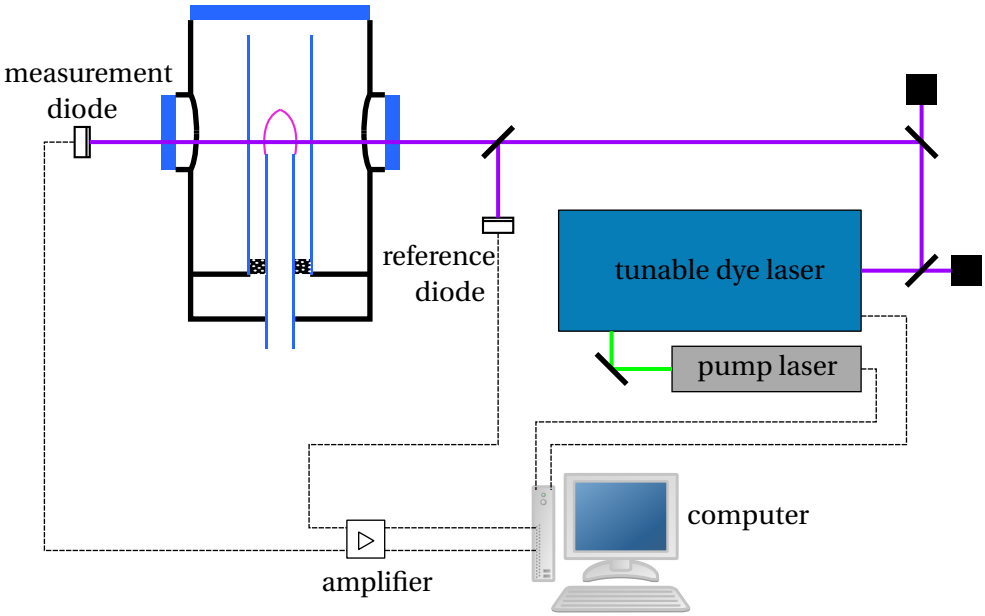


**Figure 3.6.:** Setup for Tunable Dye Laser Absorption Spectroscopy.

reference photo diode is installed (see Figure 3.6). The radiance measured by the reference diode is used to correct for the variation of the laser power.

A National Instruments LabView program controls the setting of the laser wavelength and the recording of the voltages of the photo diodes automatically [30].

## 3.4. Numerical Simulation of the Flame

To provide detailed insight into the flame structure, the experimentally studied flame is computed using a computational fluid dynamics (CFD) simulation. The commercial program Ansys Fluent 14.0 [3] is found to be the best choice to simulate this setup because it is able to handle multi-component diffusion natively.

As the experimental setup shows rotational symmetry, it is sufficient to simulate the radial profile of the flame in 2D. The entire flow field inside the 463 mm long quartz tube is modeled (see Figure 3.3 on page 30). The quartz tube itself as well as the quartz fuel lance are included in the simulation as solid regions and coupled to the flow using the conjugate heat flux model. The boundary condition for the outer glass tube is set as a convection cooling boundary condition.

For the oxygen inlet, a fully developed Hagen-Poiseuille velocity profile is assumed. The 182 mm long hydrogen duct is too short to show a fully developed laminar velocity profile. Therefore, the entire annular duct is included in the simulation. A

block velocity profile is assumed at the exit plane of the metal foam. The temperatures of both hydrogen and oxygen are set to values measured in the experiment (see Table 3.1). The top end of the domain is modeled as a pressure outlet.

The domain is meshed with 17792 nodes, corresponding to a grid size of approximately 0.5 mm per rectangular cell. The grid is the result of refining an originally 4x coarser grid. Further refinements by factors of 4x and 16x do not lead to significant deviations from the coarsest solution (see Figure 3.7).

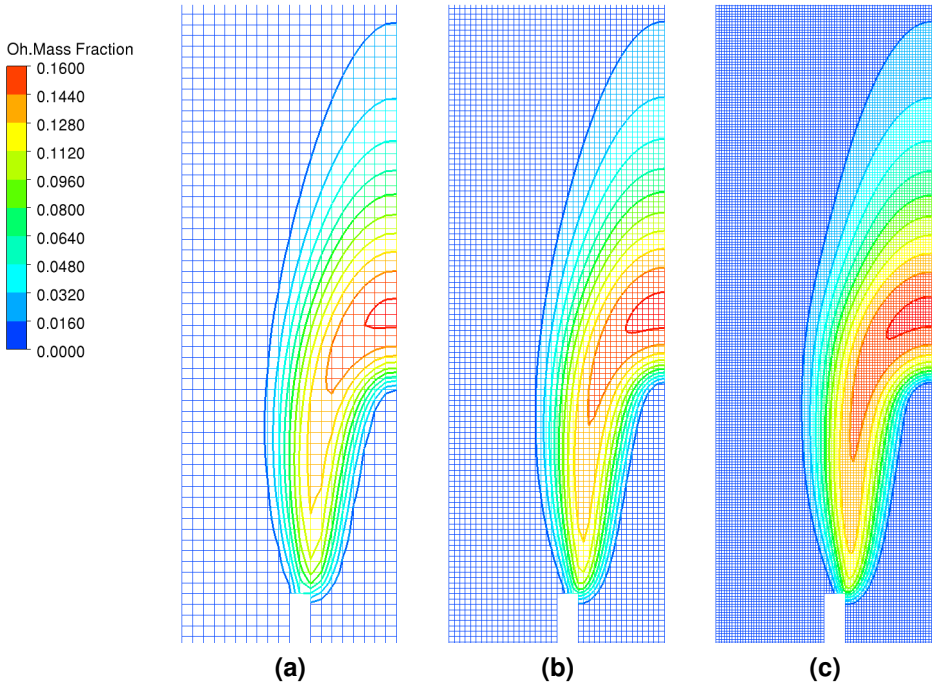


**Figure 3.7.:** Grid study: Numerically simulated OH mass fraction on the reference grid (a), the 4x refined grid (b), and the 16x refined grid (c).

Due to the stationary behavior of the flame and the low flow velocities, the steady state pressure-based incompressible solver is used. No turbulence model is applied since laminar flow is considered. As pointed out in Section 3.1, gravity has a significant impact on the flow pattern. It is included as a volumetric force. Since very high temperature levels are present in hydrogen-oxygen combustion, the thermal infrared radiation cannot be neglected. Fluent's Discrete Transfer Radiation Model (DTRM) is used to take radiative heat losses into account. This model is applicable to the range of optical densities in the infrared varying with pressure. It assumes gray radiation. The infrared absorption coefficients are computed by Fluent's Weighted Sum of Gray Gases Model (WSGGM). With growing pressure, the radiation heat loss increases from 4 % at 1 bar up to 15 % at 40 bar of the overall heat release. This is in agreement with rough engineering estimations [1]. Nevertheless, most of the

radiation heat loss originates from the hot plume because of the presence of water vapor. At the stoichiometric surface of the flame, temperatures between 3100 K and 3500 K are reached (see Figures C.1 et seqq.). As the blue and OH* radiation only account for a small percentage of the overall radiative heat flux, their effect on the overall flow field is ignored [23].

The chemical reactions are modeled using the detailed mechanism of Ó Conaire et al. [101]. The original mechanism contains ten species (H, $H_2$, O, $O_2$, OH, $H_2O$, $H_2O_2$, $HO_2$, $N_2$, and Ar) and 19 reactions. It is extended to include $CO_2$ as a non-reacting species, which is required for Fluent's Weighted Sum of Gray Gases Model to work. Additionally, the summed-up electronically excited $A^2\Sigma^+$ state of OH is included as a separate species OH*, thus inherently providing the thermalized OH* radiation. The reaction rates accounting for chemical excitation and quenching are taken from Kathrotia et al. [72]. The thermodynamic data for OH* is taken from Burcat and Ruscic [15], which is recommended by Kathrotia et al. The transport data for OH* is assumed to be identical as for ground state OH[2]. Further details on the OH* radiation modeling will be given in Section 4.1. Since OH* is present in only very small amounts and $CO_2$ does not occur at all, the underlying reaction mechanism is found not to be influenced by these modifications.

The local volumetric heat release rate is computed natively by Fluent.

## 3.5. Modified Abel Transform

A direct spatial comparison between numerical and experimental data is not possible, because the numerical simulation is performed in 2D whereas the experimental quantities are measured along 3D lines of sight. However, using mathematical transformations, equivalent spatial profiles can be generated from each set of data. The conversion from the radial to the line-of-sight integrated quantities is commonly achieved by a so-called (forward) Abel transform. The reverse process, by which the radial quantities are reconstructed from the line-of-sight integrated ones, is known as an inverse Abel transform.

Mathematically, the analytical forward transformation of a radial quantity $a(r)$ into the line-of-sight integrated quantity $A(y)$ as a function of the distance $y$ from the

[2]The latter assumption was recently justified numerically by Hossain and Nakamura [65].

center line is given by: [13] [3]

$$A(y) = 2 \int_{y}^{\infty} \frac{a(r)\, r}{\sqrt{r^2 - y^2}}\, dr \tag{3.6}$$

Its inverse is defined as:

$$a(r) = -\frac{1}{\pi} \int_{r}^{\infty} \frac{dA}{dy}(y)\, \frac{1}{\sqrt{y^2 - r^2}}\, dy \tag{3.7}$$

The key requirement for the application of the Abel transform and its inverse is that the lines of sight are single, non-interfering lines, forming a parallel projection of the object under investigation. Experimentally, this can be achieved by an unfocused Schlieren-type setup. Alternatively, the requirement can be approximated by placing a pinhole detector far away from the object. In this case, it is important to select a small aperture to preserve the association between lines and sensor pixels.

Additionally, standard Abel transforms are only directly applicable to emission measurements in which self-absorption is negligible, i.e. the medium is optically thin. Under this condition, Equation (2.3) holds along each line of sight. The parameter $a$ corresponds to the local emissivity $e_\lambda$ and the parameter $A$ to the line-of-sight integrated radiance $L_\lambda$.

The Abel transforms can also be used for measurements of pure absorption: As shown in Section 2.1, the solution of the radiative transfer equation yields a similar result as for pure emission (Equation (2.6)). In this case, the parameter $a$ corresponds to the local absorptivity $k_\lambda$ and the parameter $A$ to the negative logarithm of the transmittance $-\ln(\tau_\lambda)$.

In the present study, both requirements of parallel rays as well as the optical thinness are not always given. To overcome these problems, modified Abel-type transformations are derived in the following. The procedure consists of three steps: First,

[3] If the forward and inverse Abel transforms are to be integrated numerically, it is beneficial to avoid the singularity at $y = r$. Equations (3.6) and (3.7) then become:

$$A(y) = 2 \left[ a(y) \sqrt{(y + \delta y)^2 - y^2} + \int_{y+\delta y}^{\infty} \frac{a(r)\, r}{\sqrt{r^2 - y^2}}\, dr \right] \tag{3.4}$$

and

$$a(r) = -\frac{1}{\pi} \left[ \frac{dA}{dy}(r) \ln\left( \frac{\sqrt{(r+\delta r)^2 - r^2} + r + \delta r}{r} \right) + \int_{r+\delta r}^{\infty} \frac{dA}{dy}(y)\, \frac{1}{\sqrt{y^2 - r^2}}\, dy \right] \tag{3.5}$$

the ray through the flame associated with each camera pixel is reconstructed. Second, the radiative transport equation is set up along a generic line to compute the line-of-sight integrated radiance from the local emissivities and absorptivities. Third, a reconstruction procedure is described by which the local parameters can be computed from the line-of-sight integrated measurements. This procedure was developed with the help of Michael Nettinger [36, 98].

**Definition of the rays associated with each camera pixel.** To simplify the problem, a horizontal slice of the flame is considered and variations along the $z$-axis are ignored. Two cases are investigated and illustrated in Figure 3.8: In case (a), the camera is treated as a pinhole detector at a finite distance away from the flame. Case (b) represents an unfocused Schlieren-type camera setup or a camera infinitely far away from the flame, thus recording a bundle of parallel rays. Each pixel of the camera is associated with a single ray. By interaction with the glass parts of the burner (the quartz window (not shown) and the quartz tube), the rays are refracted. The path is computed for each ray according to Snellius' law. The bundle of rays is handed over to the next step at the innermost refracting surface, later denoted as *interface*. Within the interface, refraction due to the density gradients is neglected and the rays are assumed to be straight. The bundle of rays at the interface associated with each pixel is described by the starting positions of the rays and their angle to the horizontal axis.

**Application of the radiative transfer equation.** The axis-symmetric flame is discretized by homogeneous circular shells. The number of shells $N$ is equal to the number of rays associated with the camera pixels. To apply the radiative transfer Equation (2.7), the intersecting length $\delta_{jk\pm}$ of each ray $j$ with each shell $k$ at the first (+) and second (−) intersection have to be known (see Figure 3.8(b)). Shells with $j < k$ are not intersected. To match the general procedure, the shell with $j = k$ is split into two at the foot of a dropped perpendicular on the ray. It can be shown that the intersecting length of the first and second intersection are of equal length [98], thus just denoted by $\delta_{ij}$. These lengths can be computed from geometrical optics if the bundle of rays is defined at the interface.

The discretized application of Equation (2.7) along the $j$-th ray yields:

$$L_{\lambda,j} = \sum_{k=j}^{N} e_{\lambda,k} \left\{ \frac{1}{k_{\lambda,k}} \left(1 - \exp\left[-k_{\lambda,k}\, \delta_{jk}\right]\right) \right. \tag{3.8}$$
$$\left. \left(1 + \exp\left[-2 \sum_{l=j}^{k-1} k_{\lambda,l}\, \delta_{jl} - k_{\lambda,k}\, \delta_{jk}\right]\right) \cdot \exp\left[-\sum_{l=k+1}^{N} k_{\lambda,l}\, \delta_{jl}\right] \right\}$$

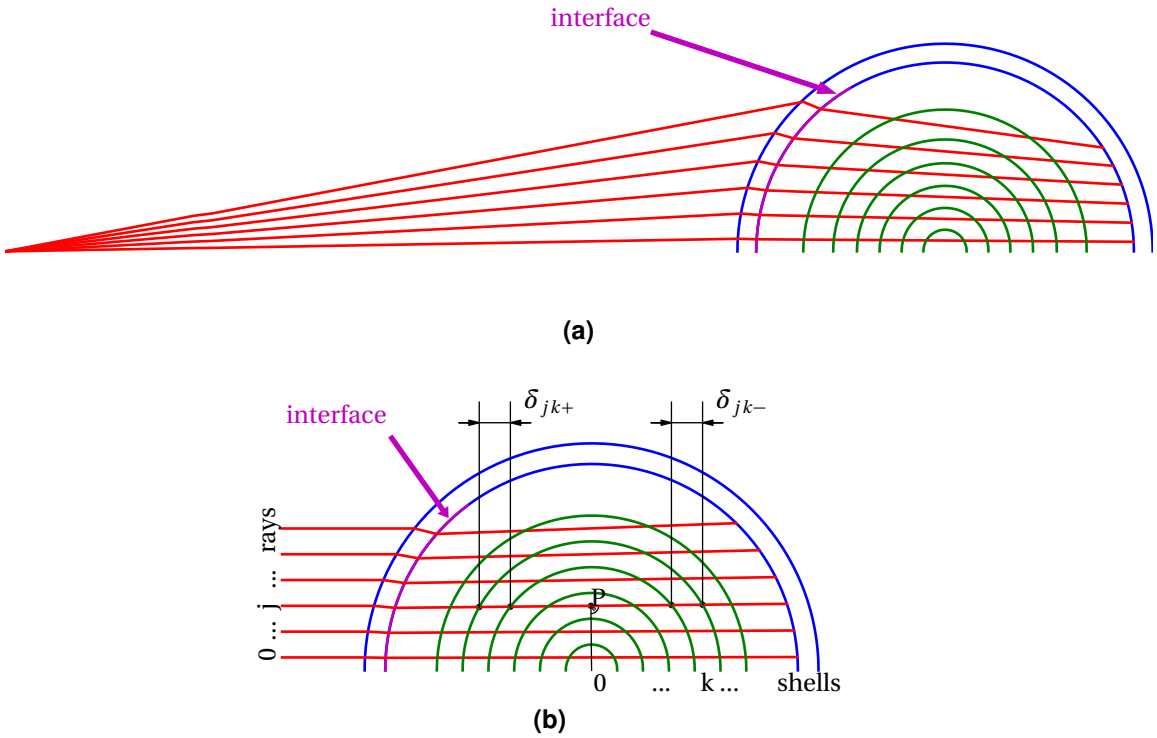


**Figure 3.8.:** Typical radiation paths through the flame. In case (a), the camera is assumed as a pinhole detector at a finite distance. In case (b), the camera is assumed to collect the radiation along parallel rays.

If self-absorption is neglected, the equation can be greatly simplified:

$$L_{\lambda,j} = 2 \cdot \sum_{k=j}^{N} e_{\lambda,k}\, \delta_{jk} \tag{3.9}$$

which essentially represents a discretized formulation of the forward Abel transform Equation (3.6). Similarly, if only absorption is considered, a formula for the negative logarithm of the transmittance can be derived:

$$-\ln\left(\tau_{\lambda,j}\right) = 2 \cdot \sum_{k=j}^{N} k_{\lambda,k}\, \delta_{jk} \tag{3.10}$$

**Reconstruction of the radial emission and absorption coefficients from line-of-sight integrated measurements.** The procedure described by Boltendahl [10] is used for this task. It consists of the following steps:

1. Determination of the geometrical parameters matrix $\delta_{jk}$ according to the experimental setup as described above.

2. Measurement of the line-of-sight integrated transmittance $\tau_{\lambda,k}$. The transmittance can typically be measured in presence of the flame's own radiation, like using the setup described in Section 3.3.3.
3. Computation of the radial absorption coefficients $k_{\lambda,j}$ by matrix inversion of Equation (3.10).
4. Measurement of the line-of-sight integrated radiance $L_{\lambda,k}$ without background.
5. Computation of the radial emissivity $e_{\lambda,j}$ by solving Equation (3.8). Although the formula appears to be complicated, the term within the curly braces actually represents a matrix of constants. If the absorptivities $k_{\lambda,j}$ and the geometrical parameters $\delta_{jk}$ are known, this matrix can be pre-computed and the equation can be solved again by matrix inversion.

This procedure is only applicable if the measured radiation is monochromatic, or if the emissivities and absorptivities are constant over the investigated wavelength band.

## 3.6. Counterflow Flame Simulations

Counterflow flame simulations will be used to study flame radiation and heat release at varying pressure and strain rate. A schematic view of the considered counterflow flame configuration is shown in Figure 3.9. Two axis-symmetric jets of fuel and oxidizer impinge onto each other from opposed nozzles, thus creating an axis-symmetric flow field. It is described by the axial coordinate $z$ and the radial coordinate $r$. Only the axial coordinate $z$ has to be resolved to specify the flame [74].

The well-known governing partial differential equations are described by Kee et al. [74]. The problem can be solved numerically by evaluating the continuity equation, the radial momentum equation, a species conservation equation for each species considered, and the energy equation. Species source terms are calculated from detailed chemistry reaction mechanisms. Pressure, density, and temperature are linked by the equation of state for ideal gases. Real gas effects were shown to have little influence on the structure of counterflow flames [113, 139].

The flow field is fully characterized by the axial coordinate $z$, the axial velocity $u$, the radial velocity divided by the radial coordinate $V = \frac{v}{r}$, the radial pressure curvature $\Lambda = \frac{1}{r}\frac{\partial p}{\partial r}$ (which is an eigenvalue and constant throughout the flame), the temperature $T$, and the species mass fractions $Y_i$ for all considered species.

So-called plug-flow boundary conditions are applied both on the oxidizer and the fuel inlet [74, 83]: The mass fluxes (flow rate area densities) $\mathring{m}_\mathrm{f} = u_\mathrm{f}\,\rho_\mathrm{f}$ and $\mathring{m}_\mathrm{o} = u_\mathrm{o}\,\rho_\mathrm{o}$, the inlet temperatures $T_\mathrm{f}$ and $T_\mathrm{o}$, and the inlet compositions $Y_{i,\mathrm{f}}$ and

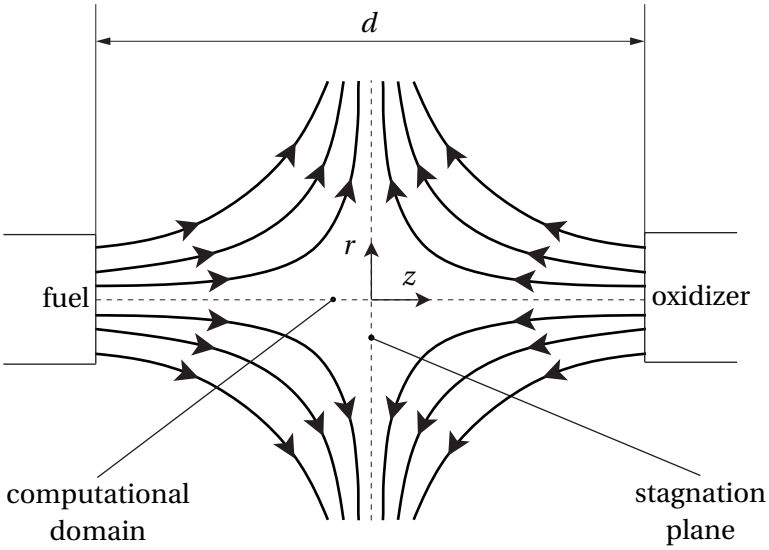


**Figure 3.9.:** Schematic view of the counterflow flame configuration.

$Y_{i,\mathrm{o}}$ are specified on the fuel and oxidizer boundaries. The distance between fuel and oxidizer inlets is defined as the domain size $d$.

The counterflow flame is defined by setting boundary conditions, grid size, operating pressure, and a chemical reaction mechanism. Unless specified otherwise, all counterflow simulations presented in this thesis rely on the same reaction mechanism as used for the jet flame simulation (Ó Conaire et al. [101] extended by Kathrotia et al. [72]).

Counterflow flames are commonly characterized by their strain rate $a$, which typically results from the boundary conditions. However, different definitions of the strain rate are used in the literature: $a$ can be determined from the mean axial velocity gradient [83], the maximum axial velocity gradient [136], the axial velocity gradient at the stoichiometric point [114], or the axial velocity gradient "before the flame" [83, 107, 116]. The latter corresponds to the boundary conditions in the potential flow setup where fuel and oxidizer are assumed to be infinitely far away[4]. Sometimes, radial velocity gradients are used instead [74]. If oxidizer and fuel do not have equal density, the strain rates on either side of the flame are dif-

[4] In the plug flow configuration, the potential flow boundary conditions can be approximated by

$$a_{\mathrm{f/o}} = \sqrt{\frac{\Lambda}{\rho_{\mathrm{f/o}}}} \tag{3.11}$$

for the fuel and for the oxidizer sides, respectively. This result can be obtained by reshaping Equation (3.35) from [108] or Equation (6.32) from [74].

ferent [83]. All of these definitions are approximately directly proportional to each other, see Figure 3.10. Only at high strain rates close to extinction, they deviate slightly from proportionality. In this study, the influence of strain is discussed qualitatively. Therefore, the maximum axial velocity gradient is chosen arbitrarily to characterize the strain rate. Nevertheless, attention has to be paid when comparing absolute results. Figure 3.10 also shows the inverse square of the flame thickness $\delta$, arbitrarily normalized by the factor 0.008. This quantity similarly scales as the strain rate (see also Equation (6.1)). The flame thickness thus is a similarly unique parameter as the strain rate.

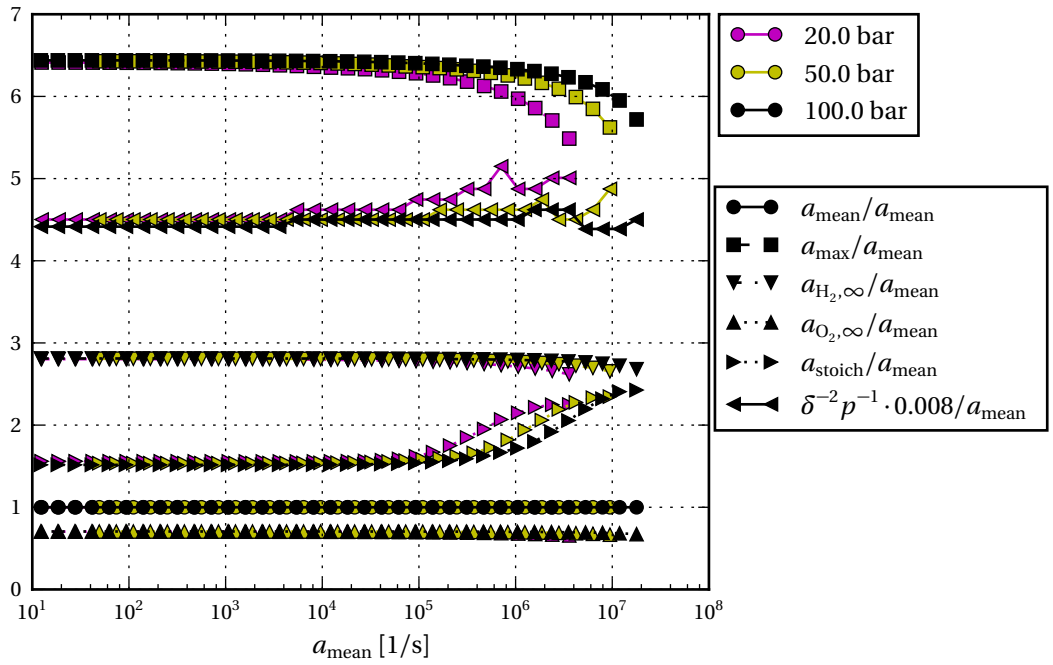


**Figure 3.10.:** Comparison of different (axial) strain rate definitions in a hydrogen-oxygen counterflow flame at different pressures and strain rates. $a_{mean}$ corresponds to the mean axial velocity gradient, $a_{max}$ to the maximum axial velocity gradient, $a_{H_2,\infty}$ and $a_{O_2,\infty}$ to the corresponding potential flow boundary condition strain rates on the fuel and oxidizer side, and $a_{stoich}$ to the axial velocity gradient at the stoichiometric surface. The flame thickness $\delta$ computed from the FWHM of the $H_2O$ profile is scaled appropriately and added to the diagram, indicating that it is a similarly unique parameter as the strain rate.

With all parameters defined, counterflow flames can be computed with standard software like OPPDIFF [91], Cosilab [119], FlameMaster [112], or Cantera [51]. These programs solve the underlying partial differential equations of the one-dimensional problem.

For this work, Cantera [51] is chosen to simulate the counterflow flames. This program is open source, providing access to all functions and fundamental equations. It is documented and well maintained by an active user group.

To compute counterflow flames at varying pressures and strain rates for the results presented in Section 6.2, separate simulations for each set of operating conditions have to be performed. Originally, this consumed a large amount of time and patience because the solution of the stiff set of equations is prone to diverge. In the course of this work, an optimized procedure was developed, published, and implemented into the Cantera source code [34, 32, 51]. This optimization provides a fast and reliable method to compute a batch of simulations. Additionally, a model was developed with the help of Andreas Rücker to include heat loss due to radiation and due to an arbitrary source in the counterflow simulation [122].

The volumetric heat release rate $\dot{q}$ of the counterflow flame is not accessible through Cantera by default. Instead, it is calculated manually from the steady-state solution following the approach by Ribert et al. [116]:

$$\dot{q} = \sum_i h_i \, M_i \, \dot{\omega}_{m,i} \tag{3.12}$$

with $i$ representing all species present in the reaction mechanism and $\dot{\omega}_{m,i}$ their molar volumetric production rates. As combustion consists of mostly exothermic reactions, the transformation of chemical energy to heat is associated with a negative value in $\dot{q}$.

# 4. OH* Radiation

Resting upon the literature review given in Section 2.4, this chapter presents the numerical and experimental investigation of OH* radiation. Three radiation models are employed to compute the OH* radiation. They are described first. Among them is the newly developed Equilibrium Filtered Radiation Model. To verify their applicabilities, the relevance of chemical and thermal excitation of OH* in non-premixed hydrogen-oxygen flames is investigated. The influence of pressure on both the emission and absorption is studied experimentally from a spectral and a wavelength-integrated perspective. This data is compared to the radiation calculated from the numerical simulation. The prediction quality of the simulation models is discussed.

## 4.1. OH* Radiation Modeling

Three different approaches to model the OH* radiation are used in this study: The Detailed Chemistry reaction mechanism approach using the chemiluminescence reaction rates from literature, the Spectral Modeling approach, and a self-derived Equilibrium Filtered Radiation Model (EFRM) [33]. All of these methods are described in the following. Their fundamental assumptions, abilities and restrictions are compared in Section 4.1.4.

### 4.1.1. Detailed Chemistry Radiation Model (DC)

This approach is essentially already described in Section 2.3.2. The basic assumption is that the radiation is directly proportional to the concentration of the excited species OH* (see Equation (2.13)). This naturally implies the assumption of optically thin gases and disregards any form of self-absorption. Additionally, no information on the spectrum is provided, but rather only the intensity of the bandpass-filtered radiation around 308.5 nm is calculated.

This method is only applicable to CFD simulations featuring a detailed reaction mechanism. The extension of the reaction mechanism to include OH* as a separate species has to be done before the start of the simulation. An additional equation for the species OH* has to be solved during the simulation run, thus increasing the

computational effort. As a benefit, the post-processing of the data is very simple: The radiation is assumed to be directly proportional to the OH* concentration, which can be extracted directly from the simulation.

The model depends on two sets of parameters: The reactions implemented for the radiation model including their corresponding Arrhenius parameters, and the thermodynamic data of OH*. Apart from the heat capacities, the latter data set provides the standard-state Gibbs free energy $g_m^{\ominus}(T)$ of OH* [73]. Its difference to the standard-state Gibbs free energy of ground state OH, denoted as $\Delta_{\mathrm{OH^*-OH}} g_m^{\ominus}$, is used to compute the equilibrium constant $K_c$ of the chemical equilibrium between OH* and OH [74, 4] (see Equation (2.19)).

The inclusion of thermodynamic data for OH* thus inherently provides the modeling of thermal excitation of OH*. Especially at high temperatures, the computed OH* concentration is determined by the specification of the thermodynamic data. In this thesis, the data provided by Burcat and Ruscic [15] is used, which is based on the molecular data by Huber and Herzberg [66]. This is recommended by Kathrotia et al. [72] in combination with their reaction rates.

The advantage of including OH* as a separate species in the detailed chemical reaction mechanism is that chemical excitation mechanisms can be included. By evaluating the reaction rates at runtime, non-equilibrium of OH* can be evaluated. As reviewed in Section 2.4.2, Reaction (2.21) is the dominant path of OH* formation in hydrogen-oxygen combustion. It is added to the detailed chemical reaction mechanism. Except for Section 4.2, in which the different chemical excitation rate specifications will be compared, the reaction rate specified by Kathrotia et al. [72] is used in this thesis. This includes the quenching rates by Tamura et al. [133], which not only provided the rates for thermal quenching but also the thermal excitation rates (see Section 2.3).

### 4.1.2. The Equilibrium Filtered Radiation Model (EFRM)

In the present study, the Equilibrium Filtered Radiation Model (EFRM) is proposed [33]. The idea behind this method is simple: If OH* is in equilibrium with its ground state OH, then the chemical excitation can be ignored. Consequently, no reaction rates are necessary and OH* does not have to be included in the detailed mechanism of the simulation. Instead, the concentration of OH* can be calculated directly from Equation (2.19), which in this case becomes:

$$\frac{[\mathrm{OH^*}]}{[\mathrm{OH}]} = K_c = K_p = \exp\left(-\frac{\Delta_{\mathrm{OH^*-OH}} g_m^{\ominus}}{R_m\, T}\right) \tag{4.1}$$

If the gas is assumed to be optically thin and self-absorption is therefore ignored, then the OH* concentration is again directly proportional to the OH* radiation.

This procedure can be even more simplified: The equilibrium between OH* and OH is not just a general chemical equilibrium between reactants and products, but in principle a thermal equilibrium between the first electronically excited state and the ground state. The relation between the concentrations of OH* and OH is then given by statistical thermodynamics [74]:

$$\frac{[\mathrm{OH}^*]}{[\mathrm{OH}]} = \frac{N_{\mathrm{OH}^*}}{N_{\mathrm{OH}}} = \frac{\tilde{g}_{\mathrm{OH}^*}}{\tilde{g}_{\mathrm{OH}}} \exp\left(-\frac{\Delta E}{k_B\, T}\right) \tag{4.2}$$

with $\tilde{g}^*_{\mathrm{OH}}$ and $\tilde{g}_{\mathrm{OH}}$ being the degeneracies of OH* and OH, respectively, which are constants and correspond to the number of sub-states in each state [4]. The energy difference $\Delta E$ varies depending on which actual transition occurs. However, if the excited state is simplified as a single state above the ground state, then the energy difference $\Delta E$ can be computed from Equation (2.11). Combining this assumption with the above equation, a qualitative relation for the OH* radiation can be derived:

$$e_{\mathrm{OH}^*} \sim [\mathrm{OH}^*] \sim [\mathrm{OH}] \cdot \exp\left(-\frac{h\, c}{k_B\, \lambda\, T}\right) \tag{4.3}$$

The wavelength $\lambda$ corresponds to the dominant wavelength of the radiation to be computed. For the comparison with measurements, the central wavelength of the optical filter employed (for OH*, 308.5 nm) should be used.

Equation (4.3) greatly simplifies the radiation modeling compared to the detailed chemistry model: The relation just relies on the temperature field, the ground state OH concentration field, physical constants, and the studied wavelength. The computation of the OH* concentration does not have to take place at runtime of the simulation, but instead can be applied as a post-processing step. Additionally, the simulation is even not required to account for all minor species. Reduced chemical mechanisms featuring OH are equally suitable, if temperature and OH are computed correctly.

### 4.1.3. Spectral Model (SM)

To obtain the wavelength-dependent radiation from the numerical simulation data, the spectrum of OH is modeled (see also Section 2.4.1). It relies on the fundamental assumption of thermal equilibrium. Qualitatively, spectral modeling is already applicable to equilibrium in rotational and vibrational states. This is a good approximation for all natural (particularly not laser-induced) radiation of OH, even in situations in which chemiluminescence dominates, with an exception being low-pressure hydrogen-air flames [21, 44–46, 49]. If additionally thermal equilibrium in the vibrational states is present, as it is the case for dominating thermal excitation, then the absolute values of the radiative quantities can be modeled.

In this study, the computation relies on the HITRAN/HITEMP database [121], which inherits the spectroscopic quantities summarized by Luque and Crosley [89, 90]. The database essentially provides the list of individual lines at reference conditions, their wavenumbers, pre-calculated line intensities, and FWHM of the pressure broadening. Additionally, the partition function of OH is supplied [4].

To couple the data base with the data from the numerical simulations, an object-oriented computer program is self-developed in Python. This is necessary for two reasons: First, the computation in HITRAN is bounded below 3000 K, and second, the available software is not object-oriented. The new tool is able to compute the absorption coefficient, emission coefficient, transmittance, absorptivity, emissivity, and radiance of a homogeneous cell. Input parameters for the computation of the absorption and emission coefficients are temperature, pressure, and OH mole fraction. For the calculation of line-of-sight integrated quantities like radiance or transmittance, the thickness of the cell is additionally required. The program follows the computational models described in the manuals of HITRAN on the Web [120] and SpectralCalc [43]. The lumped vibrational excitation temperature 4643.6 K and the lumped rotational excitation temperature 3.434 K of the partition function are obtained from fitting the partition function to the data provided by HITRAN [52]. The Voigt profile of the combined temperature and pressure broadening is implemented efficiently using the real part of a Faddeeva or Kramp function (see Section 2.2.1). The tool is able to blur the fine-resolution spectrum with a triangular or Gaußian kernel of arbitrary half-width to create spectra comparable to experiments with limited spectral resolution (For example, the laser used for the TDLAS measurements has a FWHM of 2 pm, which is larger than the typical simulation resolution). The implementation of the tool is verified by comparing the results for a broad range of test cases with the results from HITRAN on the Web (see Figure 4.1).

A wrapper class is implemented to compute the radiance, emissivity, and transmittance of a stack of homogeneous cells following the equations stated in Section 2.1. The cells are specified by their temperature, pressure, OH mole fraction, and thickness. They are assumed to be on a single ray with constant cross-section. This procedure is used to compute the overall radiance with self-absorption in the counterflow flame simulations. For the use with the two-dimensional jet flame simulations, only the absorption and emission coefficients computed from the base class are used.

To obtain the total radiation quantities, the wavelength-integration as described in Section 2.1.1 can be applied in combination with the transmittance of the filter used in the corresponding experiment.

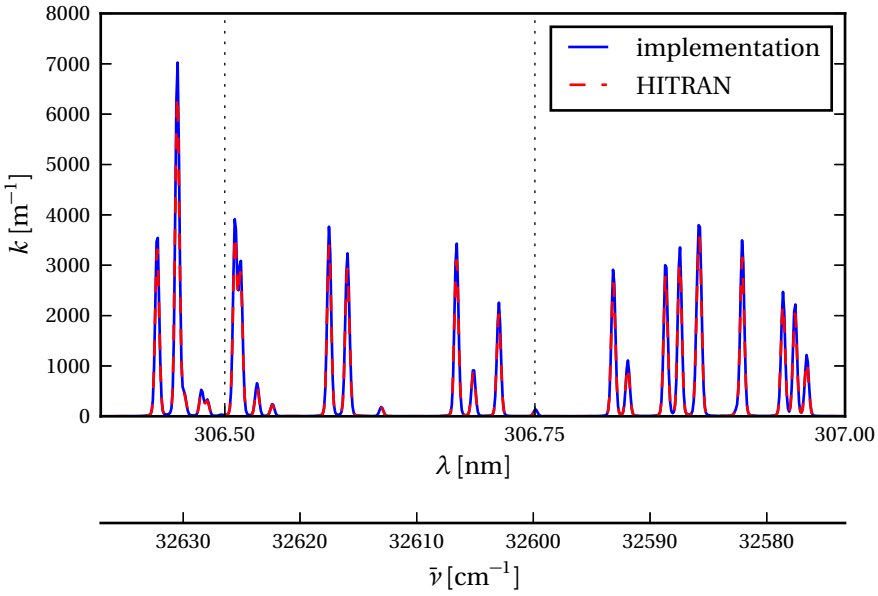


**Figure 4.1.:** Verification of the spectral modeling implementation: Absorption coefficient of 100% OH at 3000 K and 1 bar, computed from the Python implementation and "HITRAN on the Web" [120]. Both data rely on the HITRAN database [121].

### 4.1.4. Comparison of the Modeling Approaches

The different assumptions, output, and computational effort of the three radiation models used in this thesis are compared in Table 4.1. Thermal excitation of OH* is captured by all three models. The Detailed Chemistry model is the only one which can take chemical excitation into account, but has to be included early in the simulation process. The two other models can be applied as a post-processing step and only require the distributions of the temperature, pressure, and ground state OH concentration in the flame. The Spectral Model relying on the HITRAN database gives the most detail of the spectrum and is the only one which can accurately account for self-absorption (see Section 2.4.1), nevertheless with considerable computational effort. The Equilibrium Filtered Radiation Model has its advantage in its simplicity and ease of application.

All of these radiation models are well applicable to laminar flames which fully resolve the structure within the flame. In simulations of turbulent flames, in which the temperature and the OH concentration are usually averaged values, caution is necessary: The equations described in this section are highly non-linear. For example, Equation (4.2) depends exponentially on temperature. Its evaluation on ensemble-averaged quantities is not equal to the true ensemble average:

$$\overline{[\mathrm{OH}]\cdot\exp\left(-\frac{\Delta E}{k_B\,T}\right)} \neq \overline{[\mathrm{OH}]}\cdot\exp\left(-\frac{\Delta E}{k_B\,\overline{T}}\right) \tag{4.4}$$

| | DC | EFRM | SM |
|---|---|---|---|
| Spectral Resolution | no | no | yes |
| Absorption Modeling | no | no | yes |
| Chemical Excitation Modeling | yes | no | no |
| Applicable as Post-Processing | no | yes | yes |
| Simulation Data Requirement | Detailed Chemistry | OH, T | OH, T |
| Computational Effort | high | low | high |
| Prediction Quality at Low Optical Density | high | high | high |
| Prediction Quality at High Optical Density | low | low | high |

**Table 4.1.:** Comparison of the OH* radiation models.

To apply these models on simulations of turbulent flames, a method to account for the sub-grid distribution of OH concentration and temperature is necessary.

The next section will show that the assumption of thermal equilibrium between OH* and OH is indeed justified in hydrogen-oxygen flames. Therefore, all three radiation models are applicable. Their performance on modeling the emission and absorption will be evaluated in the subsequent sections.

## 4.2. Chemical vs. Thermal Excitation

As already mentioned in Section 2.4.2, OH* is known to be in thermal equilibrium above approximately 2700 K [42, 47, 63, 72, 77, 86, 144]. Nevertheless, this fact is widely unknown in the context of measuring combustion instability. To prove it, thermal and chemical excitation are quantitatively compared in this section.

The analysis is performed numerically based on counterflow flame simulations as described in Section 3.6. Since the turbulent combustion in liquid rocket engines is known to show flamelet character, the findings from these simulations are assumed to represent the real situation reasonably well.

Counterflow, non-premixed hydrogen-oxygen flames are simulated at various constant pressure levels. At each pressure, the influence of temperature on the formation of OH* is investigated. As most OH* radiation originates from the zone of highest temperature (see Section 6.2), the peak temperature of the counterflow flame is used for characterization. As in actual turbulent combustion, the peak temperature is controlled by varying the strain rate of the counterflow flame: At low strain rates, the peak temperature is close to the adiabatic flame temperature (and even exceeds it due to diffusion effects). With increasing strain, the peak temperature drops until the flame is extinct.

At each pressure, a batch of counterflow flame simulations with increasing strain rates is computed. This is implemented following the procedure described by Fiala and Sattelmayer [34], which provides an efficient and stable procedure for this task.

As only the formation of OH* is of interest for this analysis, self-absorption is not taken into account. The wavelength-integrated OH* emission of the flame is thus assumed to be directly proportional to the concentration of OH* molecules included in the extension of the detailed reaction mechanism (see Section 3.4 and 4.1.1).

The origin of the radiation is studied by considering the rates of formation of OH*. In the detailed chemistry mechanism, OH* can either be formed by a chemical reaction like $H + O + Q \longrightarrow OH^* + Q$ (Reaction (2.20)), or by the collision of ground-state OH with other molecules, $OH + Q \longrightarrow OH^* + Q$ (Reaction (2.14)).

Both types of reaction rates are included in the extension of the detailed reaction mechanism. While for the chemical excitation reaction a single set of (modified) Arrhenius parameters exists, the thermal excitation is given for each colliding molecule individually, taking into account the collisional cross-sections. The thermal excitation reactions are implemented as quenching reactions, i.e. of the form $OH^* + Q \longrightarrow OH + Q$. These reactions are reversible. The sum of all the reverse rates of these reactions is used to quantify the thermal production rate.

In Cantera, the production rates of each reaction are accessible at each point within the flame. To compare the overall contribution of both mechanisms, the flamelet-integrated quantities are calculated by integrating the local quantities over the grid (see also Section 6.2). This results in molar production rates per unit flame area (kmol $s^{-1}$ $m^{-2}$).

Figure 4.2 shows the thermal and the chemical production rates as a function of pressure and peak temperature. At low temperatures, chemical excitation clearly dominates and the thermal excitation is hardly noticeable. At about 2725 K, the chemical and the thermal production rates are of equal strength. Above this temperature, the thermal excitation further increases exponentially. This can be expected according to Equation (2.19). Thermal excitation governs the formation of OH* at higher temperatures. In this temperature range, the contribution of the chemical excitation becomes negligible.

The crossover temperature is insensitive to pressure. Close to the adiabatic flame temperature, both the chemical and the thermal excitation rates increase asymptotically. This is because a decrease of the strain rate in this region does not lead to an increase in peak temperature, but only to an increase in flame thickness. As the production of OH* is approximately proportional to the flame thickness (see Section 6.2), the steep increase in the production rates is explained. The relation between the thermal and the chemical production rates does not change in this part of the graph for single counterflow flame simulations.

The results obviously depend on the reaction mechanism. For the results in Fig-

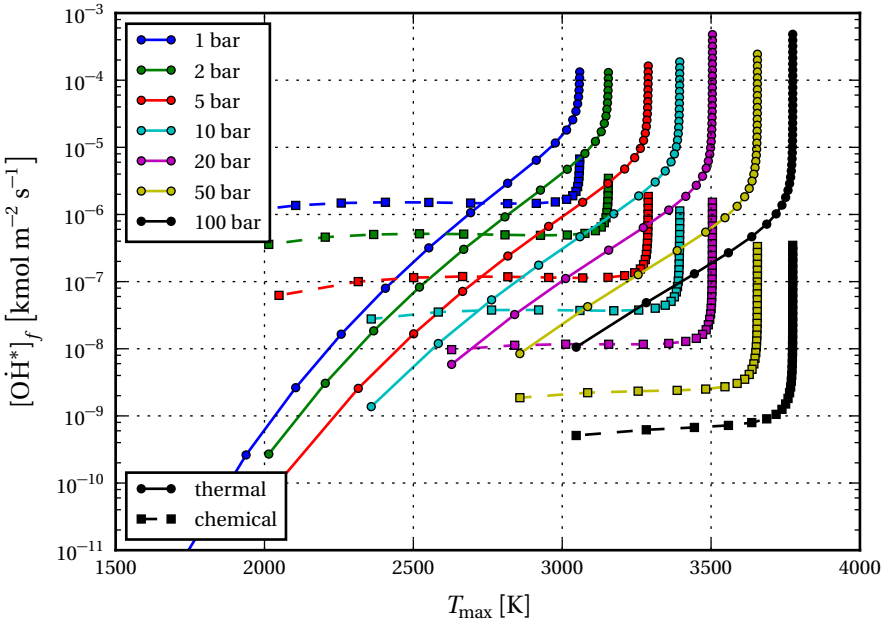


**Figure 4.2.:** Thermal vs. chemical excitation of OH* in counterflow hydrogen-oxygen flames. Base reaction mechanism by Ó Conaire et al. [101] and OH* extension by Kathrotia et al. [72].

ure 4.2, the OH* extension by Kathrotia et al. [72] is used on top of the Ó Conaire et al. [101] base reaction mechanism. This study was also performed for other OH* and base reaction mechanisms found in literature (including their additional chemical excitation mechanisms as noted in Table 2.1). Qualitatively, the graphs obtained show the identical behavior as plotted in Figure 4.2, an exception being the OH* extension by Dandy and Vosen [24], in which thermal excitation always dominates. The crossover temperatures for these combinations are given in Table 4.2. Generally, the crossover temperature is in the same range as shown in Figure 4.2. The base mechanism does not appear to have a great impact. This is reasonable as the flames are dominated by the diffusion effects, which are modeled in the same way for all cases. The crossover temperatures predicted by the different OH* extensions vary slightly. The highest crossover temperature is obtained when applying the Hall and Petersen [57] mechanism. However, the authors themselves state in a follow-up publication that their mechanism tends to over-predict chemiluminescence [111].

In agreement with the available literature, it can be concluded that OH* is mostly due to thermal excitation above 2700 K. With increasing temperature, the amount of thermal excitation grows exponentially, and the relative contribution of chemical excitation to the total excitation decreases. As rocket combustion typically occurs at temperatures well above 2700 K, it is reasonable to neglect chemical excitation and to assume only thermal excitation of OH*.

| Base mechanism | OH* mechanism | Crossover temperature |
|---|---|---|
| Ó Conaire et al. [101] | Kathrotia et al. [72] | 2725 K |
| Ó Conaire et al. [101] | Kaskan [71] | 2850 K |
| Ó Conaire et al. [101] | Hidaka et al. [63] | 2600 K |
| Ó Conaire et al. [101] | Koike and Morinaga [77] | 2475 K |
| Ó Conaire et al. [101] | Dandy and Vosen [24] | thermal always dominates |
| Ó Conaire et al. [101] | Smith et al. [127] | 2650 K |
| Ó Conaire et al. [101] | Hall and Petersen [57] | 2900 K |
| Jachimowski [67] | Kathrotia et al. [72] | 2725 K |
| GRI-Mech 3.0 (subset) [125] | Kathrotia et al. [72] | 2725 K |
| Konnov [78] | Kathrotia et al. [72] | 2725 K |

**Table 4.2.:** Crossover temperatures above which thermal excitation exceeds chemical excitation of OH* for various combinations of base and OH* detailed chemical reaction mechanisms.

## 4.3. Absorption

Although the focus of this thesis is on the emission, the absorption of hydroxyl in the UV is described first. This is due to the fact that absorption can be measured directly, whereas the interpretation of the emission data always relies on the knowledge of (self-)absorption (see Section 2.4.1).

This section generally describes the amount and importance of absorption and additionally assesses the predictive power of its modeling. Only the Spectral Model (Section 4.1.3) is considered as it is the single one which provides absorption data.

The absorption of the jet flame experiment is measured in two ways: First, the absorption of a small band is measured spectrally at a high resolution using TDLAS. These measurements are performed along a single line of sight. Second, the band-pass filtered absorption is measured, which does not provide spectral, but a spatial resolution.

### 4.3.1. Spectral Absorption

The spectral absorption is measured using Tunable Dye Laser Absorption Spectroscopy (TDLAS). The setup is described in Section 3.3.4. All measurements are conducted along a single laser beam passing through the center of the flame 5 mm above the burner (see Figure 4.3). Due to the three-dimensional flame structure, the spatial structure cannot be resolved. Instead, the transmittance along the line of sight is measured.

Spatial resolution is not possible because of the three-dimensional flame structure, but only the transmittance integrated along the line of sight is measured.

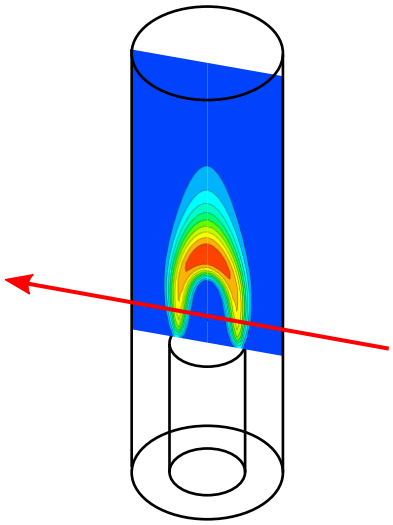

**Figure 4.3.:** Illustration of the TDLAS laser beam path through the flame. The contour image represents a radial slice of the ground state OH mass fraction at 5 bar.

Experimentally, the transmittances are obtained by dividing the wavelength-dependent radiance measured by the measurement diode with the flame burning by the radiance measured with the flame turned off. The wavelength is adjusted by the dye laser through an internal control[1].

Beam steering caused by the inhomogeneous refractive index within the hot flame is small due to the small dimensions of the flame, but, nevertheless, has a significant impact on the measured transmittance: The slight aberration of the beam by few micrometers already causes a reduction (or even slight increase) of the radiance recorded by the measurement diode. This problem is addressed by studying the transmittance at 282.76 nm. OH has no absorption line close to this wavelength. Therefore, no absorption should take place and ideally the transmittance should be unity. In reality, beam steering results in a deviation. To segregate this effect, the

[1] The laser measures the wavelength with respect to the speed of light in air. To obtain the wavelength in vacuum as it it specified in the HITRAN database, the wavelength output of the laser has to be modified by the refractive index of air (derived from Equation (2.11)):

$$\lambda_{\mathrm{vac}} = \frac{c_{\mathrm{vac}}}{c_{\mathrm{air}}} \lambda_{\mathrm{air}} = n_{\mathrm{air}}\, \lambda_{\mathrm{air}} \tag{4.5}$$

The refractive index of air $n_{\mathrm{air}}$ can be computed from the modified Edlén or Ciddor formulae [129, 90]. In this work, the refractive index $n_{\mathrm{air}} = 1.0002943$ is used, which causes a wavelength shift of approximately 83.3 pm in the investigated wavelength range.

calculated transmittances are scaled to reach unity averaged over a wavelength band of 0.1 nm around 282.76 nm. The refractive index distribution is assumed to be constant over the small wavelength band studied. By applying the scaling on the entire wavelength band, the effect of beam steering is removed.

The measurements of the radiance transmitted through the flame are conducted at atmospheric conditions as well as a set of elevated pressures up to 31.5 bar. At each pressure level, up to ten measurements are recorded and averaged. The transmittances are computed by dividing these values by the measured radiance at the measurement diode with the flame turned off. The results are shown in Figure 4.4(a).

Seven absorption lines of the $v = 1 \rightarrow v = 0$ system of OH can easily be identified in the experimental data: The $R_2 14$ line at 282.900 nm, the $Q_2 2$ line at 282.921 nm, the $Q_1 6$ line at 282.949 nm, the $Q_2 3$ line at 282.958 nm, the $R_1 15$ line at 283.011 nm, the $P_1 3$ line at 283.033 nm, and the $Q_2 4$ line at 283.057 nm (all wavelength as measured in air). The position of the line centers remains constant over pressure. The $Q_1 6$ and the $Q_2 3$ lines are only separable at low pressure levels. With increasing pressure, the lines overlap more and more. Generally, the absolute absorption as well as the line width become stronger and wider with pressure. This is reasonable, as more OH molecules are within the optical path at higher pressures, and the optical thickness therefore increases. Pressure broadening increases naturally with pressure, leading to thicker lines (see Section 2.2.1). Additionally, the flame temperature increases with pressure, causing higher Doppler broadening.

The data is compared to the transmittances obtained from the spectral simulation shown in Figure 4.4(b). The data is based on the CFD simulation of the jet flame described in Section 3.4. The mole fractions of OH, the temperature, and the pressure along the path of the laser beam are extracted. For this step, the effect of the azimuthal flame curvature is neglected, because the laser beam is thin compared to the flame radius. The CFD data is fed into the spectral simulation tool described in Section 4.1.3, which yields the transmittance of the flame as a function of the wavelength in vacuum. To produce results with a resolution comparable to the experiment, the simulated data is blurred with a Gaußian kernel with a FWHM of 2 pm, representing the spectral half width of the laser beam given by the manufacturer. This procedure is applied to simulations closest to the pressure levels studied in the experiment.

The simulation results agree well with the experimental data: The same lines can be identified in the simulated spectra. The trend of increasing absorption and broader lines with pressure is captured as well. However, the absolute wavelengths of the lines do not coincide. Instead, there appears to be a constant shift of approximately 23 pm compared to the experimental data. This is due to the wavelength accuracy of the laser, which is stated to be within 30 pm by the manufacturer, and combined with the uncertainty of the refractive index of air needed to convert the vacuum

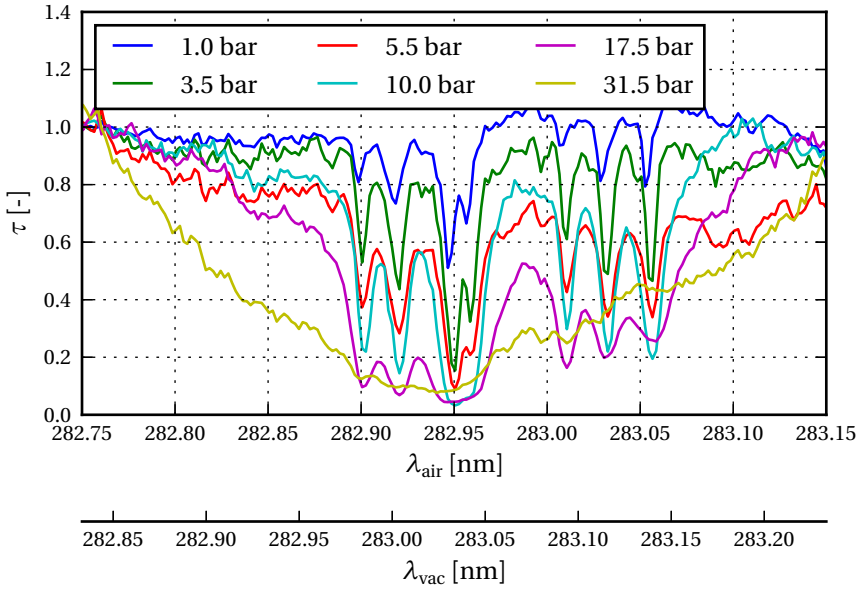


**(a)** Experiment

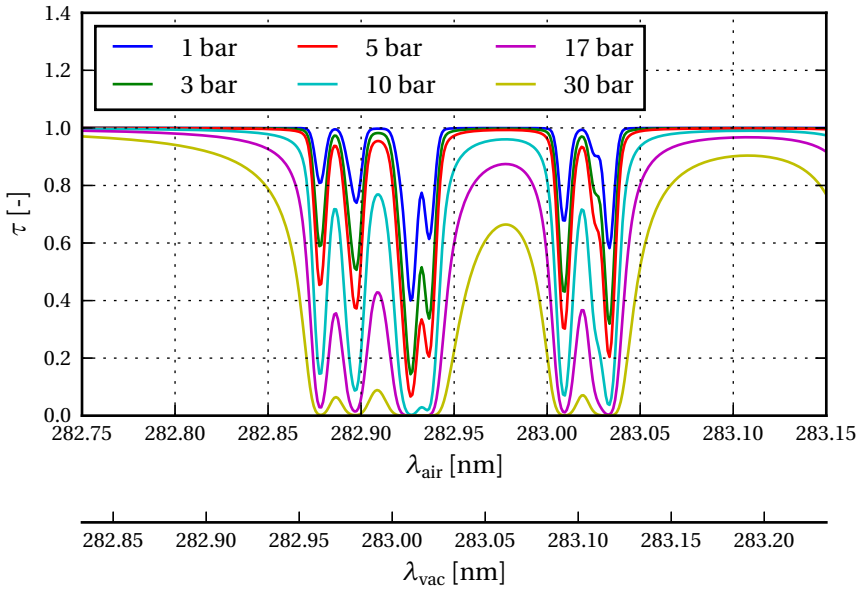


**(b)** Simulation

**Figure 4.4.:** Transmittance of the jet flame between 282.75 nm and 283.15 nm 5 mm above the lance. Experimental results from the TDLAS measurements, simulation results from the spectral modeling (Section 4.1.3).

wavelength to the wavelength in air. If the experimental spectrum is shifted by 23 pm, as shown in Figure 4.5 for 10 bar, the transmittance spectra overlap almost perfectly. Quantitatively, the absorption is slightly over-predicted, which, however, is also due to the systematic contribution of experimental noise at low signal intensities. The measurement around 31.5 bar does not fit into the overall picture: The peak absorption is lower than at lower pressures, and the absorption is much wider than predicted in the simulation. The reasons for this behavior cannot be explained by this study.

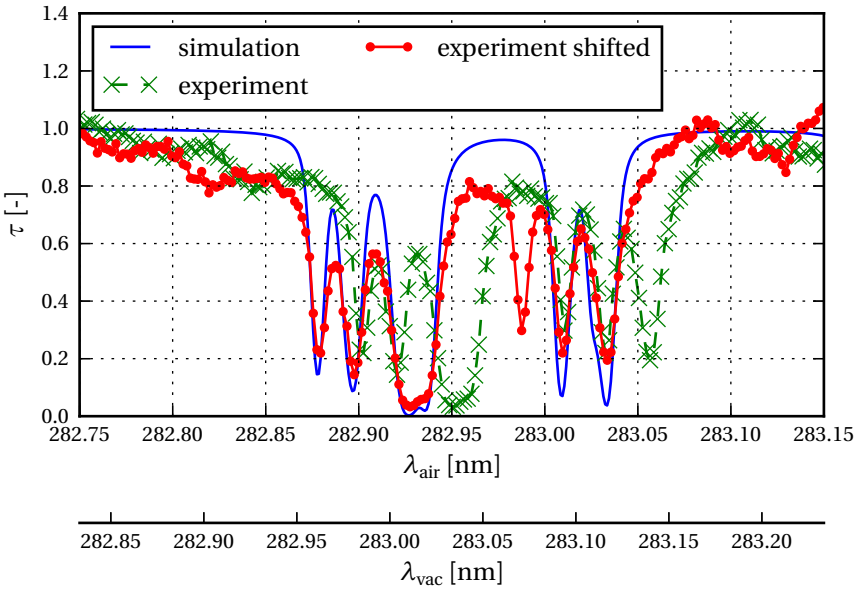


**Figure 4.5.:** Transmittance of the jet flame between 282.75 nm and 283.15 nm 5 mm above the lance at 10 bar. Comparison between data from the TDLAS experiment and from spectral simulation. The "shifted" experimental results are arbitrarily shifted by 23 pm.

A notable difference in the simulated spectrum compared to the experimental data is the $R_1 15$ line at 283.011 nm: This single line does not appear significantly in the simulated spectrum. However, this appears to be an error in the underlying HITRAN database, in which a very low line strength is associated with this line. Both the data collected by Dieke and Crosswhite [28] as well as the LIFBASE [90] program present values matching the experimental observations in this study.

### 4.3.2. Filtered Absorption

Additionally, the spatial absorption of the flame is measured. This is achieved by the setup described in Section 3.3.3. Due to the use of the band-pass filter around

308.5 nm (Figure B.1), the wavelength-dependent information is lost. Instead, only wavelength-averaged transmittances are measured according to Equation (2.10).

The combination of the detection setup featuring an optical chopper and appropriate filtering in the post-processing routines removes the influence of the flame's self-radiation and provides the transmitted radiance only. However, during the measurements, the intensified camera records the superposition of the background radiation and the radiance of the flame. To avoid the signal loss due to over-exposure, the gating time and gain of the image-intensifier has to be adjusted such that the maximum overall intensity does not exceed saturation. In the present case around 308.5 nm, the flame radiation is much more intense than the background, even though a 500 W Hg(Xe) lamp with a strong radiation in the UV is used. The background contributes to the recorded signal only up to 10%, in many regions even below 1%. Although 2048 sample images are taken for each pressure, this level is prone to random noise as well as to the uncertain linearity of the camera in this region. Especially at elevated pressures, the intense infrared radiation of the flame further increases the camera noise.

As in the previous section, the transmittances are obtained by dividing the measured radiance transmitted through the flame by the radiance with the flame turned off. The result is shown for four pressure levels in the Figures 4.6 and 4.7.

Unfortunately, due to the mounting of the quartz diffuser, the base of the flame is not illuminated by the background. Instead, the diffuser starts 3 mm above the lance, and additionally shows an impurity 6 mm above the lance, visible as a slightly diagonal line in the results. The effect of beam steering is visible at the edges of the quartz tube and diffuser.

While almost fully transparent at atmospheric conditions, the flame zone becomes more and more opaque with increasing pressure. At 30 bar, only 25% of the background radiation is transmitted through the center of the flame.

The experimental data is compared to the transmittance computed from the numerical simulation. Similar to the procedure described in the previous section, the spectral absorption coefficient of the flame is computed from the simulated radial profiles of temperature, pressure, and OH mole fraction using the self-developed spectral modeling software described in Section 4.1.3. Along the line of sight associated with each camera pixel, the wavelength-dependent transmittance is computed according to Section 3.5. Finally, the wavelength-integrated transmittance corresponding to the experiment is obtained by multiplication with the spectral radiance of the lamp provided by the manufacturer and the filter curve, see Equation (2.10).

Qualitatively, the simulation agrees well with the experimental data. Quantitatively, significantly higher transmittances are predicted from the simulation. This deviation can be due to two effects: First, the data for the spectral radiance of the lamp provided by the manufacturer is very sparse and states only four data points

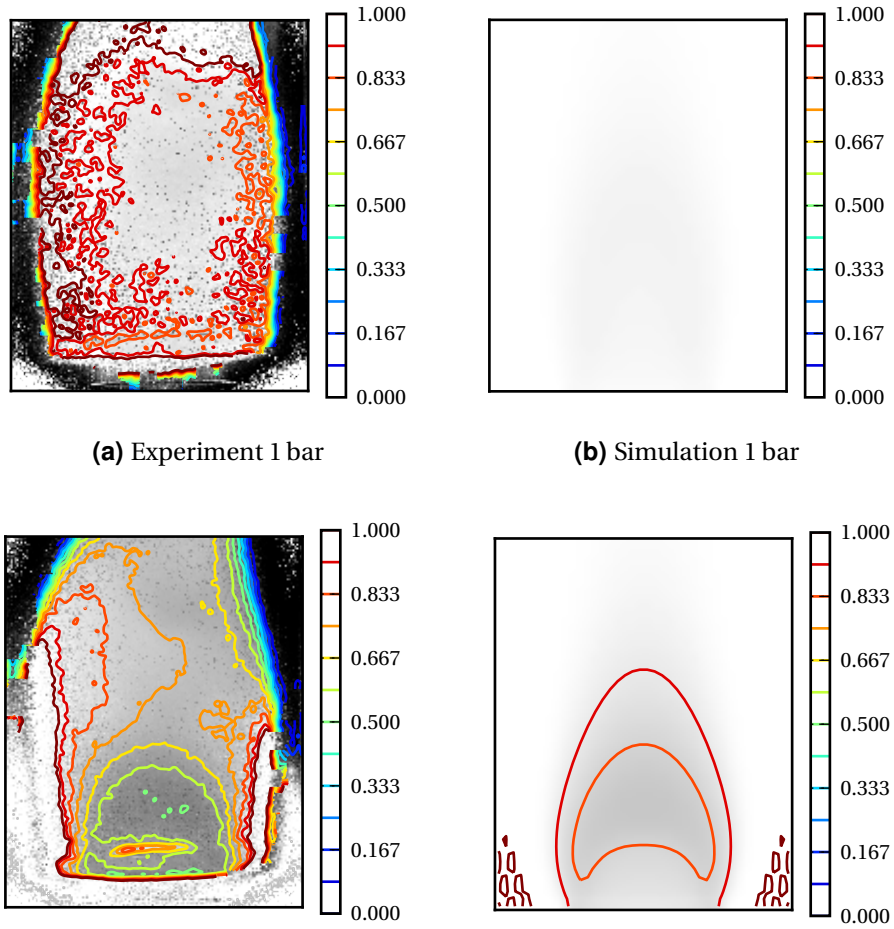


**(a)** Experiment 1 bar

**(b)** Simulation 1 bar

**(c)** Experiment 10.22 bar

**(d)** Simulation 10 bar

**Figure 4.6.:** OH* transmittance of the Hg(Xe) lamp radiation through the flame, filtered by the 308.5 nm band-pass filter (see Figure B.1). Data at 1 and 10 bar.

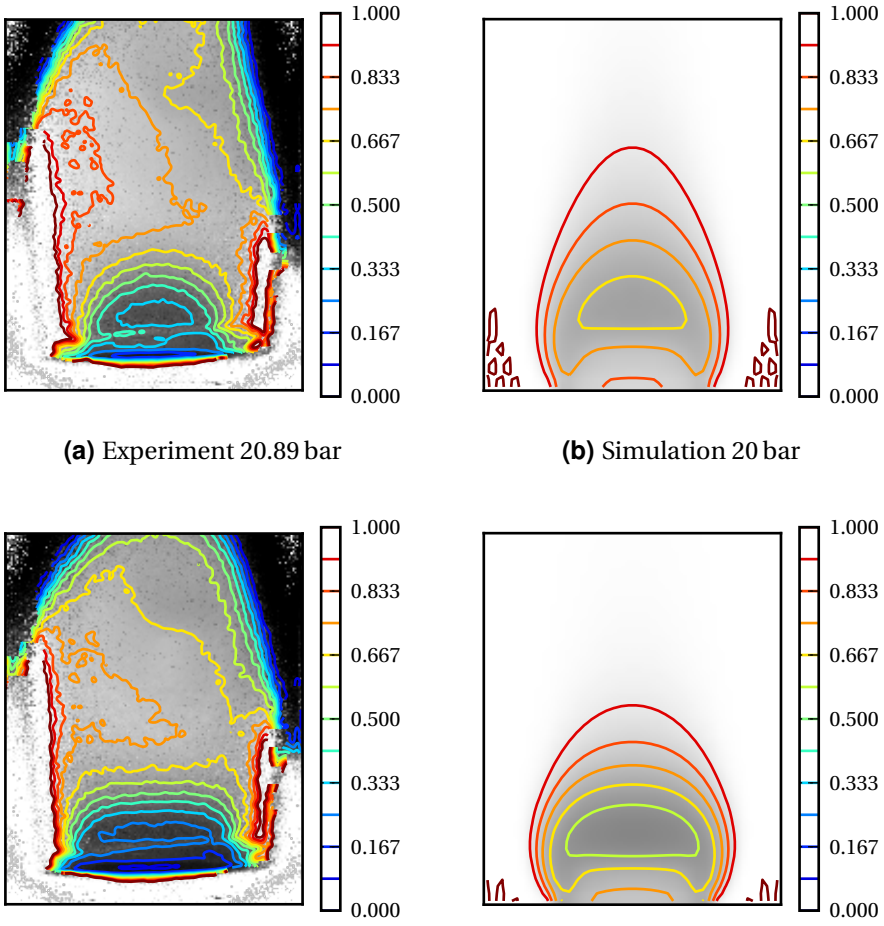


**(a)** Experiment 20.89 bar

**(b)** Simulation 20 bar

**(c)** Experiment 29.73 bar

**(d)** Simulation 30 bar

**Figure 4.7.:** OH* transmittance of the Hg(Xe) lamp radiation through the flame, filtered by the 308.5 nm band-pass filter (see Figure B.1). Data at 20 and 30 bar.

within the investigated wavelength range. In reality, the lamp has a pronounced fine-structure. Depending on the overlap of the spikes in the lamp spectrum with the absorption lines, the value of the wavelength-integrated transmittance is considerably influenced. Second, there is the undefined measurement deviation due to beam steering and the unknown camera sensitivity in this range described in the above paragraphs. Even in regions far away from the flame where there should be little to no absorption, transmittances of 60% or less are obtained. This is in agreement with the generally lower transmittances within the flame compared to the simulation. Therefore, the quantitative values have to be treated with care.

It is important to note that the absorption investigated in this section is not the absorption of the flame's own radiation, but the absorption of the background light source filtered around 308.5 nm. Due to the wavelength-unspecific nature, the quantitative values of the transmittance are irrelevant for the further analysis. This is the reason why no further effort has been made to improve the presented results. Nevertheless, the trend to substantial absorption is visible and the general shape of the transmittance computed by the Spectral Modeling is confirmed.

### 4.3.3. Relevance of Absorption for OH* Radiation

The TDLAS results shown are in good agreement with the Spectral Modeling performed on the numerical data. The filtered absorption measurement qualitatively confirms the spatial distribution. Quantitatively, absorption of OH is proven to have a significant impact on hydrogen-oxygen flames at elevated pressure and temperature.

Absorption is a phenomenon which strongly depends on the wavelength: The TDLAS measurements show 97% attenuation of the $v = 1 \rightarrow v = 0$ $Q_1(6)$ line at 10 bar, whereas radiation at other wavelengths is almost fully transmitted even at higher pressures. The TDLAS measurements are performed in the relatively low-absorption $\Delta v = 1$ band around 283 nm. The stronger $\Delta v = 0$ band around 308.5 nm is predicted to have even higher absorption. This is also evident in the filtered absorption measurement: Even though the radiation passing through the flame shows a broad-band spectrum and a large part not associated with OH absorption lines is greatly transmitted, the filtered transmittance is significantly reduced because of the severe absorption of the single spectral lines.

Most relevant for the interpretation of the flame's own radiation is not the absorption of radiation at arbitrary wavelength, but the absorption at the wavelength at which the flame radiates itself. The emission and absorption spectrum of a radical show the same distribution. Therefore, most radiation of an excited molecule is emitted at wavelengths at which there is also high absorption. The impact of self-absorption is, therefore, considerably more severe than absorption of a broad-band

radiation as investigated in the previous section.

The amount of self-absorption varies significantly within the spectrum. To illustrate this, the radiances of the strong $v = 0 \rightarrow v = 0$ $Q_1(7)$ line at 309.06 nm and the weak $v = 3 \rightarrow v = 2$ $P_2(15)$ line at 305.13 nm are compared in a theoretical numerical experiment: A homogeneous flame is considered, in which temperature and species composition are computed from adiabatic stoichiometric combustion of hydrogen with oxygen using Cantera. The radiances computed from Spectral Modeling, which account for self-absorption, are plotted as a function of flame thickness in Figure 4.8 for four pressures and for both wavelength. Additionally, the bandpass-filtered radiance around 308.5 nm is computed.

If self-absorption was negligible, then the radiance would increase linearly with flame thickness. This is approximately the case for the weak $v = 3 \rightarrow v = 2$ $P_2(15)$ line at 1 bar. At higher pressures, an increasing deviation from proportionality is observed: The thicker the flame is, the more radiation is attenuated within the flame and the less is effectively emitted. For the filtered radiation and even more for the single strong line, the effect is already visible at atmospheric pressure. At 100 bar, a 10 mm long flame emits more than 80% of the radiation a 100 mm thick flame. For the strong $v = 0 \rightarrow v = 0$ $Q_1(7)$ line, the emitted radiance does not increase significantly after just 0.25 mm at 100 bar. Therefore, at elevated pressures, self-absorption determines the region from which OH* radiation is recorded.

To quantitatively transfer the experimental findings of this section to arbitrary flames, three parameters have to be compared: The length of the optical path through the flame, the mole fraction of ground state OH, and the pressure. All of these enhance absorption. The parameters result from the Lambert-Beer law combined with the definition of the absorption coefficient (see Sections 2.1 and 2.2.2). The experimental results show a significant influence of the absorption at a laboratory scale flame with a half width of the OH concentration of approximately 10 mm. In practical flames with typically thicker luminous zones, the effect is even more important.

## 4.4. Emission

With the absorption spectrum of OH clarified, its emission in the jet flame experiment can be studied thoroughly. In this section, measurements of the flame spectrum, the spatial profiles, and the influence of pressure are presented. The data is compared with the results obtained from the different radiation models and their performance is assessed.

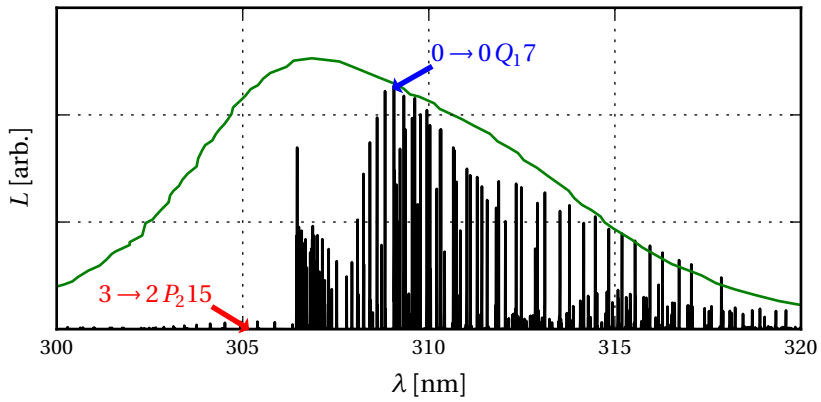


**(a)** Selection of the lines. The green line indicates the filter transmittance.

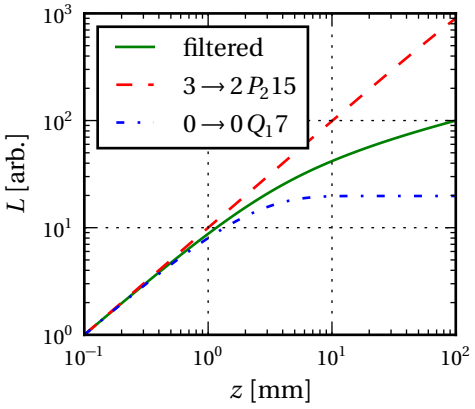


**(b)** 1 bar

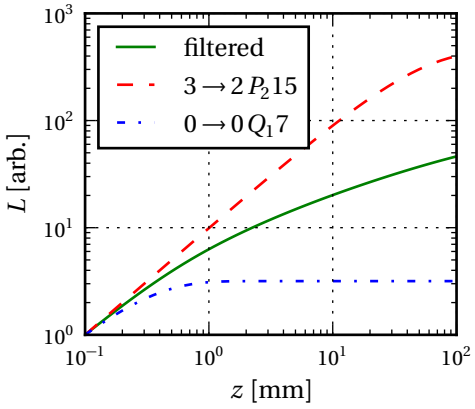


**(c)** 10 bar

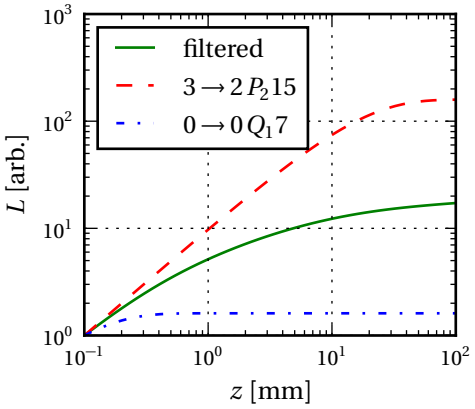


**(d)** 60 bar

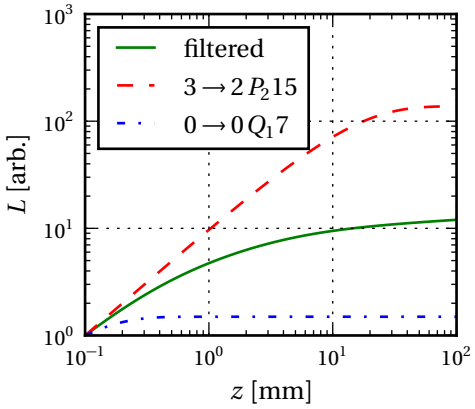


**(e)** 100 bar

**Figure 4.8.:** Simulated radiance $L$ of a theoretical flame as a function of flame thickness $z$ for two individual lines and the radiance filtered by the 308.5 nm band-pass filter.

### 4.4.1. OH* Radiance Spectrum

The spectrum of the flame is recorded using the setup described in Section 3.3.2. A horizontal slice 5 mm above the burner is resolved radially and spectrally. Two gratings with 150 grooves/mm and 2400 grooves/mm are used to record a coarse and a fine spectrum, respectively. The coarse spectrum is mainly of interest for the discussion of the blue radiation and is, therefore, presented in Figure 5.2 on page 76.

The OH* spectrum shows the typical shape as known from literature ([49], Section 2.4.1) with the $\Delta v = 1$ bands around 285 nm, the $\Delta v = 0$ bands around 310 nm, and the $\Delta v = -1$ bands around 330 nm. The intensity of the entire OH* spectrum increases strongly with pressure, see also Section 4.4.3.

To gain further insight and to discuss the modeling results, the fine spectrum of the flame at 12 bar around 310 nm is shown in Figure 4.9 between 305 nm and 318 nm. The experimentally observed line-of-sight integrated radiance is plotted in a false-color image as a function of the horizontal coordinate $y$ and the wavelength.

The image is compared to the radiance $L$ computed from Spectral Modeling, which naturally is the only method to resolve the radiation spectrally. From temperature, pressure, and ground state OH mole fraction of the CFD simulation, the wavelength-dependent absorption and emission coefficients are computed at each radial and axial position. The line-of-sight integrated radiance as a function of the horizontal coordinate $y$ is then calculated as described in Section 3.5.

To better illustrate the performance of the radiation model, the radiances are integrated along the horizontal coordinate $y$. The resulting radiances are a function of only the wavelength and shown in Figure 4.9(b). As the measured quantities are not absolute values, the spectra are normalized by their maximum values. Generally, very good agreement between the experimental data and the simulated radiance can be observed.

Additionally, a third curve is plotted in Figure 4.9(b): It represents the emission coefficient $e$ obtained from Spectral Modeling (see also Section 2.1). It is computed in the same way as the radiance $L$, but does not take into account self-absorption. The spectrum of the emission coefficient $e$ is again normalized by its maximum value. Comparing the data with the experiment, good correlation is observed for wavelength below 312 nm. Above, the emission coefficient significantly under-predicts the recorded radiance. In this region, the radiance is dominated by transitions between the vibrational states $v = 1 \rightarrow v = 1$, whereas below 312 nm the transitions are between the vibrational states $v = 0 \rightarrow v = 0$. OH molecules with the vibrational state $v = 0$ have a much higher number density than with the vibrational state $v = 1$. Therefore, the $v = 0 \rightarrow v = 0$ transitions are substantially more attenuated by self-absorption than the $v = 1 \rightarrow v = 1$ transitions. In Figure 4.9(b), the values are

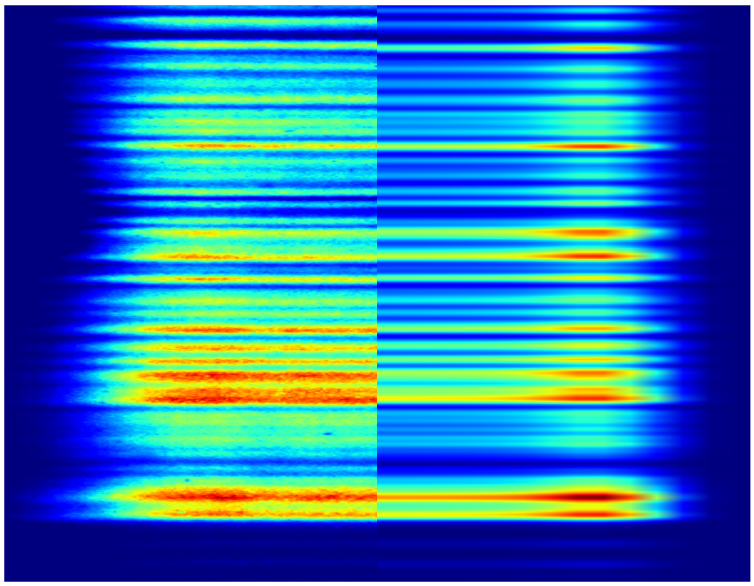

**(a)** Experimental spectrum (left half) vs. Spectral Modeling radiance, blurred with a 65 pm FWHM Gaußian kernel (right half).

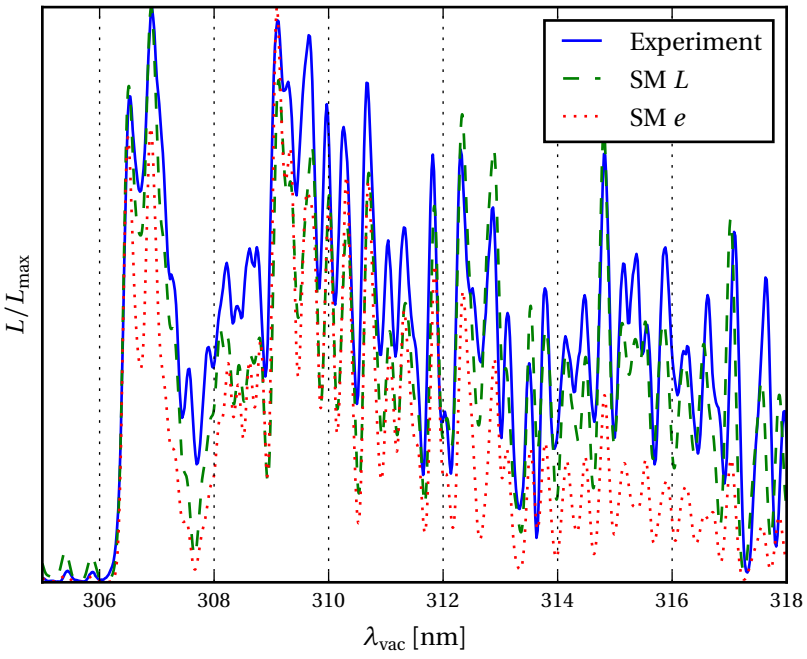


**(b)** Radially integrated spectra.

**Figure 4.9.:** OH* radiance spectrum of the jet flame experiment. The recording shows a radial slice 5 mm above the lance. Data at 12 bar.

normalized, which is why the values of the dominating $v = 0 \rightarrow v = 0$ transitions are well represented. In reality, the less self-absorbed $v = 1 \rightarrow v = 1$ transitions therefore appear to be relatively stronger in the experiment compared to the emission coefficient.

### 4.4.2. Spatial Filtered OH* Radiance

The line-of-sight integrated radiances of the flame recorded from the side give insight into the spatial structure. To provide two-dimensional data, the camera is equipped with the 308.5 nm band-pass optical filter instead of a spectrograph. The wavelength thus cannot be resolved.

The radiances of the flame at different pressures is shown in Figure 4.10. Originally being an elongated flame, it becomes shorter with increasing pressure. Along with the increase in pressure, the outflow velocities decrease inversely because of the constant mass flow rate. The gravitational effect which relatively increases with pressure pushes the flame towards a narrow zone above the lance. This trend is also visible in the numerical data. Above approximately 33 bar, the velocities are so low that slight disturbances cause the flame to become unstable and start to flicker.

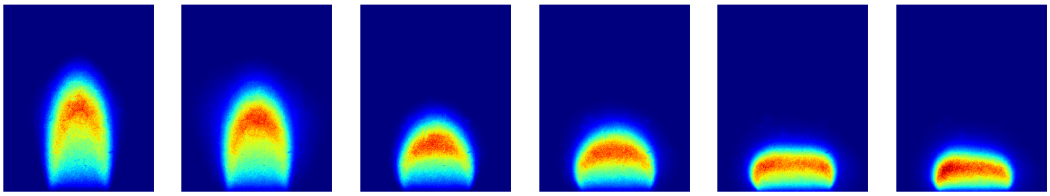

**(a)** 1 bar **(b)** 5 bar **(c)** 12 bar **(d)** 19 bar **(e)** 31 bar **(f)** 39 bar

**Figure 4.10.:** Filtered, line-of-sight integrated OH* radiation at different pressure levels.

As shown in Section 4.3, the OH* radiation suffers from severe self-absorption at elevated pressures, which strongly depends on the individual spectral lines. An Abel-type inverse transform to obtain the radial profiles is only possible in the presence of self-absorption if the absorption coefficient is constant over the measured wavelength. The optical band-pass filter used has a FWHM of 10 nm, thus containing the information of many spectral lines. The absorption among these lines is very different. Therefore, an accurate Abel-type inverse transform is not possible. Accordingly, only line-of-sight integrated data of the OH* radiation are presented in this sub-chapter.

All three radiation modeling approaches presented in Section 4.1 aim to compute the filtered flame radiation. Therefore, all of them can be compared to the experimental data. The values computed by the Spectral Modeling approach are cal-

culated in the same way as in the previous section, but for each height of the flame. The band-pass filtered radiation is finally computed by integrating the wavelength-dependent data with the filter curve. Like in the previous section, both the radiance $L$ and the integrated emission coefficient $e$ are presented to indicate the importance of the self-absorption.

Both the Detailed Chemistry approach and the Equilibrium Filtered Radiation Model naturally cannot account for self-absorption. The radiances predicted by these models are, therefore, obtained by performing the geometrically modified forward Abel transform based on the radially computed data without taking into account any absorption.

The results of the three models are presented in Figure 4.11 for 12 bar. All data are normalized by their peak values, as the radiation models always produce qualitative emissivities (see Section 4.1). Further pressure levels are shown in Appendix C. All three radiation models predict the general shape very well. However, the simulated radiation peaks a little too far downstream compared to the experiment. This behavior is observed for all radiation models. As they all rely on the same fundamental numerical simulation, this appears to be due to the underlying data.

Comparing the Detailed Chemistry, EFRM, and Spectral Modeling $e$ results, almost identical shapes are produced. All three models have the same fundamental assumption of no self-absorption. The equality of the Detailed Chemistry and the EFRM data again confirms the result of Section 4.2 that the chemical excitation included in the Detailed Chemistry model is negligible compared to the thermal excitation.

The Spectral Modeling of the radiance $L$, however, produces a little different result. This is due to the inclusion of self-absorption. Spatially, the absorption results in a reduction of radiation in the peak regions of the flame. Normalized by the maximum value, radiation in regions of lower attenuation appear amplified. This can clearly be seen in the inner region of the flame near the flame foot. The effect is visible both in the experimental data and the Spectral Modeling $L$. While almost negligible at atmospheric conditions, it becomes stronger with increasing pressure.

### 4.4.3. Overall Filtered OH* Radiance

In the previous sub-sections, the radiances were always presented referenced to their maximum value in each case. While absolute radiance measurements are not achievable with the equipment in use, the relative radiances between various pressure levels can, nevertheless, be compared.

To present a meaningful parameter, the overall wavelength-, radially-, and axially-integrated radiance is measured at each pressure level. This quantity is shown in Figure 4.12. The values are normalized by the radiance at 5 bar. At each pressure

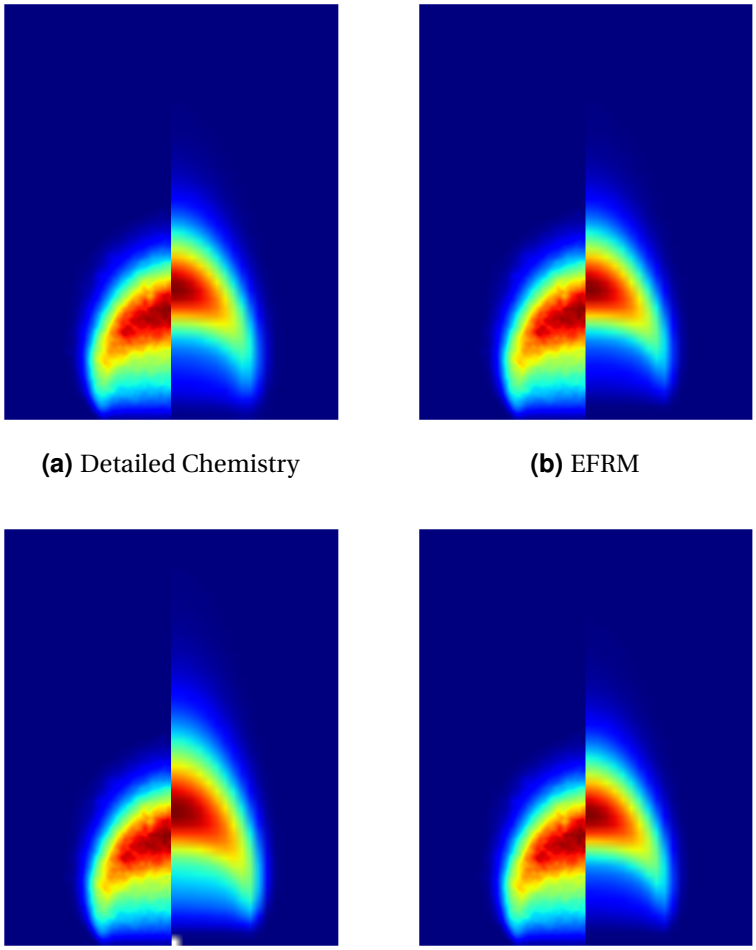

**(a)** Detailed Chemistry

**(b)** EFRM

**(c)** Spectral Modeling $L$

**(d)** Spectral Modeling $e$

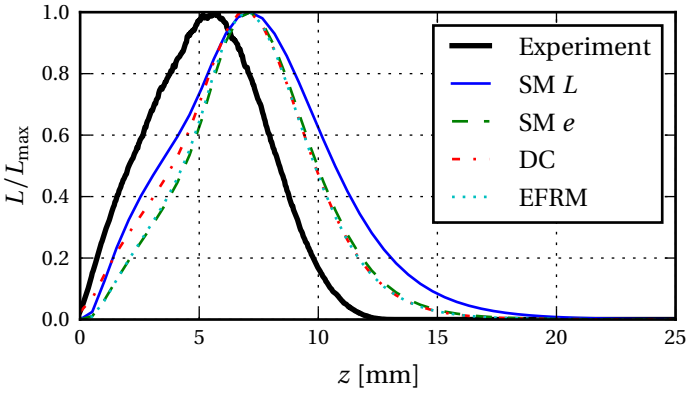


**(e)** Radially integrated radiances over flame height $z$

**Figure 4.11.:** Filtered, line-of-sight integrated OH* radiances. Experimental, normalized data is shown on the left sides of the four images. The right sides show the radiance modeling data. Pressure in the experiment: 12.2 bar, pressure in the simulation: 12 bar.

level, 204 pictures of the flame are recorded. The presented values represent the average overall radiances of each measured pressure. The standard deviation in both the overall radiance and the pressure is plotted as error bars in Figure 4.12. The significant error bars at approximately 35 bar and 40 bar indicate the flickering and the unstable behavior of the flame at these pressure levels. Therefore, their values have to be treated with care.

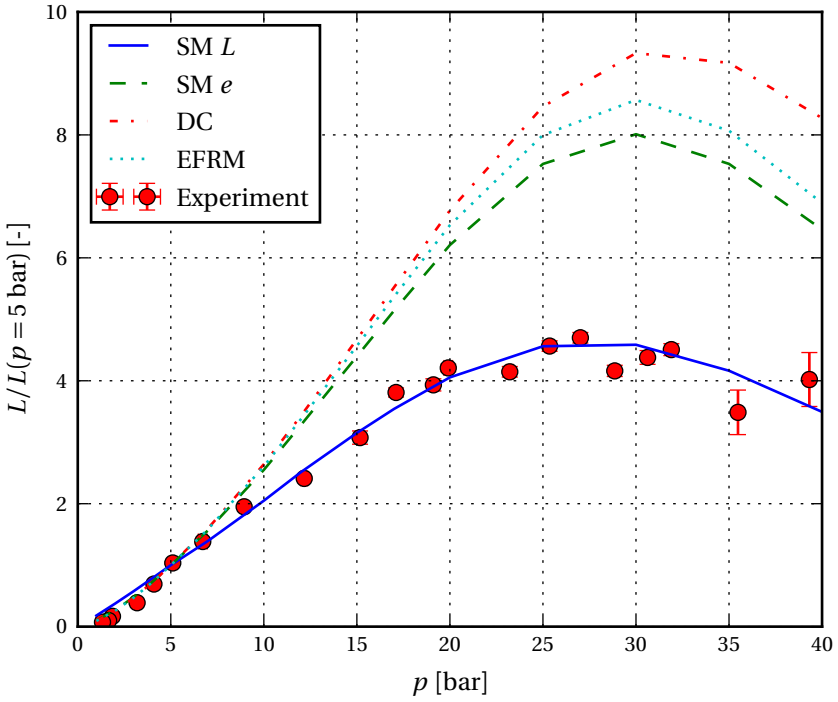


**Figure 4.12.:** Total OH* radiance filtered by the 308.5 nm filter. Comparison with the data from the numerical simulation: Radiance $L$ from Spectral Modeling (including self-absorption, "SM $L$"), emittance $e$ from Spectral Modeling (excluding self-absorption, "SM $e$"), result from the Detailed Chemistry model ("DC"), result from the Equilibrium Filtered Radiation Model ("EFRM").

Figure 4.12 shows an approximately linear increase of the overall OH* radiation up to 17 bar. At this point, the growth stagnates, and the overall radiance remains at a constant level up to 30 bar. The two (unstable) data points at 35 bar and 40 bar suggest a decrease of radiation.

Analogously to the experimental radiances, the overall radiances from the simulation results presented in the previous sub-section are collapsed into single values for each pressure. Their data is added to Figure 4.12. Again, each model is normalized by its value at 5 bar to produce comparable results. This naturally results in perfect agreement at 5 bar, but the responses of the three models to pressure are captured.

All radiation models yield very good results up to 10 bar. Above this value, the radiance $L$ resulting from the Spectral Modeling approach shows almost perfect agreement with the experimental data. The other three models, however, overshoot significantly. This deviation is clearly again due to the fact that these models neglect self-absorption.

### 4.4.4. Discussion of OH* Emission and its Modeling

The OH* radiation of the presented laminar jet flame experiment can well be modeled using the approaches presented in Section 4.1. Spectrally, the data available through the HITRAN database mostly matches the results measured. Regarding the band-pass filtered radiation of the flame under investigation, all three models perform very well below 10 bar. Above the optical thickness corresponding to this pressure, self-absorption becomes important, and the Detailed Chemistry and the Equilibrium Filtered Radiation Models overshoot both globally and locally.

As can be assumed from literature and from Section 4.2, OH* is in thermal equilibrium with OH. Therefore, the additional information of chemical excitation included in the Detailed Chemistry modeling does not result in better simulation data. The much simpler newly presented Equilibrium Filtered Radiation Model describes the flame radiation in this temperature regime equally well. Its ease of application makes it favorable for modeling the OH* radiation at high temperatures and moderate self-absorption.

At elevated optical densities, these simple models fail due to the wavelength-dependent self-absorption. To accurately simulate the OH* radiation in this regime, the Spectral Modeling approach has to be followed.

With the simulation representing the experiment well, the experimental observations of the flame shape and the pressure dependency can be explained: Conferring to Equation (4.3), the OH* radiation originates from the zones in which the presence of ground-state OH coincides with a high temperature. In a laminar jet diffusion flame, this is the region close to the stoichiometric surface. For varying pressures, the radiation profile follows the shape of this surface. The decrease in Froude number with pressure, which leads to the shortening of the flame, is thus visible in the radiation.

The total amount of OH* radiance observed is influenced by three parameters: The peak temperature, the general amount of OH molecules, and their distribution in space. In the presented experiment, the peak temperature is close to the adiabatic flame temperature and increases from approximately 3190 K to 3500 K between 1 bar and 10 bar (see also Figures C.1 et seqq.). At higher pressures, the flame is strained and the peak temperature effectively stagnates at a constant value of

approximately 3570 K. Above 10 bar, the increase in temperature does not have a significant influence on the OH* radiation (see Figure C.1 et seqq.).

More important is the amount of OH molecules and their distribution: At almost constant temperature, the radiation is directly proportional to the summed-up ground state OH concentration. This is effectively the flame thickness multiplied by the number density of OH, which is directly proportional to the pressure. In the experiment, the flame shape decreases only slightly up to 17 bar. In this range, the decrease appears to compensate the increase due to the rise in temperature, and the dominant influence is the pressure. This explains the approximately linear behavior of the summed-up radiation at low pressures.

At higher pressures, the reduction in flame thickness caused by the gravitational strain and the combined stagnation of peak temperature become more important than the OH number density increase with pressure. This leads to the stagnation of the overall radiation in this regime. Additionally, the broad spatial distribution of OH causes severe self-absorption: A large amount of radiation produced at the rear end of the flame does not reach the detector due to attenuation within the flame. This further reduces the amount of radiation received and leads to the experienced reduction at very high pressures.

From this perspective, the inconsistent observations on the dependency of the OH* radiation on pressure reported in the literature mentioned in Section 2.4.3 can be explained: There is no simple correlation between OH* radiation and pressure, but the radiation is greatly influenced by the flame area and number density, and additionally suffers from self-absorption. For the pressure variations presented in the literature, no comments were made on the dependency of flame volume on pressure. Typically, with a change in operating conditions, all of the parameters which influence the amount of OH intermediately present, like strain distribution, flame length, et cetera, are considerably altered. Depending on the setup, the overall OH* radiation can increase exponentially by an arbitrary factor, remain constant, or even decrease.

# 5. Blue Radiation

As introduced in Section 2.5, the blue or continuous radiation is a sparsely discussed feature of hydrogen flames. Even though it has been known for a long time [40] and certainly everyone is familiar of its presence from e.g. the radiation of the Space Shuttle Main Engine or the Vulcain engine, many researchers know little about its existence [123].

The blue radiation is a prominent feature of the jet flame experiment introduced in Section 3. In the following chapter, both its absorption and its spectral and spatial emission are discussed. The origin of the blue radiation is still not fully proven. For this reason, the last section in this chapter will give an evaluation of the suspected sources mechanisms.

## 5.1. Absorption

Up to this point, no research is known which studies the (self-)absorption of the blue radiation. As it is important for the interpretation of the radiance, it is again discussed first.

The investigation of the absorption is essentially analogous to the procedure described in Section 4.3.2. The experimental setup explained in Section 3.3.3 consisting of the background illumination, experiment, and camera is employed. Instead of the OH* filter, the band-pass filter centered around 456.270 nm with a FWHM of 2.370 nm (see Appendix B) is mounted in front of the camera lens to ensure that only blue radiation is recorded.

The spatial transmittance is measured at six pressure levels up to 40 bar. At each operating condition, 2048 frames with a sampling frequency of 50 Hz are recorded. Around 456.270 nm, the radiation of the 500 W Hg(Xe) lamp is orders of magnitude larger than at 308.5 nm which allows shorter gating times of the image intensifier and, therefore, the higher frame rate. Additionally, the background radiance is considerably stronger compared to the flame radiation in this wavelength band. The camera and image intensifier can, therefore, be set to record the background intensity distributed over the entire sensitivity range. This provides a much better signal-to-noise ratio compared to the experiments described in Section 4.3.2.

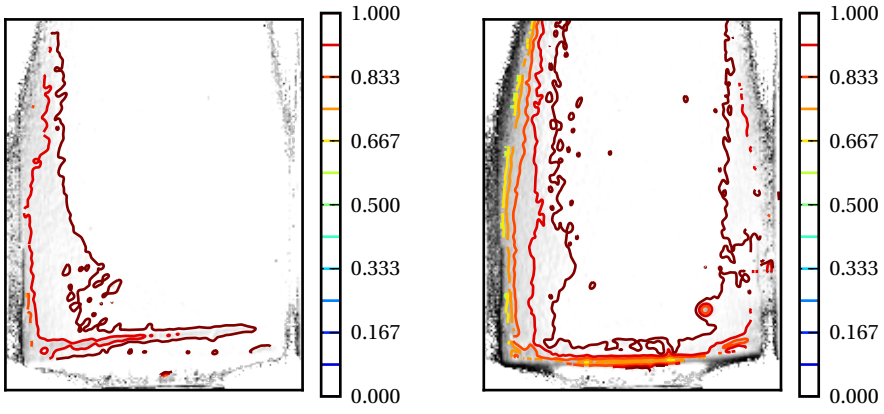


**(a)** 1 bar




**(b)** 9.78 bar

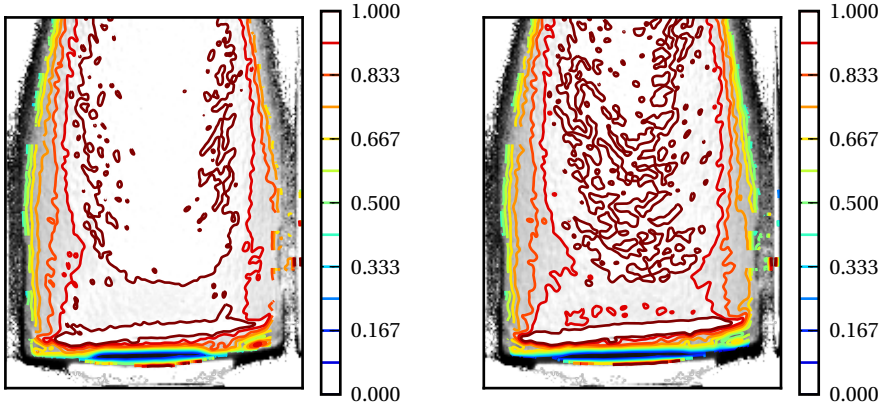


**(c)** Experiment 21.11 bar




**(d)** 30.05 bar

**Figure 5.1.:** Blue transmittance of the Hg(Xe) lamp radiation through the flame, filtered by the 456.270 nm band-pass filter (see Figure B.2).

The results of the spatial transmittance measurements are shown in Figure 5.1 at approximately 1, 10, 20, and 30 bar. In contrast to the transmittance in the OH band, where severe absorption was observed, no significant deviation from unity can be seen for the blue radiation. This is the case for all pressure levels studied. Only the influence of beam steering causes shadows along the edges and the impurity of the diffuser.

From these measurements, it can be concluded that no significant absorption is present in hydrogen-oxygen flames around 456.270 nm up to 30 bar pressure. As the emission spectrum is continuous, it can be assumed that a corresponding absorption spectrum would also be continuous, and that the absorption coefficient is only weakly depending on the wavelength. Therefore, the absorption of the broad-band background at the band-pass filtered wavelength should be similar

to the absorption of the flame's own radiation. As no absorption is observed, self-absorption of the entire blue radiation is concluded to be insignificant.

## 5.2. Emission

The absence of self-absorption in the entire pressure range makes the blue radiance much easier to interpret than the OH* radiance. The flame is optically thin with respect to the blue radiation, and radial profiles can be extracted from line-of-sight integrated measurements via the modified inverse Abel transform (see Section 3.5).

The following section presents the spectrum of the experimental flame and the spatial distribution of the radiation. Subsequently, the influence of pressure on the overall blue radiation is shown.

### 5.2.1. Blue Radiance Spectrum

The coarse spectrum of the flame at various pressures is shown in Figure 5.2. It is recorded by the setup described in Section 3.3.2 using the 150 grooves/mm grating. The $\Delta v = 1$ band around 285 nm, the $\Delta v = 0$ band around 310 nm, and the $\Delta v = -1$ band around 340 nm of the OH radical are dominating the UV range. The continuous blue radiation is much weaker, but clearly visible for higher pressure levels. It is partially masked by the high wavelength region of the OH bands around 340 nm and extends beyond the end of the spectrum displayed in Figure 5.2. The flat maximum lies at approximately 440 nm. The radiation intensity increases with pressure for both OH* and blue emission. For OH*, the pressure influence appears to be less significant at elevated levels, which is in agreement with the results shown in Fig. 4.12. For the blue radiation, the pressure influence is considerably stronger. While significant at 31 bar, it is not detectable compared to the OH* radiation below 5 bar. A human eye is able to see it very brightly already at atmospheric pressure.

The continuous radiation shows a reproducible fine-structure as reported by Schefer et al. [123]. The peak appears to become sharper with rising pressure and temperature. Apart from the OH bands, no superimposed radiation is observed. Therefore, it can be concluded that the band-pass filtered signal recorded around 456.270 nm is attributed purely to the blue continuous radiation. The subsequently presented results rely on this assumption.

### 5.2.2. Spatial Blue Radiance

Spatially, the line-of-sight integrated blue radiation shows a shape very similar to the OH* radiation. A comparison between the two radiances at 20 bar is given in

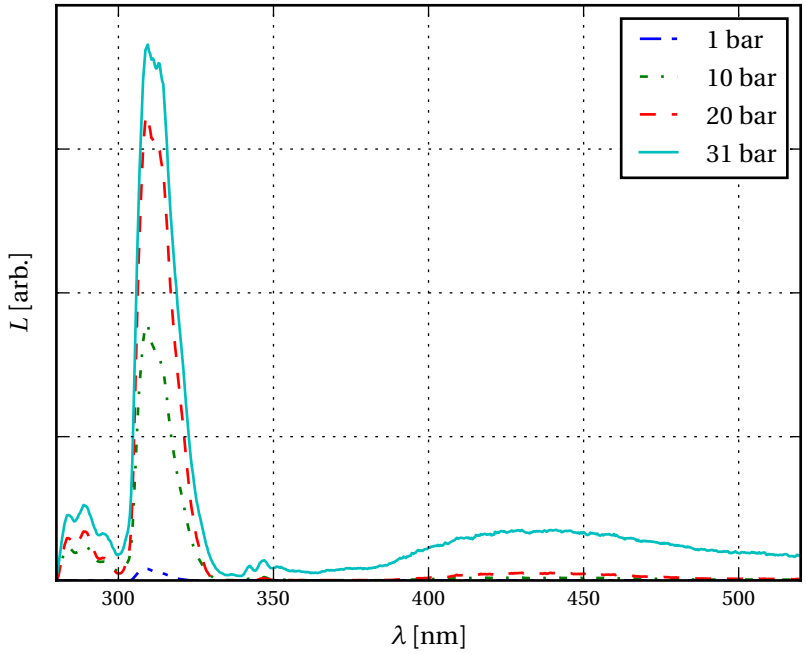


**Figure 5.2.:** Coarse spectrum of the flame 5 mm above the fuel lance at different pressures.

Figure 5.3(a). Additionally, the radial profiles obtained from applying the modified inverse Abel transform neglecting absorption described in Section 5.3 is shown in Figure 5.3(b).

Generally, the blue radiation shows a very similar shape to the OH* radiation at all pressures. The peaks are approximately at the same axial position. However, the blue radiation has a sharper edge than the more diffuse OH* radiation. The influence of self-absorption of OH* is clearly visible: In the line-of-sight integrated data, the intensity close to the center at the foot of the flame is low for the blue radiation, whereas it is relatively more pronounced for the OH* radiation due to the attenuation of OH* radiation at the maximum value. Similarly, the modified inverse Abel transform of the blue radiation produces a reasonable radial field, which is not the case for the OH* radiation due to self-absorption.

With increasing pressure, the shape of the blue radiation follows a trend similar to the one of the OH* radiation. An overview is shown in Figure 5.5, with more data available in Appendix C.

### 5.2.3. Overall Blue Radiance

To quantify the influence of pressure on the blue radiation, the overall radiance of the entire flame is plotted as a function of pressure in Figure 5.4. The quantities are

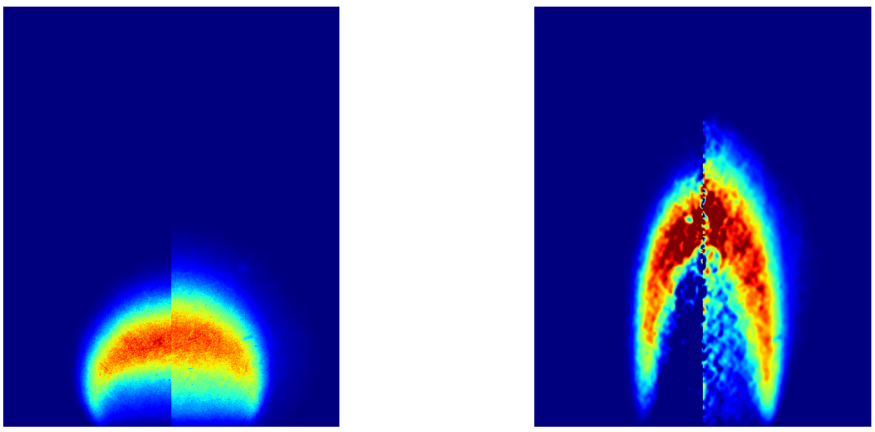

**(a)** Line-of-sight integrated radiation, 20 bar

**(b)** Results of the inverse Abel transforms, 1 bar

**Figure 5.3.:** Comparison between blue (left halves) and OH* (right halves) radiation of the jet flame.

obtained by computing the mean value of the 204 pictures taken at each pressure. The standard deviation of this value is illustrated by error bars in Figure 5.4 and is only significant above 33 bar, indicating the flame flicker like described in Section 4.4.3. As an absolute measurement of the radiance was not feasible, the values are normalized by the radiance at 5 bar.

At atmospheric pressure, the blue radiation only amounts to 2% of the radiance at 5 bar. Up to approximately 10 bar, the overall blue radiation increases exponentially with pressure. The rate of change slows down gradually between 10 bar and 25 bar, in which the increase is approximately linear. Between 25 bar and 33 bar, the blue radiation stagnates at a level 17 times larger than the radiance at 5 bar. Above 33 bar, the radiance increases again, although caution is necessary as the flame is unstable at these operating conditions. Between 1 bar and 40 bar, the overall blue radiation increases by a factor larger than 1000. This value is in perfect agreement with the number stated by Diederichsen and Wolfhard [27].

## 5.3. Investigation of the Origin of the Blue Radiation

The real source of the blue radiation is still not identified beyond doubt. As summarized in Section 2.5, the mechanisms suggested in literature are the formation

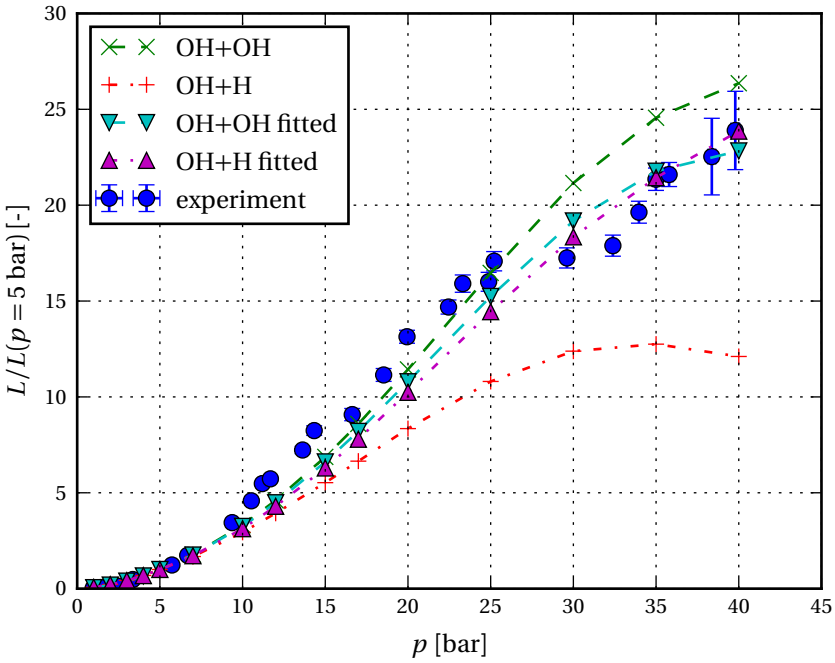


**Figure 5.4.:** Comparison of the measured total flame radiation at 456.270 nm to the numerical $H_2O_2^*$ and $H_2O^*$ chemiluminescence models (reactions (5.1) and (5.2)). The parameters $n$, $E_a$, and $k_Q$ are set to 0 for the standard case. The *fitted* curves are plotted for the parameters optimized to fit the experimental data (see Table 5.1). All curves are normalized by their intensities at 5 bar.

of chemiluminescent $H_2O^*$ and chemiluminescent $H_2O_2^*$:

$$OH + H \longrightarrow H_2O^* \longrightarrow H_2O + h\nu \tag{5.1}$$

$$OH + OH \longrightarrow H_2O_2^* \longrightarrow H_2O_2 + h\nu \tag{5.2}$$

The first reaction (5.1) is favored by Padley [103], whereas the second reaction (5.2) is found more suitable by Vanpee and Mainiero [137]. However, both studies suffer from the fact that they do not spatially resolve their flames and are, therefore, not able to compare molecular data to the recorded radiation data directly.

The present study provides a spatially resolved numerical simulation accompanying the experimental data. This combination can be used to gain further insight into the origin of the blue radiation by evaluating the two above models.

Before the experimental data is compared to the simulation, two conclusions that can be drawn from the absorption and spectral measurements should be mentioned: As presented in Section 5.2.1 and the work by Schefer et al. [123], the continuous spectrum exhibits a detailed fine-structure. From the discussion of various flame spectra made in Section 2.2.4, such a spectrum can be typically attributed

to the radiation of molecules consisting of three or more atoms, which allow the great number of transitions required. Both suggested models appear to be suitable from this perspective. The absence of any observed absorption in the wavelength band attributed to the blue radiation can have two sources: Either, the transition probability is very low, or the number density of the ground state species is very low.

The low absorption allows to assume direct proportionality between radiation and concentration of the excited species. Following the derivation in Section 2.3.2, the concentration of the chemically excited species can be calculated from Equation (2.20). Applied to the two chemiluminescence models proposed, the equations become:

$$[H_2O^*] = \frac{k_{\mathrm{ch},\,H_2O^*}\,[OH]\,[H]}{k_{\mathrm{Q},\,H_2O^*}\,[Q] + A_{H_2O^*\rightarrow H_2O}} \tag{5.3}$$

for reaction (5.1) forming $H_2O^*$ and

$$[H_2O_2{}^*] = \frac{k_{\mathrm{ch},\,H_2O_2{}^*}\,[OH]\,[OH]}{k_{\mathrm{Q},\,H_2O_2{}^*}\,[Q] + A_{H_2O_2{}^*\rightarrow H_2O_2}} \tag{5.4}$$

for reaction (5.2) forming $H_2O_2{}^*$.

Equations (5.3) and (5.4) show several unknown parameters: Most important are the rate constant of the chemical excitation reaction, $k_{\mathrm{ch},\,H_2O^*}$ and $k_{\mathrm{ch},\,H_2O_2{}^*}$. Typically, these parameters follow a modified Arrhenius equation:

$$k_{\mathrm{ch},\,H_2O^*} = A_{H_2O^*}\;T^{\,n_{H_2O^*}}\;\exp\left(-\frac{E_{a,H_2O^*}}{R_m\;T}\right) \tag{5.5}$$

$$k_{\mathrm{ch},\,H_2O_2{}^*} = A_{H_2O_2{}^*}\;T^{\,n_{H_2O_2{}^*}}\;\exp\left(-\frac{E_{a,H_2O_2{}^*}}{R_m\;T}\right) \tag{5.6}$$

Additionally, quenching can influence the concentration of the excited species. Being known as an effective quencher for other chemiluminescence models [133] and being the by far most dominating product species present in the flame, $H_2O$ is assumed to be the only quenching species Q[1]. Following a Stern-Volmer approach, the quenching rate parameters $k_{\mathrm{Q},\,H_2O^*}$ and $k_{\mathrm{Q},\,H_2O_2{}^*}$ are treated as constants (see Section 2.3.2).

Theoretically, the Einstein coefficients $A_{H_2O^*\rightarrow H_2O}$ and $A_{H_2O_2{}^*\rightarrow H_2O_2}$ are also unknown parameters. However, as all comparisons are normalized, they become irrelevant. Similarly, the pre-exponential factors $A_{H_2O*}$ and $A_{H_2O_2{}^*}$ only lead to a constant amplification of the concentrations and can, therefore, not be studied.

[1] Additionally, the sum of all species concentrations (which is equal to the molar density) is tried as the quenching concentration. However, this results in approximately the same parameters and an almost identical output. This option is, therefore, not further discussed.

| | $H_2O^*$ | $H_2O_2{}^*$ |
|---|---|---|
| $n$ | 0.0031 | 0.0013 |
| $E_a$ | 8.7 J/kmol | −7.3 J/kmol |
| $k_Q$ | 0.0056 $m^3$/kmol | 0.0021 $m^3$/kmol |

**Table 5.1.:** Optimized parameters of the chemiluminescence models for total blue radiation as a function of pressure.

To evaluate the two chemiluminescence models, Equations (5.3) and (5.4) are applied on the computed numerical data set on a cell-by-cell basis. The resulting concentration fields $[H_2O^*]$ and $[H_2O_2{}^*]$ are compared with the experimental data.

The first comparison is made based on the total radiation of the flame. To compute this value numerically, the concentration at each cell is multiplied by the cell volume. The summation over all cells results in the total radiation, which can be computed for each pressure level. The data is normalized by the value at 5 bar and added to Figure 5.4.

In a first approach, all unknown Arrhenius and quenching parameters are assumed to be zero. The radiation density originating from each cell is, therefore, calculated by simply multiplying the concentration of OH and H for the $H_2O^*$ chemiluminescence and of OH by itself for the $H_2O_2{}^*$ chemiluminescence. In the succeeding step, the parameters $n$, $E_a$, and $k_Q$ of both chemiluminescence models are optimized to match the experimental data best using a Nelder-Mead algorithm available through Python/SciPy [68]. The parameters obtained are listed in Table 5.1.

Figure 5.4 shows clearly that even without taking into account the Arrhenius and quenching parameters, the measured total intensities are already well described by the chemiluminescent reaction forming $H_2O_2{}^*$. The chemiluminescent reaction forming $H_2O^*$ on the other hand significantly under-predicts the radiation for higher pressures without tuning.

The optimization of the Arrhenius and quenching parameters yields close correspondence between the simulation and the experiment for both models, even though all optimum parameters differ only slightly from zero. The small values of the optimum Arrhenius parameters suggest that the chemiluminescence reactions are not sensitive to temperature. However, this fact has to be considered with care, as the temperature within the luminous zone varies only between 3100 K and 3500 K.

Above 30 bar, the experimental values that do not follow the general trend are not reproduced by both models. This could be due to the fact that the flame becomes unstable in the experiment for very high pressures which leads to differences from the simulation result. Based on this data, no chemiluminescence model can be qualified as a better match to the experimental data.

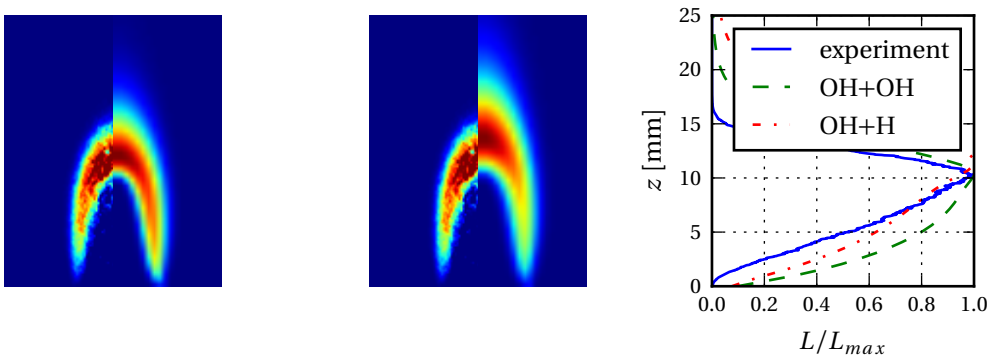


**(a)** Experiment: 1.0 bar, simulation: 1 bar

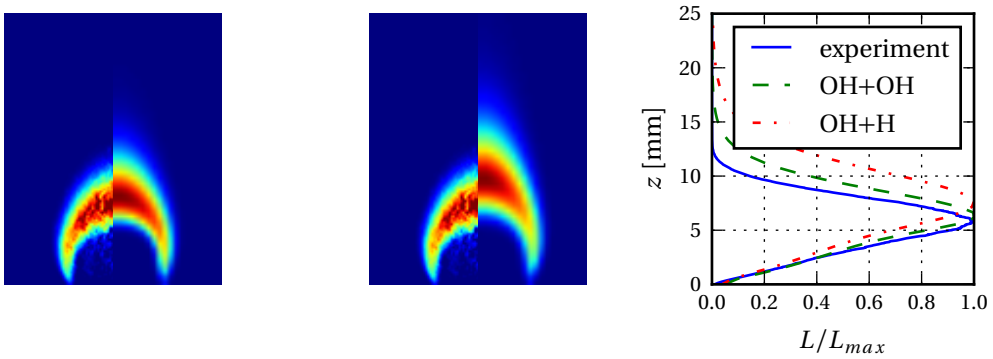


**(b)** Experiment: 10.5 bar, simulation: 10 bar

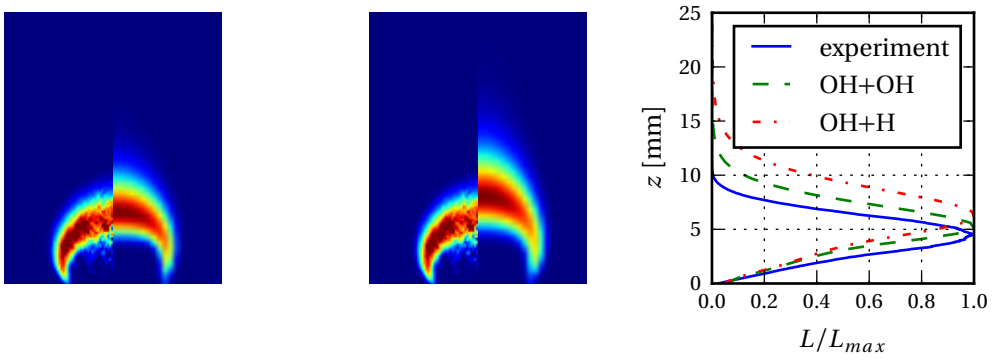


**(c)** Experiment: 19.9 bar, simulation: 20 bar

**Figure 5.5.:** Radial distributions of the blue radiation at different pressures. The left half of the images shows the inverse Abel transformed measured intensities. The right half of the images shows the result of the numerical computed reaction rates forming $H_2O_2$* (reaction (5.2), left) and $H_2O$* (reaction (5.1), center). The images on the right hand side compare the line-of-sight integrated radiances over the flame height.

Additionally, the experimental images from the side of the flame showing the line-of-sight integrated emission are considered. As described in Section 5.2.2, the radial profiles are obtained via the modified inverse Abel transform. This data can directly be compared to the $H_2O^*$ and $H_2O_2{}^*$ radiation models applied to the axis-symmetric simulation domain, as shown in Figure 5.5 for three selected pressures[2]. As the pressure in the experiment cannot be set directly but has to be measured, the experimental data closest to the simulation pressure levels is displayed. Figure 5.5 additionally shows the integrated emission over the height of the flame from the measurements and the models.

Within the luminous zone of the flame at a single specific pressure, both the temperature and the water vapor concentration do not vary significantly (see Figure C.1 et seqq.). Therefore, the impact of the Arrhenius and quenching parameters on the radial emission simulations is negligible.

Like for the overall blue radiance as a function of pressure, the chemiluminescent reaction model forming $H_2O_2{}^*$ describes the spatial radiation field very well for all pressure levels. The peak is constantly predicted slightly downstream of the experimental measurements. As pointed out in Section 4.4.2, this behavior is also visible in the comparison of the OH* radiation, which also mainly depends on the concentration field of OH.

On the other hand, the chemiluminescent reaction forming $H_2O^*$ constantly results in a luminous zone longer than observed in the experiment. The peak is further downstream, and the flame is computed to be thicker than measured. This is due to the fact that this reaction relies on the concentration of atomic hydrogen, which is higher on the hydrogen (outer) side of the flame.

From this comparison, it can be seen that reaction Equation (5.2) better predicts the experimentally observed blue radiation than reaction Equation (5.1). This supports the observations from Vanpee and Mainiero [137] and Diederichsen and Wolfhard [27]. The temperature exponent $n_{H_2O_2{}^*} = 0.0013$ and the Arrhenius activation energy $E_{a,H_2O_2{}^*} = -7.3$ J/kmol derived from the curve fitting have to be treated with care as the temperature range under investigation is small. The quenching rate of the relation has a negligible value. This can have two reasons: First, the excited state $H_2O_2{}^*$ is so unstable that it immediately relaxes to the ground state $H_2O_2$ after formation. Alternatively, the opposite assumption is also possible: The lifetime of $H_2O_2{}^*$ is so large that it is always de-excited by collision. In Equation (5.4), the Einstein coefficient $A_{H_2O_2{}^* \rightarrow H_2O_2}$ is then negligible. If the reaction forming $H_2O_2{}^*$ is not a bimolecular reaction but instead a trimolecular reaction $OH + OH + Q \longrightarrow H_2O_2{}^* + Q$, then the concentration of the collision partner [Q] appears as an additional factor in the numerator of Equation (5.4). If again $H_2O$ is assumed to be the main collision partner Q, then its concentrations appear in both numerator and denominator of

[2] Further data is presented in Figure C.9.

Equation (5.4) and, therefore, cancels out. The concentration of $H_2O_2$* and thus the blue radiation is again proportional to the square of the concentration of OH.

The little differences between the two radiation models, and the fact that only two previously assumed possibilities are investigated, are clearly not sufficient to prove beyond doubt that reaction Equation (5.2) is the real physical source of the blue radiation. In fact, the real origin of the blue radiation might not even be one of the two chemiluminescence reactions proposed. The close spatial correlation between OH* and blue radiation leads to the new idea that the blue radiation is a fluorescent response of some molecule excited by the strong OH* radiation.

However, from a practical point of view, the physical source might not be relevant: In the current study it is shown that the square of the OH concentration is proportional to the recorded radiation. If this relation is shown to be true for other flames, the method could present a very simple way to validate numerical simulations.

# 6. Flame Radiation and Heat Release

To investigate the mechanisms driving combustion instability in liquid rocket engines, the measurement of the volumetric heat release rate is beneficial. As all measurements are difficult in such a hostile environment, a correlation between flame radiation and the heat release rate would be desirable. In this chapter, the relation between these two quantities is examined for flames and conditions typical for rocket combustion.

Even for laboratory scale flames, it is hard to measure the volumetric heat release rate accurately. Therefore, this is not even attempted in this study. Instead, the heat release rate is investigated based on the numerical computations described in Sections 3.4 and 3.6.

In the previous chapters it was shown that the OH* radiation in flames at elevated temperature and pressure can be modeled accurately. Similarly, the blue radiation can be described by the chemiluminescence reaction (5.2). Therefore, by numerically simulating heat release rate and radiation of counterflow flames, further deductions can be derived without performing experiments.

To understand the physical link between heat release rate and flame radiation, and to make use of the data already discussed, the two properties are first compared within laminar flames. To extend this information to the turbulent combustion in practical rocket engines, the findings are discussed in terms of laminar flamelet ensembles forming a turbulent flame. Based on these results, the use of radiation measurements for the investigation of combustion instability in liquid rocket engines is evaluated.

## 6.1. Flame Radiation and Heat Release in Laminar Flames

The laminar flame structure is the most basic description of a non-premixed flame featuring all essential physical effects. Diffusion, chemical reactions, and flow phenomena are present. The laminar nature avoids the complexity of turbulence-flame-interaction and thus provides an environment which can accurately be modeled numerically. On this basis, the physical mechanisms leading to both heat release and radiation are elaborated and compared.

### 6.1.1. Laminar Jet Flame Experiment

To synthesize the results already discussed in the previous sections, the radiation and heat release of the jet flame are discussed first. Figure 6.1 repeats the radially deconvoluted experimental and numerical profile of the OH* radiation at 1 bar. In addition, the numerically computed heat release rate is shown. The contour plots can be compared directly.

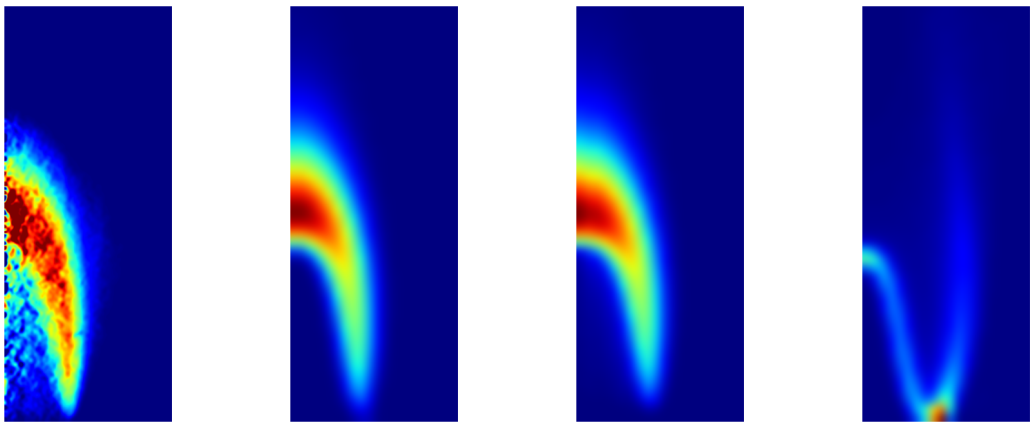

**(a)** Measured OH* radiance, inverse Abel transformed

**(b)** [OH*] from DC simulation

**(c)** [OH*] from SM simulation

**(d)** Volumetric heat release rate

**Figure 6.1.:** Comparison between the local (filtered) OH* emissivity of the jet flame with the local heat release rate at 1 bar.

It is seen that radiation and heat release rate have significantly different spatial distributions. The OH* radiation shows the familiar crescent shape, with little intensity at the flame base and mostly radiating at the tip of the flame. Figure 5.3 shows that the blue radiation follows a similar shape. The heat release rate, on the other hand, peaks directly at the anchoring point at the lance rim. Here, the heat of reaction is mostly transferred to the lance. From there on, two regions of heat release emerge: One at the inner (oxygen) side, and one at the outer (hydrogen) side. On a volumetric basis, the oxygen branch appears to be more intense. However, the hydrogen branch shows a larger radius and in total accounts for approximately the same amount. In between the two branches, the heat release drops almost to zero. This shape is very reasonable, as will be discussed in the next section. It is also in agreement with observations from other diffusion jet flames in literature [53, 130].

Spatially, there obviously is not even a qualitative correlation between the local volumetric heat release rate and either the local OH* or blue radiation for the laminar jet flame.

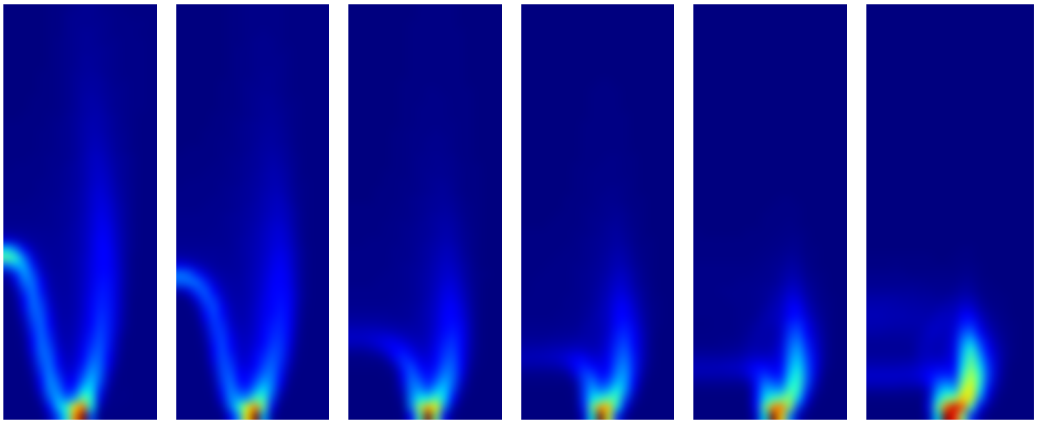

**(a)** 1 bar **(b)** 5 bar **(c)** 12 bar **(d)** 20 bar **(e)** 30 bar **(f)** 40 bar

**Figure 6.2.:** Local heat release rate of the laminar jet flame at various pressures.

With increasing pressure, the volumetric heat release rate adjusts its shape to the lower velocities at constant buoyancy forces (see Figure 6.2). At all operating conditions, the two heat release branches exist and enclose the luminous zone. As the flame becomes smaller in shape, the fraction of heat release taking place close to the flame foot is increased. Nevertheless, the overall heat release rate remains constant at approximately 600 W because of the constant mass flow rates.

From Figures 4.12 and 5.4 it is known that both the overall OH* radiation and the overall blue radiation increase significantly with pressure by a factor of 80 and more than 1000, respectively, while the mass flow rate is constant. An assumed direct proportionality between the total OH* or blue radiation and the total heat release rate, therefore, would not hold for varying pressure.

### 6.1.2. Counterflow Flames

A better understanding of the spatial distributions of heat release and radiation observed above can be gained from counterflow flame simulations. Their one-dimensional nature allows for more detailed and quantitative analysis of the processes happening within a non-premixed flame. This section relies on the results obtained from the Cantera simulations described in Section 3.6.

Figure 6.3 shows the key structural aspects of a typical hydrogen-oxygen diffusion flame. As pure hydrogen is used for the fuel and pure oxygen for the oxidizer, their mole fractions $X_{H_2}$ and $X_{O_2}$ are unity at their corresponding boundaries. Within the flame, their mole fractions overlap due to diffusion. The products of combustion, mostly $H_2O$ and OH, are present in the center of the flame.

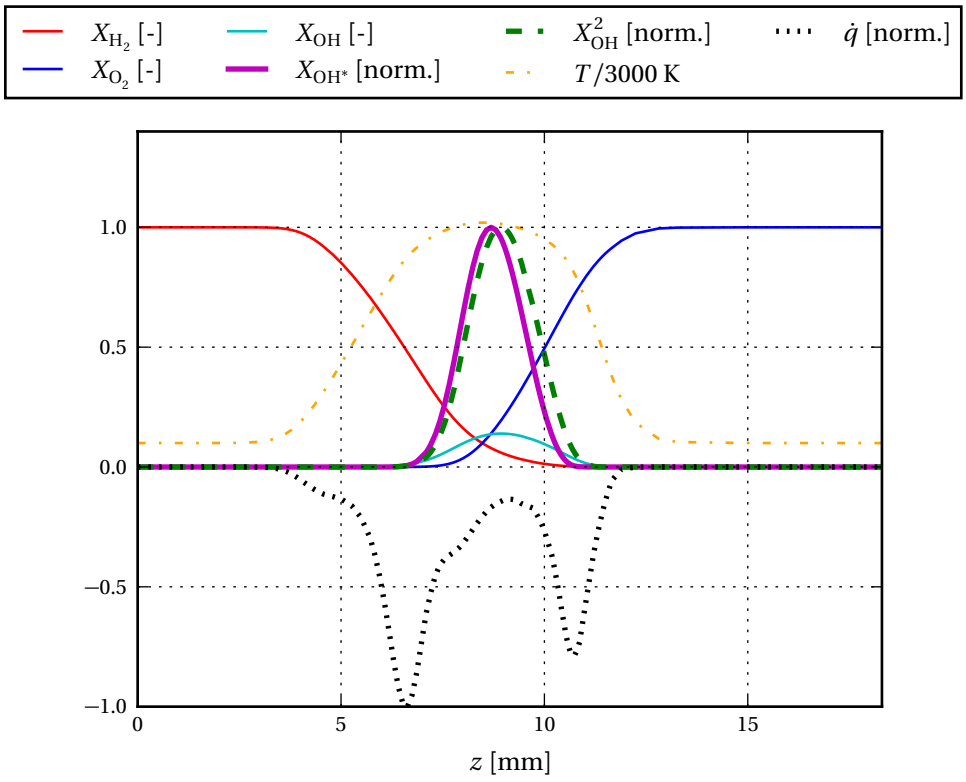


**Figure 6.3.:** Structure of a counterflow flame at $p = 1\,\text{bar}$ and $a_{\text{max}} = 5.8 \times 10^2\,1/\text{s}$.

The heat release rate resulting from the chemical reactions is also shown in Figure 6.3. It is computed from Equation (3.12) and exhibits a complex structure with two dominating peaks. To understand the origin of this structure, it is split into the most important reactions in Figure 6.4, similar to the analysis presented by Law [83]. The peak on the hydrogen side is mostly due to the reaction $H + OH + M \longrightarrow H_2O + Q$, whereas the peak on the oxygen side is caused by the combination of the same reaction, the reaction $H + O_2(+Q) \longrightarrow HO_2(+Q)$, and the reaction $HO_2 + OH \longrightarrow H_2O + O_2$. These reactions reasonably dominate the heat release rate, because they are the chain terminating reactions (indirectly) forming water vapor. In between the two peaks, there is less formation of $H_2O$. Instead, the endothermic reaction $H + O_2 \longrightarrow O + OH$ forming OH actually removes heat from the flow.

The double-peak structure can also be explained in an intuitive way: The effect of heat release is the increase in temperature. In non-premixed flames, the two streams of oxidizer and fuel are each heated up before they reach the stagnation plane. It is natural that heat release coincides with the gradients in temperature. The endothermic reactions sustaining the flame are most effective in the regions of the highest temperature, thus reducing the amount of heat release in this zone.

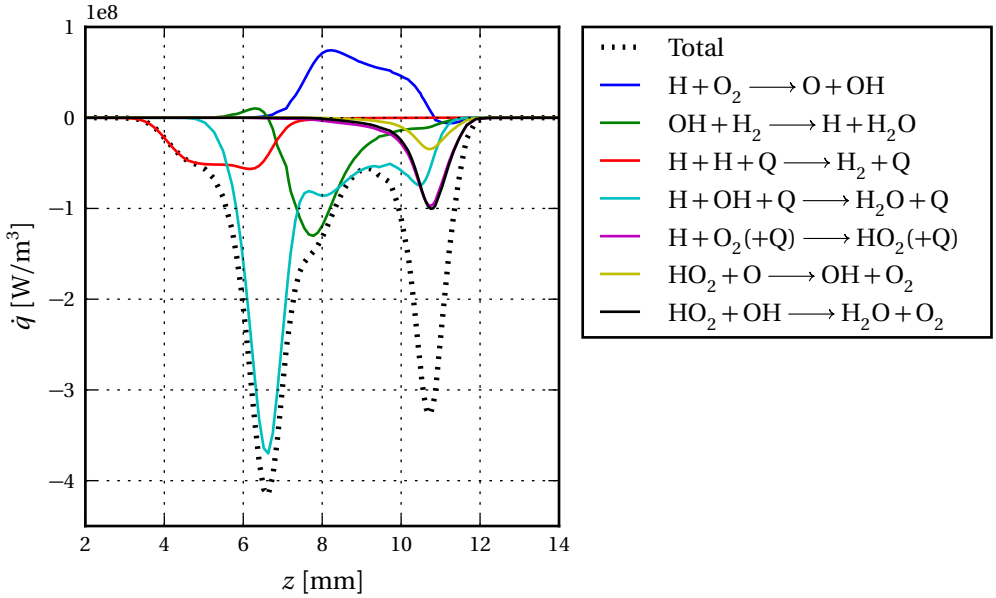


**Figure 6.4.:** Contribution of the most important reactions to the total heat release within a counterflow flame. Data at $p = 1$ bar and $a_{\max} = 5.8 \times 10^2$ 1/s.

This behavior is visible so well because of the high diffusivity of atomic and molecular hydrogen and the absence of dilution like nitrogen. It is insensitive to pressure, but influenced by strain (see Figure 6.5): With increasing strain rate, the flame thickness is reduced and the diffusion velocities cannot keep up with the free stream velocities. The two zones of heat release move closer together and partially overlap.

The spatial emissivities of the OH* and blue radiation are also shown in Figure 6.3. Their normalized (filtered) emissivities are modeled by the Detailed Chemistry approach for OH* and the square of the OH concentration for the blue radiation[1]. Both profiles show a single, sharp peak in the center of the flame at approximately equal locations.

The emissivity profile of OH* can be best explained by Equation (4.3): If thermal excitation is assumed, then the OH* concentration is directly proportional to the concentration of OH and exponentially depending on temperature. As shown in Figure 6.4, OH is formed from an endothermic reaction which is most prominent in the hottest region of the flame. Its profile is centered around this zone. The exponential temperature influence leads to an even narrower peak of OH* compared to OH, with a maximum at the highest temperature.

Similarly, taking the square of the OH concentration to model the blue radiation results in a profile which is based on the shape of the ground state OH distribution,

[1] The EFRM or filtered SM OH* emissivities yield an identical normalized profile compared with the DC result.

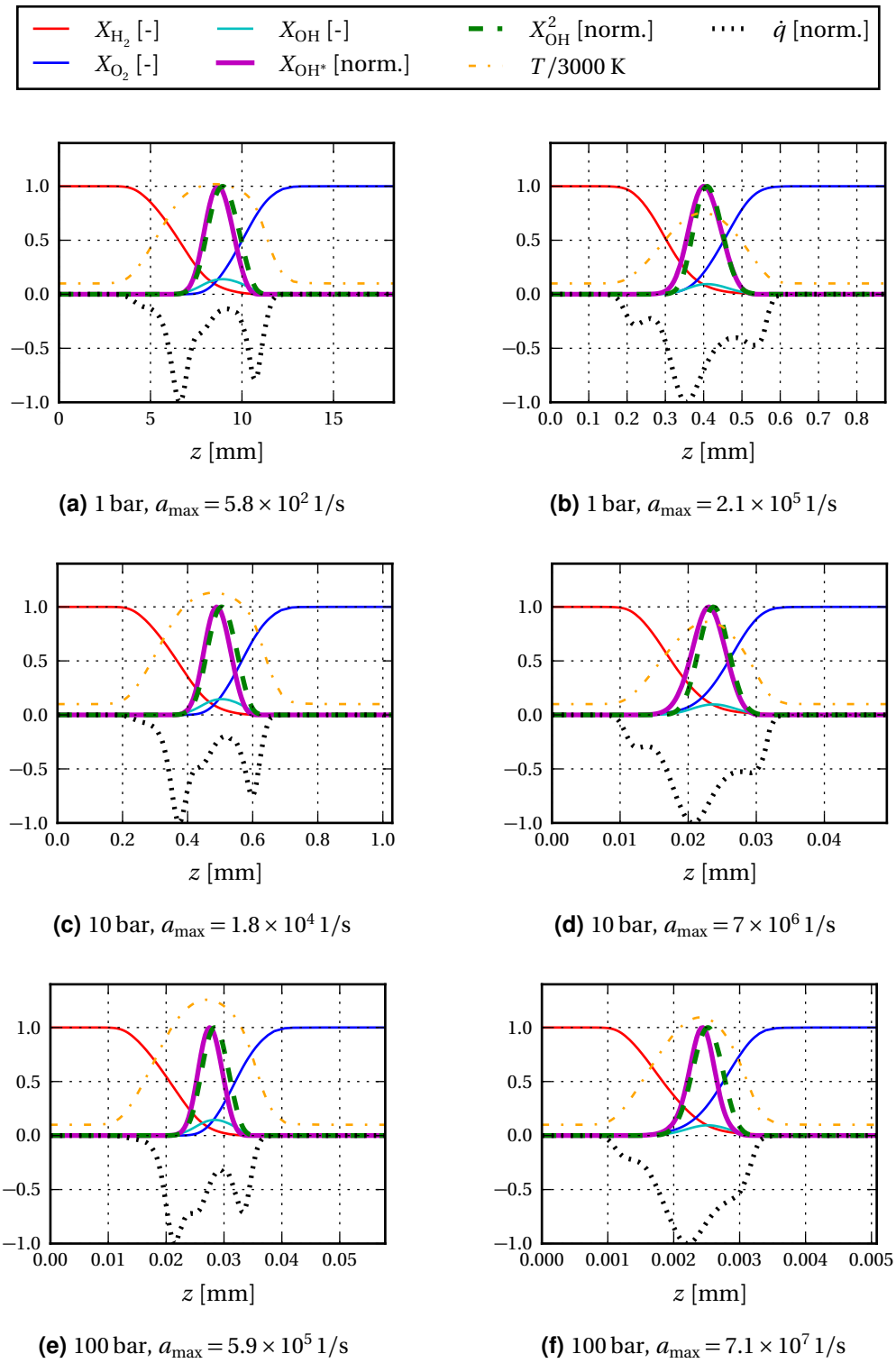


**(a)** 1 bar, $a_{max} = 5.8 \times 10^2$ 1/s

**(b)** 1 bar, $a_{max} = 2.1 \times 10^5$ 1/s

**(c)** 10 bar, $a_{max} = 1.8 \times 10^4$ 1/s

**(d)** 10 bar, $a_{max} = 7 \times 10^6$ 1/s

**(e)** 100 bar, $a_{max} = 5.9 \times 10^5$ 1/s

**(f)** 100 bar, $a_{max} = 7.1 \times 10^7$ 1/s

**Figure 6.5.:** Profiles within counterflow flames at various pressures and maximum strain rates.

but sharper. This is in agreement with the experimental observations presented in Section 5.2.2.

Comparing the profiles of OH* and blue radiation to the heat release rate profile, the same discrepancy is observed as in the semi-experimental results in the previous section. It can be concluded that within non-premixed hydrogen-oxygen flames, heat release rate and radiation peak at spatially separate locations. As explained above, the reasons for the profiles can be physically derived. A spatial correlation between heat release rate and OH* or blue radiation does not exist.

## 6.2. Flame Radiation and Heat Release in Turbulent Flames

As shown in the previous section, the flame radiation is not a good marker for the heat release within laminar non-premixed flames. However, almost all problems with combustion instability arise in turbulent flames. Practically, a correlation between the line-of-sight integrated radiation and the corresponding heat release rate is of greater interest than a spatial correlation within the laminar structure.

This section attempts to transfer the findings from the investigation of laminar flames onto turbulent flames. The approach is reasonable, as the turbulent flame is often imagined as an ensemble of laminar counterflow flames, then referred to as *flamelets* [107]. Therefore, the underlying physical processes leading to radiation and heat release learned from laminar flames still apply. However, if a turbulent flame is considered, the relation between heat release rate and radiation has to be evaluated for stochastic distributions of flamelet ensembles. The effects of turbulence are modeled by the straining of the individual flamelets forming the flamelet ensembles.

In practical turbulent flames in rocket engines, the pressure is high and flamelets experience high strain. The thickness of flamelets scales inversely with the square root of pressure and strain [34, 83, 114, 109]:

$$\delta \sim \frac{1}{\sqrt{p\ a}} \tag{6.1}$$

Effectively, the thicknesses of the flamelets are, therefore, well below 1 mm. Typical measurement equipment for large-scale rocket engines provides a resolution of this order. The detailed structure of the underlying flamelets cannot be resolved.

Additionally, radiation measurements are typically line-of-sight integrated measurements. Therefore, the exact spatial flame structure is not of interest. Instead, the radiation measured along the ray entering the detector is compared to the heat

**Figure 6.6.:** Illustration of the assumed flamelet ensemble.

release rate of the measurement volume (see Figure 6.6). From this integral point of view, three general cases are possible from basic consideration:

1. The measurement volume contains only unburnt reactants: In this case, there is no OH present and neither OH* nor blue radiation can take place. Similarly, as no reaction can take place, the heat release rate is zero.
2. Several flamelets are within the measurement volume: Both luminous and heat release zones are contained and their integral absolute values are positive.
3. The measurement volume consists of fully burnt products: The reaction is completed and no heat release takes place. However, radiation can still occur, if OH is present and the temperature is high enough (see also Burrows and Razner [19]). Nevertheless, if the equivalence ratio is not stoichiometric, the mixing of the combustion products with the species in excess results in lower temperature and substantially less OH compared to the flame zone. Therefore, the emissivity of OH* and blue radiation would be significantly lower compared to case 2.

Qualitatively, both OH* and blue radiation are markers for the line-of-sight integrated heat release rate, if the combustor is operated at globally non-stoichiometric conditions.

The question remains whether a quantitative relation exists. The experience from premixed hydrocarbon flames indicates that there might exist a correlation: As reviewed in Section 2.6, turbulent ensembles of flamelets can have equal property distributions, such that the integral flame radiation is proportional to the integral heat release rate. Additionally, Lauer et al. [82] introduced an approach for premixed flames, which provides a correction parameter to account for unequal strain rate distributions. To investigate non-premixed flames, the application of this technique is analyzed in the following.

Nevertheless, one limitation of the quantitative relation is evident: If self-absorption is significant, this affects only the line-of-sight integrated radiation. A direct proportionality between absolute radiation and absolute heat release rate is thus impossible. This constraint will be further discussed in Section 6.3. Within this section, self-absorption is ignored to derive quantitative results.

### 6.2.1. Flamelet-Integrated Correlation of Single Flamelets

If the line of sight is broken down into separate flamelets, and each flamelet is assumed to be cut normal to the flame surface, then the quantities of interest are the flamelet-integrated values. They are obtained by an integration along the axial flame coordinate $z$:

$$N_f = \int_{-\infty}^{\infty} N(z)\, dz \tag{6.2}$$

In the following, this operation is denoted by the subscript $_f$. This operation is applicable to any volumetric quantity $N$. For a single flamelet, the flamelet-integrated value $N_f$ thus represents a quantity with respect to the flame surface area.

For combustion of constant reactant composition at constant initial temperatures, the only two parameters influencing the structure of flamelets are pressure $p$ and strain rate $a$. To investigate both influences, batches of counterflow flame simulations at varying pressures and strain rates are computed following the procedure described in Section 3.6. The flamelet-integrated heat release rate $\dot{q}_f$, the flamelet-integrated OH* emissivity $[\mathrm{OH}^*]_f$, and the flamelet-integrated blue emissivity $[\mathrm{OH}]_f^2$ are plotted as a function of pressure and strain rate in Figure 6.7.

These quantities are already appropriately scaled. It is found out empirically that the flamelet-integrated quantities scale as follows:

$$\dot{q}_f \sim a^{1/2}\, p^{1/2} \tag{6.3}$$

$$[\mathrm{OH}^*]_f \sim a^{-1/2}\, p^{1} \tag{6.4}$$

$$[\mathrm{OH}]_f^2 \sim a^{-1/2}\, p^{3/2} \tag{6.5}$$

The relations especially hold for flamelets far from extinction. With increasing pressure, the extinction strain rate greatly increases, and the relations are valid for a larger strain rate range.

Pressure and strain rate thus have a signifiant impact on the flamelet-integrated heat release rate and both types of radiation. More importantly, the impact is not identical: While the flamelet-integrated heat release rate increases with the square root of strain rate, both flamelet-integrated types of radiation decrease with the square root of strain rate. This contradicts the hypothesis of direct proportionality between flamelet-integrated heat release rate and radiation: If two arbitrary flamelets with not-equal strain rates are considered, the flamelet with the higher strain rate will have a higher heat release rate but a lower radiation compared to the flamelet with the lower strain rate. A general direct proportionality between heat release rate and radiation of single flamelets is, therefore, not possible. This holds already at constant pressure. If the flamelets to be compared show unequal pressure

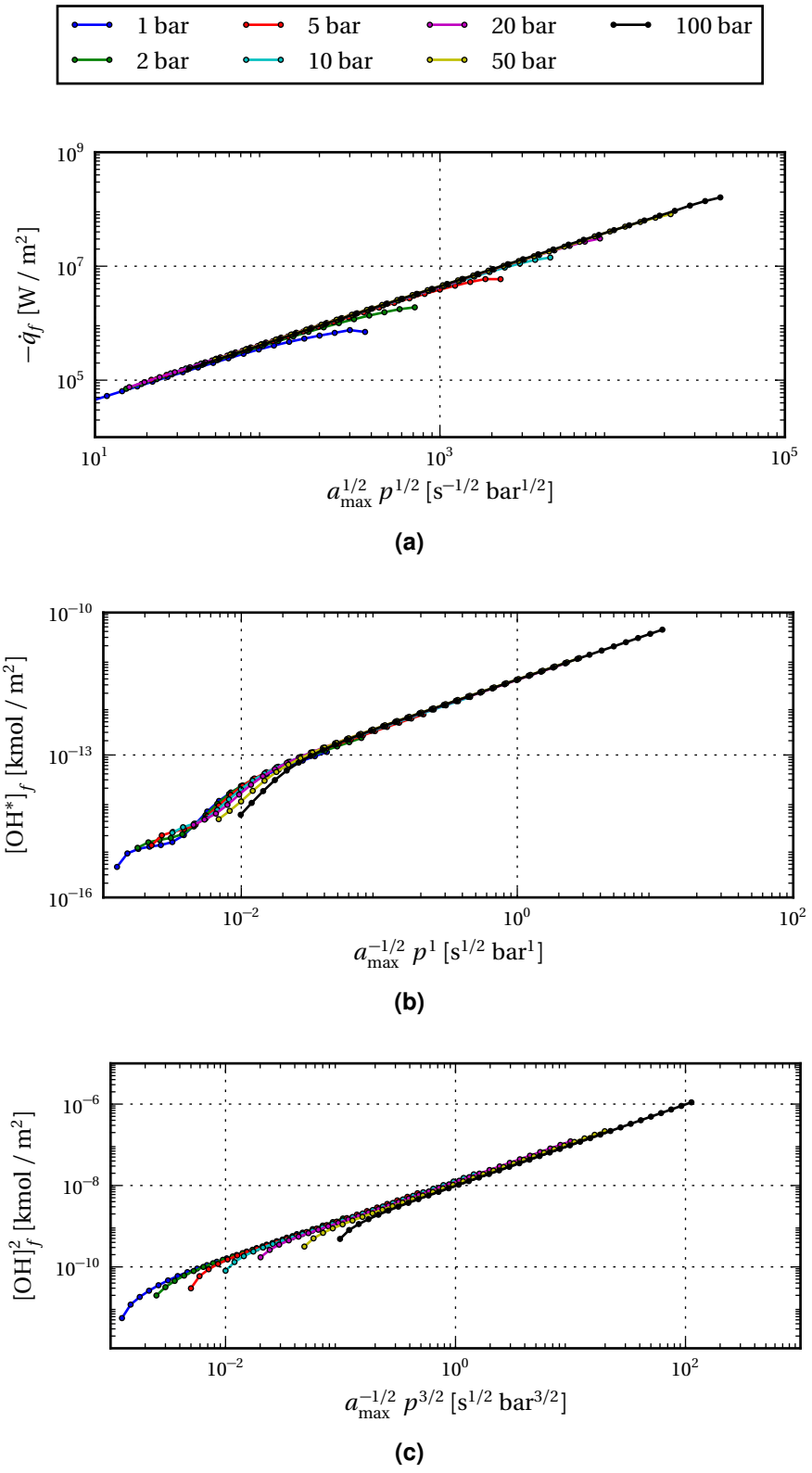


**Figure 6.7.:** Flamelet-integrated heat release rate (a), OH* radiation (b), and blue radiation (represented by $[OH]^2$) (c) as a function of maximum strain rate $a_{\mathrm{max}}$ and pressure $p$.

levels, the discrepancy for the relation between heat release rate and radiation is even larger following the above equations.

#### Justification of Equations (6.3) through (6.5)

Equation (6.3) through Equation (6.5) show a very simple form. Indeed, they can also be derived analytically: If all fuel is assumed to be consumed by the flame, then the heat release rate per flame surface area should be proportional to the fuel mass flux. The fuel mass flux is proportional to the inflow velocity multiplied by the density at the beginning of the flame. The difference in the velocities between the inlet, divided by the flame thickness, defines the mean axial strain rate. As the velocity ratio between fuel and oxidizer is constant, the velocity at the beginning of the flame is directly proportional to the strain rate multiplied by the flame thickness. Using Equation (6.1), and substituting these relations into each other, Equation (6.3) can be derived [32, 34]:

$$\dot{q}_f \sim \mathring{m}_f = \rho_f \cdot u_f \sim p \cdot a \cdot \delta \sim p \cdot a \cdot \frac{1}{\sqrt{a\ p}} \sim \sqrt{a\ p} \tag{6.6}$$

This relation is in agreement with previous results from counterflow flame simulations in literature [116, 115].

The scaling of the flamelet-integrated emissivities can be explained by evaluating the integration (6.2) itself. This is first presented for the blue radiation. As can be seen from Figure 6.5, the shape of the blue radiation is similar at all pressures and strain rates. The area under the curve, which corresponds to the integral, is under this condition proportional to the product of the peak squared OH concentration $[\mathrm{OH}]^2_{\mathrm{peak}}$ and the width of the profile, which is in turn proportional to the flame thickness $\delta$. Applying the equation of state for ideal gases, the peak OH concentration can be substituted by an expression consisting of the pressure $p$, the mixture-averaged gas constant $R$, the temperature $T$, and the peak mole fraction of OH $X_{\mathrm{OH,peak}}$. Among these, only the pressure changes significantly, while the others are approximately constant. If all of these relations are substituted into each other and only the similarity is considered, Equation (6.5) can be derived:

$$\begin{aligned}[\mathrm{OH}]^2_f &= \int_{-\infty}^{\infty} ([\mathrm{OH}](z))^2\ dz \sim [\mathrm{OH}]^2_{\mathrm{peak}} \cdot \delta \\ &= \left(\frac{p}{R\ T} X_{\mathrm{OH,peak}}\right)^2 \cdot \delta \sim p^2 \cdot \frac{1}{\sqrt{a\ p}} \sim p^{3/2}\ a^{-1/2}\end{aligned} \tag{6.7}$$

Similarly, the flamelet-integrated OH* emissivity can be derived. In addition to the above steps, Equation (4.3) is employed to compute the OH* concentration from the OH concentration and the temperature. Due to the exponential dependency on

the temperature, the change in temperature can no longer be neglected. While the strain rate does not influence the peak temperature far from extinction, an increase in pressure leads to a significant rise. The overall impact of the exponential term can be studied from a zero-dimensional analysis in Cantera: Using Cantera's *equilibrate* method, the adiabatic temperature $T_{\mathrm{ad}}$ of stoichiometric hydrogen-oxygen mixtures can be computed as a function of pressure. If the maximum temperature $T_{\max}$ is assumed to be about the adiabatic flame temperature $T_{\mathrm{ad}}$, the exponential term in Equation (4.3) can be evaluated. It is found that it scales approximately with:

$$\frac{[\mathrm{OH}]^*}{[\mathrm{OH}]} \sim \exp\left(-\frac{h\ c}{k_B\ \lambda\ T_{\max}}\right) \sim \exp\left(-\frac{h\ c}{k_B\ \lambda\ T_{\mathrm{ad}}}\right) \sim p^{0.5} \tag{6.8}$$

Using this information, Equation (6.4) is obtained:

$$\begin{aligned}[\mathrm{OH}^*]_f &= \int_{-\infty}^{\infty} [\mathrm{OH}^*](z)\, dz \sim [\mathrm{OH}^*]_{\mathrm{peak}} \cdot \delta = \frac{p}{R\ T} X_{\mathrm{OH}^*,\mathrm{peak}} \cdot \delta \\ &= \frac{p}{R\ T} X_{\mathrm{OH},\mathrm{peak}} \cdot \exp\left(-\frac{h\ c}{k_B\ \lambda\ T_{\max}}\right) \cdot \delta \sim p \cdot p^{0.5} \cdot \frac{1}{\sqrt{a\ p}} \sim p^1\ a^{-1/2}\end{aligned} \tag{6.9}$$

### 6.2.2. Flamelet-Integrated Correlation of Flamelet Ensembles

After describing the influence of strain rate and pressure on individual flamelets, the subsequent question is whether the integral heat release rate and radiation are correlated for an ensemble of flamelets forming a turbulent flame. Typically, the absolute pressure is approximately constant throughout the ensemble. However, the strain rate of each flamelet along the line of sight varies significantly. From the results presented above for individual flamelets, it is evident that a general direct proportionality between heat release rate and radiation is not given for arbitrary turbulent flames.

As mentioned in Section 2.6, Lauer et al. [82] faced a comparable influence of straining on heat release rate and OH* radiation in premixed counterflow flamelets. Similarly, a general direct proportionality was attested to be false. However, they were able to develop a model-based correction technique to still be able to obtain the heat release rate experimentally from OH* measurements. In this study, the strategy is followed accordingly.

Moreover, the simple dependencies of heat release rate and radiation from strain rate and pressure derived in Section 6.2.1 greatly simplify the procedure. A single line of sight is considered (see Figure 6.6), along which the integrated radiance $L_{\mathrm{LoS}}$ is measured. The task is to obtain the heat release rate $\dot{q}_{\mathrm{LoS}}$ corresponding to the interrogation volume. Within this volume, an ensemble of several flamelets form the turbulent flame. According to Yeung et al. [146], the strain rate in flames is

approximately normally distributed around a mean value $\bar{a}$ for a sufficiently large number of flamelets. If the number of flamelets within the volume is assumed to be $N$, the overall heat release rate $\dot{q}_{\mathrm{LoS}}$ is the sum of the flamelet-integrated heat release rates $\dot{q}_{f,i}$ of all flamelets contained. Using Equation (6.3), $\dot{q}_{f,i}$ can be expressed to be proportional to $a_i^{1/2}\ p_i^{1/2}$. Normally, the pressure $p$ can be assumed to be constant throughout the turbulent flame. By applying the law of large numbers, the sum can be replaced by the number of flamelets multiplied by the expected value of the summands:

$$\dot{q}_{\mathrm{LoS}} = \sum_{i=1}^{N} \dot{q}_{f,i} \sim \sum_{i=1}^{N} a_i^{1/2}\ p_i^{1/2} \approx N \cdot \bar{a}^{1/2} \cdot p^{1/2} \tag{6.10}$$

Correspondingly, this derivation can be performed for the radiances of OH* and the blue radiation, which are again assumed to be proportional to the OH* concentration and the square of the OH concentration, respectively:

$$L_{[\mathrm{OH}^*],\mathrm{LoS}} \sim [\mathrm{OH}^*]_{\mathrm{LoS}} = \sum_{i=1}^{N} [\mathrm{OH}^*]_{f,i} \sim \sum_{i=1}^{N} a_i^{-1/2}\ p_i^{1} \approx N \cdot \bar{a}^{-1/2} \cdot p^{1} \tag{6.11}$$

$$L_{[\mathrm{OH}]^2,\mathrm{LoS}} \sim [\mathrm{OH}]^2_{\mathrm{LoS}} = \sum_{i=1}^{N} [\mathrm{OH}]^2_{f,i} \sim \sum_{i=1}^{N} a_i^{-1/2}\ p_i^{3/2} \approx N \cdot \bar{a}^{-1/2} \cdot p^{3/2} \tag{6.12}$$

Generally, the number of flamelets $N$ is not known. However, by solving Equations (6.11) and (6.12) for $N$ and substituting the results in Equation (6.10), two expressions for the line-of-sight heat release rate can be derived:

$$\dot{q}_{\mathrm{LoS}} \sim \bar{a}\ p^{-1/2}\ L_{[\mathrm{OH}^*],\mathrm{LoS}} = c_{f,[\mathrm{OH}^*]}\ L_{[\mathrm{OH}^*],\mathrm{LoS}} \tag{6.13}$$

$$\dot{q}_{\mathrm{LoS}} \sim \bar{a}\ p^{-1}\ L_{[\mathrm{OH}]^2,\mathrm{LoS}} = c_{f,[\mathrm{OH}]^2}\ L_{[\mathrm{OH}]^2,\mathrm{LoS}} \tag{6.14}$$

These equations represent a formulation to determine the heat release rate from OH* and blue radiation measurements. The correlation factor $c_{f,[\mathrm{OH}^*]}$ and $c_{f,[\mathrm{OH}]^2}$ correspond to the non-linear correlation factor introduced by Lauer et al. [82]. They are also shown as a function of strain rate and pressure in Figure 6.8.

If the strain rate is viewed as an inverse flame thickness (see Figure 3.10), Equations (6.13) and (6.14) can also be explained intuitively: Flames with high strain rate are very thin. If radiation is proportional to the flame thickness, there will be little radiation originating from such a flame, even though there is a certain heat release. Inversely, lowly strained flames are very thick and thus radiate considerably even though they are associated with little heat release. Asymptotically, the latter describes the case of the final products of a globally stoichiometric combustion, which are hot and radiate, but do not release further heat.

Thus, the determination of the heat release rate from radiation measurements in turbulent non-premixed flames is possible in principle. However, there is no

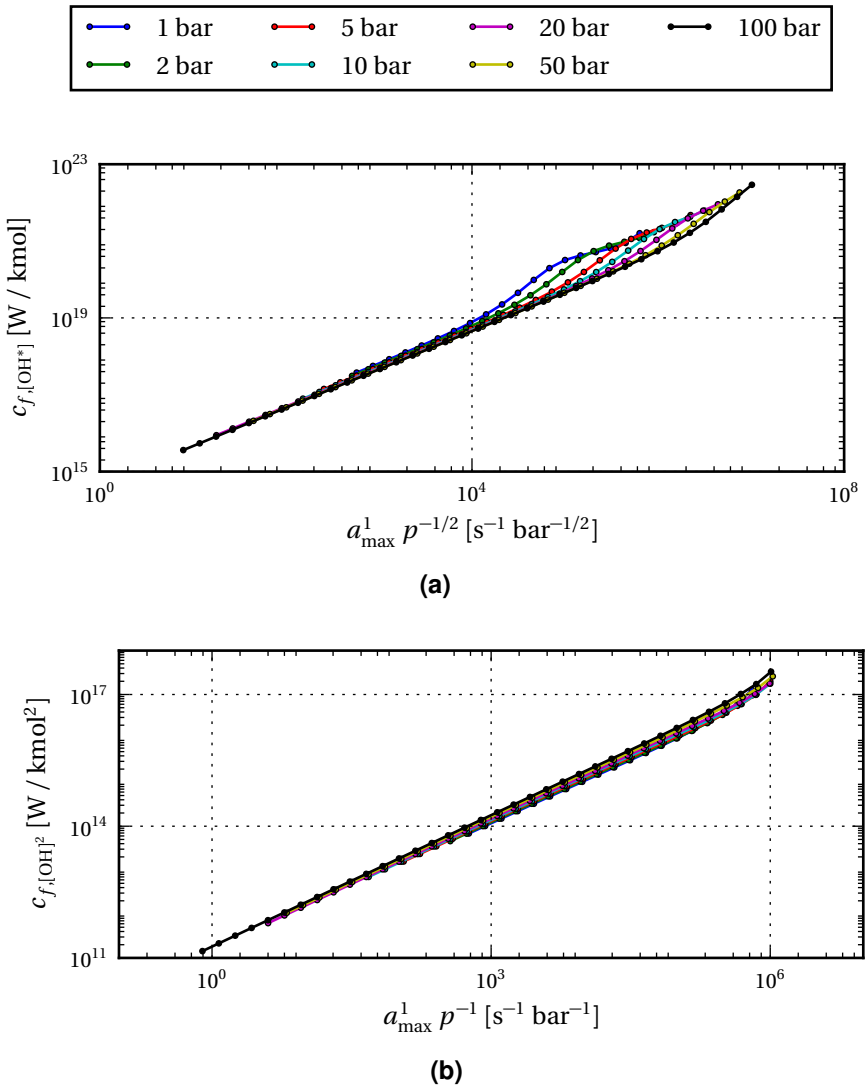


**Figure 6.8.:** Correlation factors between the flamelet-integrated heat release rate and (a) the OH* radiation or (b) the blue radiation, as a function of the maximum strain rate $a_{max}$ and the pressure $p$ (scaled appropriately).

general proportionality. Instead, the radiances have to be weighted accordingly with the mean strain rate $\bar{a}$ of the flamelet ensemble and the pressure $p$.

Practically, the scaling with pressure is achievable in experiments with reasonable effort: Either it is assumed to be constant, or, in the case of large pressure amplitude combustion instability, it can be obtained from pressure field reconstruction [54, 35]. Nevertheless, the measurement of the mean strain rate is more demanding: For example, the steady mean strain rate can be determined from PIV experiments by measuring the Kolmogorov time scale [82]. However, the application of this technique is hardly feasible in confined rocket combustion chambers, especially

if time-resolved measurements are of interest. This imposes a major drawback of using flame radiation as a quantitative marker for the heat release rate.

Additionally, it should be mentioned again that the derivations above are only valid for low optical densities, i.e. negligible self-absorption.

Within the framework of this thesis, no direct experimental proof of this method for turbulent flames was possible. Nevertheless, the results from Lauer et al. [82] generally support the viability of this method. Furthermore, the radiation data of the laminar burner studied in Sections 4.4.3 and 5.2.3 indirectly validate the theory: As the total heat release rate is kept constant throughout all experiments, the strain rate should decrease inversely with pressure (Equation (6.10)). Substituted into Equations (6.13) and (6.14), the total OH* and blue radiation should increase with $p^{3/2}$ and $p^2$, respectively. Although key effects like the flame straining due to gravity and the self-absorption of OH* radiation is neglected in this simple estimation, the results agree by trend with the data presented in Figures 4.12 and 5.4.

## 6.3. Application to Rocket Combustion Instability

As introduced in Chapter 1, the flame is the dominant driving mechanism of thermoacoustic instability. To thoroughly assess the stability of combustion chambers, the understanding of the interaction between combustion and acoustics is essential.

Common approaches to investigate combustion instability are based on the description of the linear acoustic field. By quantifying the growth or decay rate of acoustic perturbations, the stability is characterized. Within the significantly simplified framework of linear acoustics, the impact of combustion can be broken down to its heat release rate. If this theoretically defined quantity could be measured, combustion instability could be studied by evaluating the Rayleigh criterion.

In liquid rocket combustion, flames are always highly turbulent. The previous section showed that for turbulent non-premixed hydrogen-oxygen flames there indeed exists a qualitative correlation between heat release rate and flame radiation, if the medium is optically thin and the combustion is globally non-stoichiometric. Thus, the zones of heat release can be visualized by the zones of radiation.

However, it is also described that there exists no general quantitative relation between heat release rate and flame radiation because of flame straining and pressure influences. Therefore, the simple assumption of direct proportionality between heat release rate and radiation is false in general.

The direct use of radiation measurements for the evaluation of the Rayleigh integral thus would probably generate misleading results. Instead, as derived in the previous section, the radiation measurements must be accompanied by measurements of the mean strain rate along the investigated line of sight as well as the pressure to yield

the quantitative heat release rate. Strictly from theory, for dynamic measurements of fluctuations, even time-resolved strain rate measurements are necessary.

Such a time-resolved measurement of the strain rate distribution is hardly feasible with reasonable measurement effort in rocket combustion chambers, even in model burners far from practical devices. Therefore, it must be concluded that the use of isolated radiation data is insufficient to generally derive the heat release rate and to evaluate the Rayleigh criterion.

This is especially true when different regions of the flame are compared: Numerical simulations show that the strain rate decreases significantly along the flame [113]. Luminous zones close to the injector have a considerably higher associated heat release rate compared to zones at the end of the flames, at which the flame is less strained and, therefore, thicker. However, if only a single spatial region of the flame is studied and only the fluctuation of the heat release rate is of interest, the situation is different: It can be argued that the error that would arise from neglecting of the strain rate correction is of minor importance in this case. If the flame is stationary with respect to the acoustic time scales studied, the strain rate distribution at a certain location is possibly approximately constant. Thus, radiation and heat release would indeed be directly proportional. Following Equations (6.10) through (6.12), both heat release and radiation are dominated by the number $N$ of flamelets contained in the region of interest. Only if the absolute pressure fluctuation is significant, this effect has to be accounted for. Such an assumption obviously is a crude simplification of the flow phenomena. Its validity should be studied experimentally or numerically.

It should not be concluded that radiation measurements are useless. In fact, the opposite is the case: Sometimes, qualitative results are already sufficient, like the characterization of the flame zone for the description of the stratified acoustic field in the combustor. Also, if radiation measurements are not compulsively used to represent the heat release rate, its pure interpretation can be useful. An example is the investigation of the hydrodynamic eigenfrequencies due to flame-injector coupling. These frequencies not only determine the eigenfrequencies of the heat release rate, but also of the flame radiation. Measurements of the fluctuating flame radiation directly provide these eigenfrequencies.

Flame radiation is not only convenient for purely experimental investigations of combustion instability. As of today, model combustors always also serve for the validation of numerical simulations of combustion instability. There is a constant lack of sufficient experimental data, especially information describing the flame. The numerical modeling of the flame is essential to compute reliable Flame Transfer Functions. In the past, radiation data has already been used for validation. However, it is often compared to arbitrary values like the heat release rate or the ground state OH mass fraction [135, 113]. Sections 4.1 and 5.3 show that both OH* and blue radiation can be modeled very accurately in numerical simulations. To perform a

dependable assessment, it is reasonable to compare the measured radiation data with the simulated radiation data.

The methods to simulate OH* and blue radiation presented in Sections 4.1 and 5.3 account for all physically relevant effects in laminar flames, including various excitation modes and self absorption, depending on the specific conditions. However, turbulence-radiation interaction has not been addressed in this study. For example, for OH*, the dominant thermal excitation shows a numerical formulation similar to the equations of Arrhenius-type chemical reactions (Equation (4.3)). The averaging in turbulent flow fields already addressed in Section 4.1.4 affects the applicability in turbulent flames. Nevertheless, since the problem is similar to turbulence-chemistry interaction, standard techniques describing turbulence-chemistry interaction can be adopted. A flamelet-based Large Eddy Simulation can transport emissivities similar to minor species. By performing an appropriate line-of-sight integration in the post-processing, the simulated radiation of turbulent flames can be compared to experimental data for validation.

Additionally, the prominent self-absorption of the OH* radiation described in Section 4.3 can be used effectively to study combustion instability: The discussion on the correlation between heat release rate and radiation in the above paragraphs relies on the results of Section 6.2, for which the postulation of low optical density is essential. In non-premixed hydrogen-oxygen flames, this is the true for the blue radiation and OH* radiation at low pressures. At elevated pressures, the attenuation of OH* within the flame naturally leads the concept of comparing line-of-sight integrated values ad absurdum. Instead, the absorption weights the zones along the line of sight of a detector. As shown in Section 4.3.3, the region closest to the detector dominates the recorded radiance. More important than the emission of this closest region is its absorption, because this determines how much of the background radiation is transmitted. The measurement of OH* radiation at elevated pressure thus gives information about the processes in the near field region of the detector.

Experimentally, the measurement of OH* radiation and blue radiation can be obtained simultaneously. This can be achieved using a spectrograph or, for one-dimensional measurements, by a beam splitter and optical filters. Such a combination yields the maximum of information for the validation of numerical simulations and the investigation of combustion instability.

# 7. Conclusions

In this study, the OH* and the blue radiation of non-premixed hydrogen-oxygen flames are investigated. Results are obtained experimentally from a confined laminar jet flame pressurized up to 40 bar. This data is accompanied by a corresponding CFD simulation and counterflow flame simulations.

For the OH* radiation, the following key findings are obtained:

- The presence of excited OH* molecules in flames typical for liquid rocket combustion is mostly due to thermal excitation. Chemical excitation, which is the origin of chemiluminescence in colder flames, is generally negligible.
- The intensity of OH* radiation emitted by a flame is linearly proportional to the flame volume (area times thickness) and pressure and exponentially dependent on temperature. Self-absorption reduces the emitted radiation.
- In hydrogen-oxygen flames, OH occupies such high mole fractions that it significantly attenuates OH* radiation. This effect becomes more important with increasing pressure.
- The newly developed Equilibrium Filtered Radiation Model (EFRM) provides an efficient post-processing routine to numerically simulate the band-pass filtered OH* radiation. CFD simulations are only required to compute the sufficiently resolved OH and temperature fields. The method yields accurate results at high temperatures and low optical densities.
- To account for the wavelength-dependent self-absorption, OH* radiation must be simulated spectrally. An object-oriented implementation of the HITRAN database [121] is provided for this purpose.

The study of the blue radiation yields the following results:

- Hydrogen-oxygen flames emit a continuous broad-band radiation with a flat maximum in the blue spectrum as reported in literature.
- The blue radiation does not appear to suffer from self-absorption.
- The radiance of the blue radiation increases linearly with flame volume (area times thickness) and with the square of pressure.
- From comparison of the two competing models from literature describing the origin of the blue radiation, it is found that the chemiluminescence reac-

tion OH+OH $\longrightarrow H_2O_2^* \longrightarrow H_2O_2$ describes the experimental observations most accurately. However, it is not proven beyond doubt that this reaction is in fact the source of the blue radiation.

- For the investigated jet flame, the emissivity of the blue radiation can be modeled by the square of the simulated OH concentration.

The comparison between the two types of radiation and the heat release rate is summarized as follows:

- Generally, there exists little connection between the heat release rate and both types of radiation in non-premixed flames.
- Within the laminar flame structure, heat release rate and radiation occur at spatially different locations.
- The reason for the dissimilarity is the different physical origin of both quantities: Radiation originates from the center of the reactive zone, in which both temperature and OH concentration peak. The total amount of flame radiation increases with pressure and is linearly dependent on the flame thickness, which is heavily influenced by flame straining. The heat release rate, on the other hand, leads to the spatial increase in temperature and is present in a much broader region.
- In turbulent flames, in which the spatially resolved laminar flame structure is not important, there still is no quantitative proportionality between the line-of-sight integrated radiation and the heat release rate because of flame straining.
- Self-absorption only affects the line-of-sight integrated radiance but not the line-of-sight integrated heat release rate. Therefore, a direct correlation fails naturally in optically thick media.
- In turbulent flames featuring optically thin media, the line-of-sight integrated heat release rate can be obtained from radiation measurements if it is weighted with the mean strain rate of the flamelets within the probe.

For the investigation of liquid rocket combustion instability with non-stoichiometric mixture ratios, both types of radiation can be used as a qualitative marker for the reaction zone. The difference in the optical densities for the OH* and blue radiation present a possibility to simultaneously study flame surface and the truly line-of-sight integrated radiation. Instead of compulsively correlating it with the heat release rate, combustion instability should be assessed by directly interpreting radiation data. Likewise, numerical simulations can be best validated by comparing the simulated radiation with experimental data.

# Appendix A.

# Assembly Drawings of the Burner

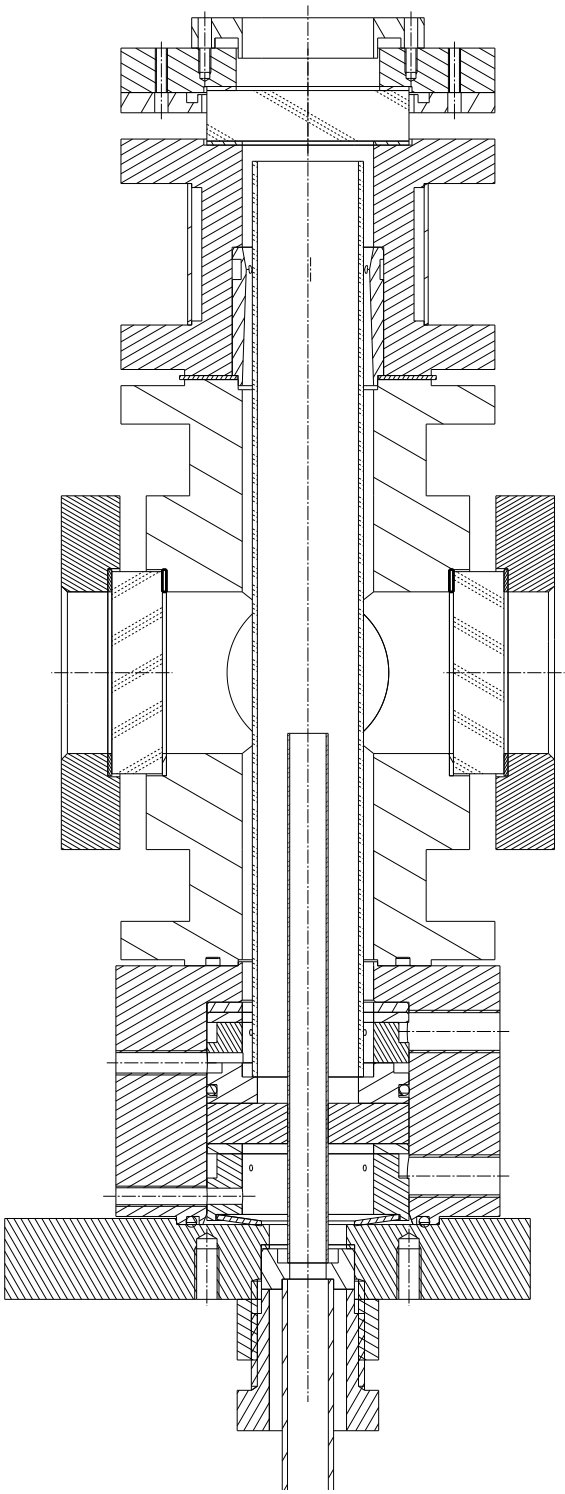

**Figure A.1.:** Cut through the assembly drawing of the high-pressure burner.

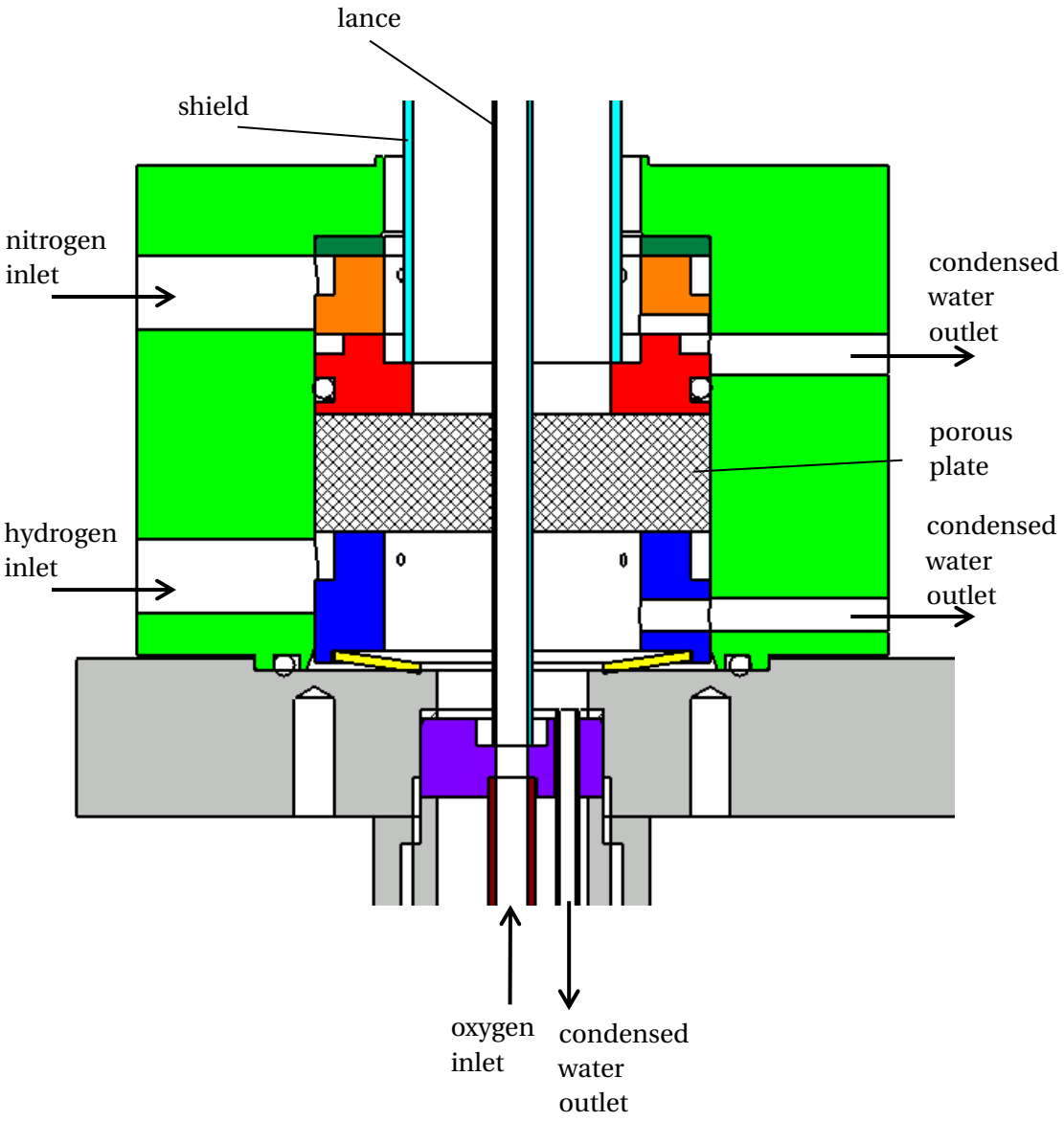


**Figure A.2.:** Cut through the base part of the high-pressure burner. Figure from [87].

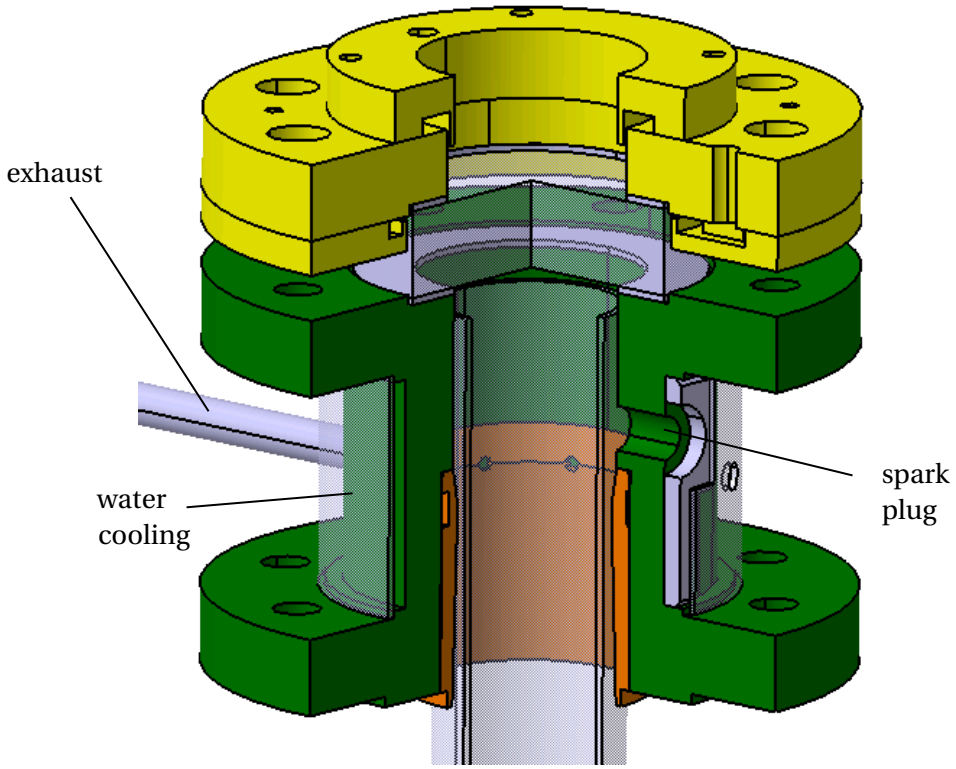


**Figure A.3.:** Cut-away isometric view of the top of the high-pressure burner. Figure from [87].

# Appendix B.

# Data Sheets of the Optical Filters

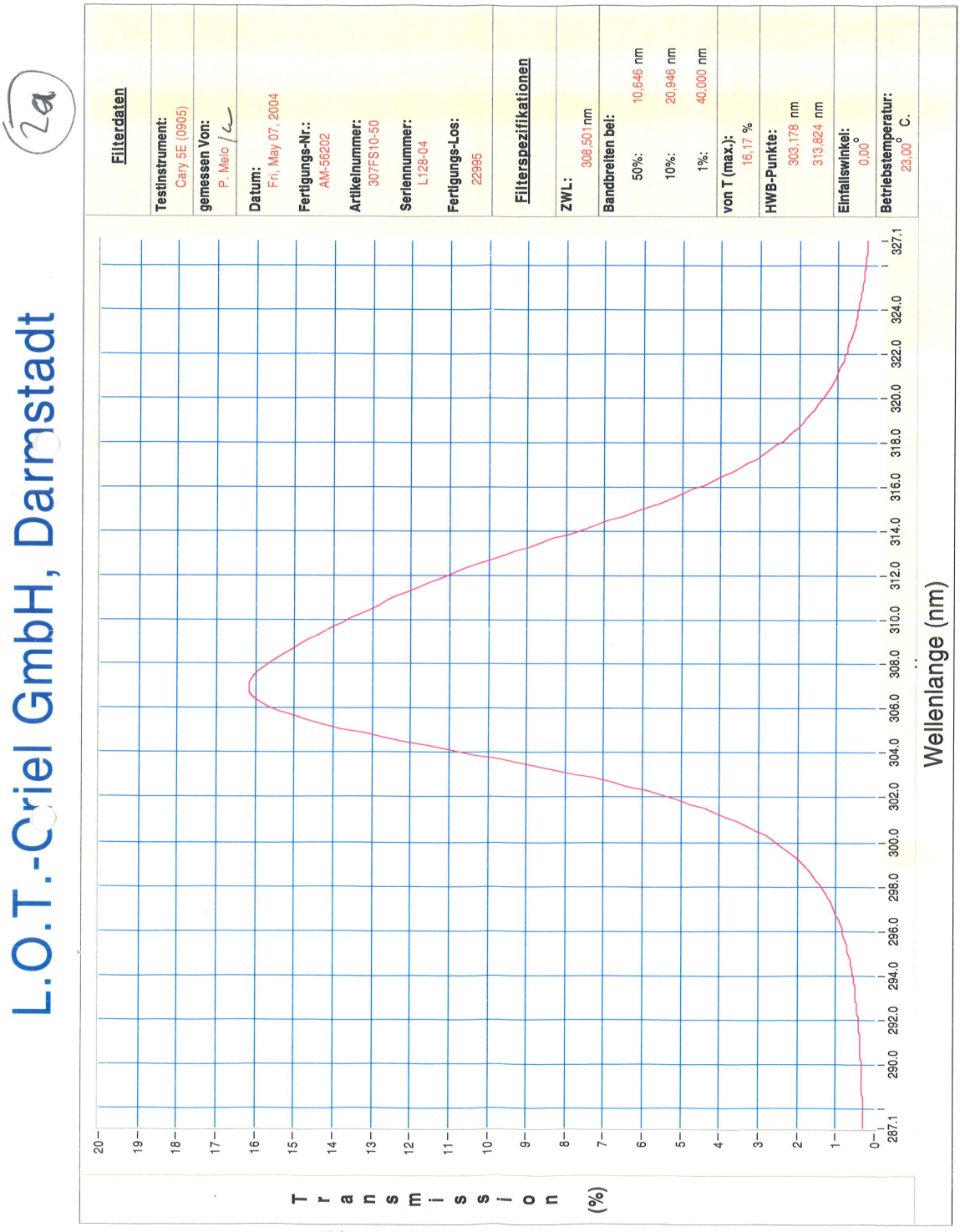


**Figure B.1.:** Spectral transmittance of the 307 nm filter.

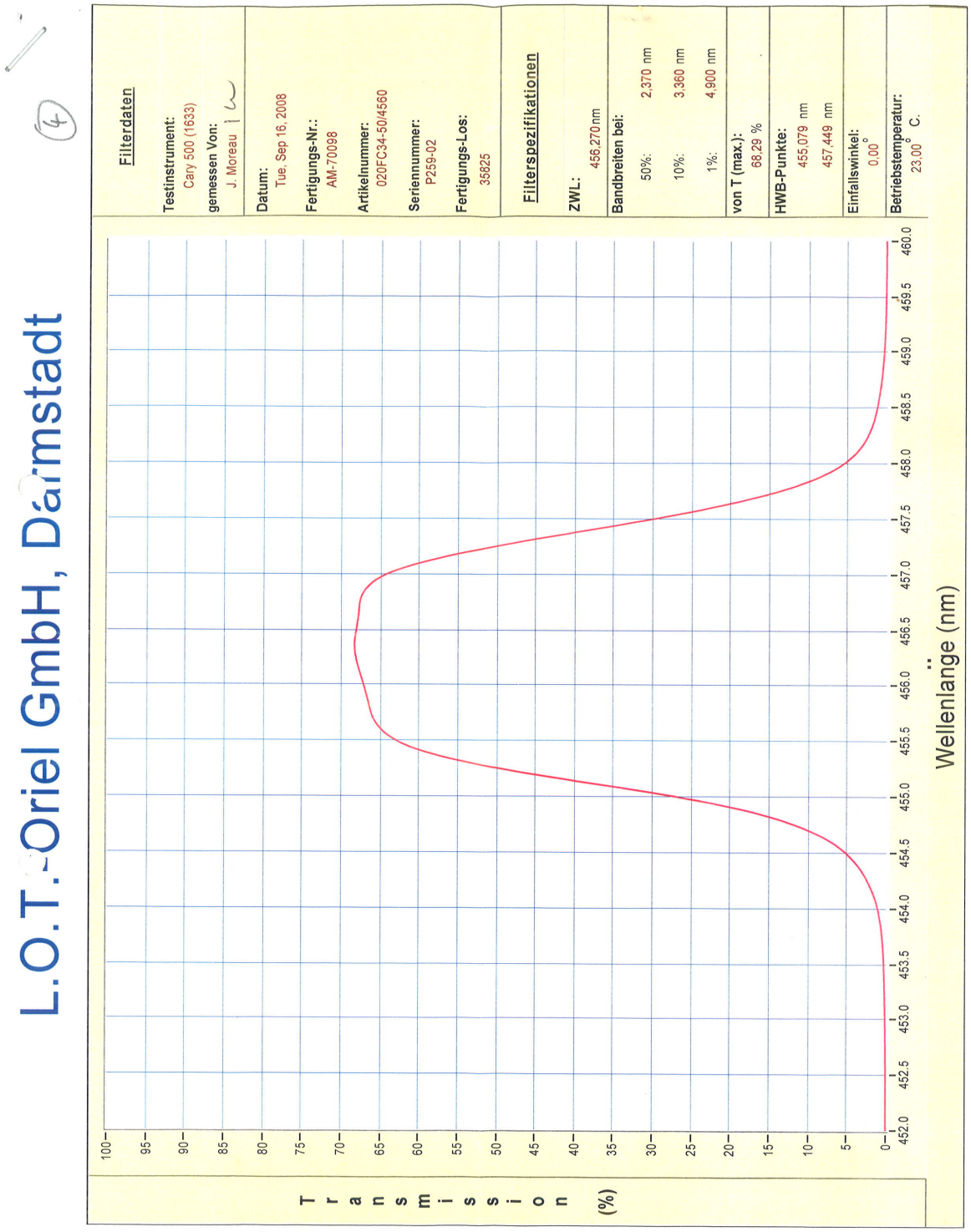


**Figure B.2.:** Spectral transmittance of the 456 nm filter.

# Appendix C.

# Additional Data

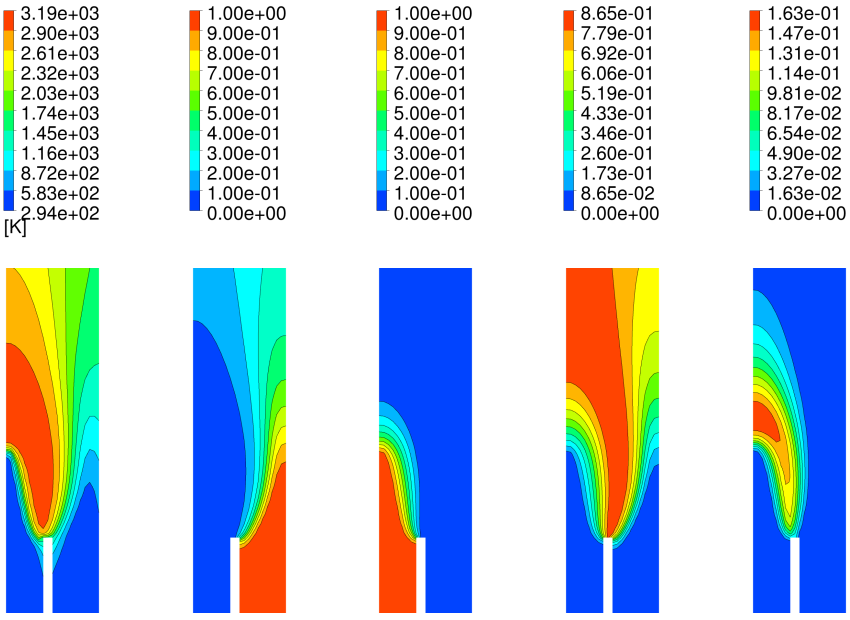


**(a)** Temperature **(b)** $Y_{H_2}$ **(c)** $Y_{O_2}$ **(d)** $Y_{H_2O}$ **(e)** $Y_{OH}$

**Figure C.1.:** Additional jet flame simulation data at 1 bar

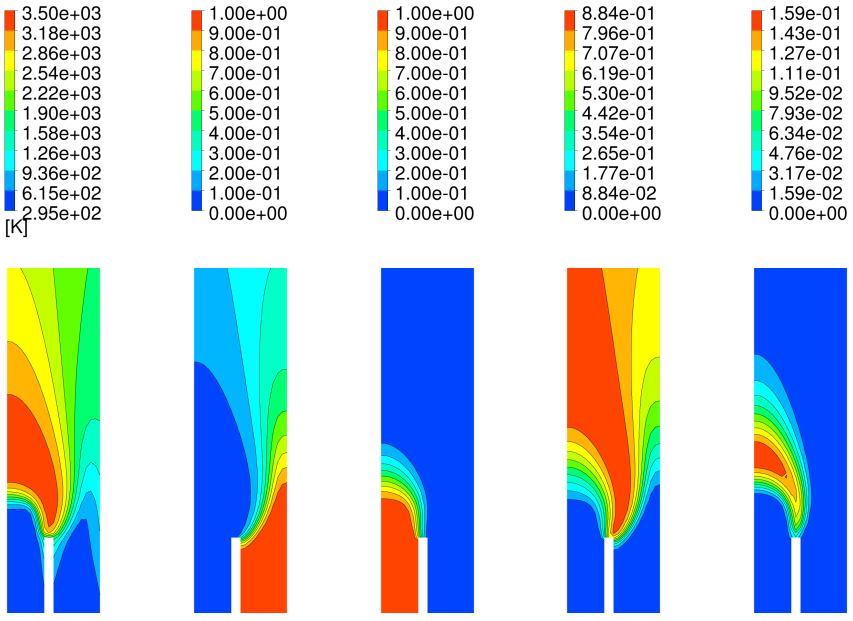


**(a)** Temperature **(b)** $Y_{H_2}$ **(c)** $Y_{O_2}$ **(d)** $Y_{H_2O}$ **(e)** $Y_{OH}$

**Figure C.2.:** Additional jet flame simulation data at 10 bar

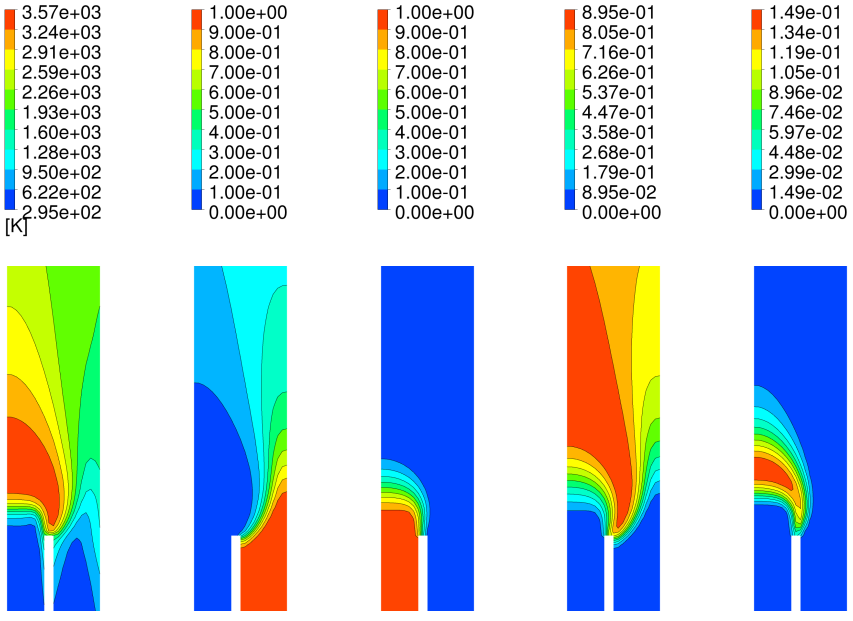


**(a)** Temperature **(b)** $Y_{H_2}$ **(c)** $Y_{O_2}$ **(d)** $Y_{H_2O}$ **(e)** $Y_{OH}$

**Figure C.3.:** Additional jet flame simulation data at 20 bar

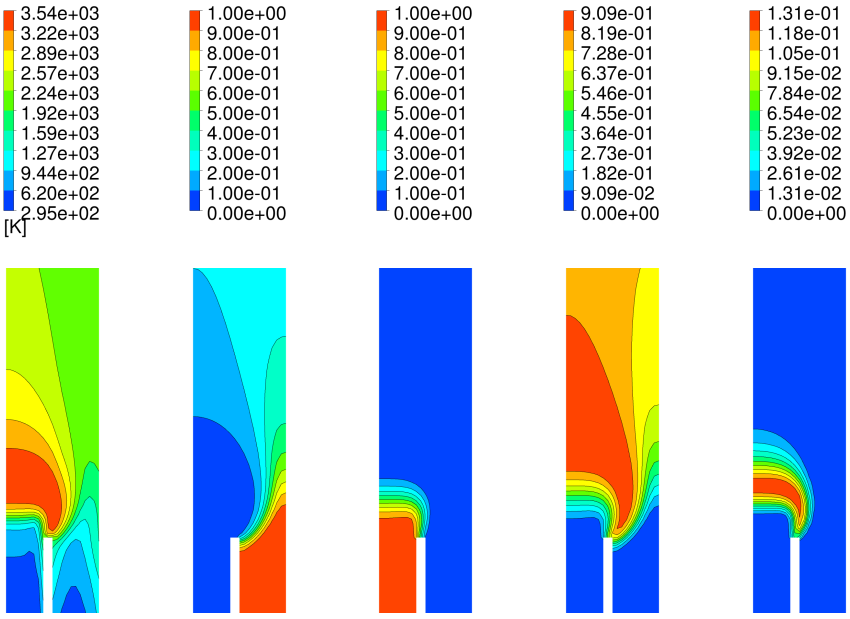


**(a)** Temperature **(b)** $Y_{H_2}$ **(c)** $Y_{O_2}$ **(d)** $Y_{H_2O}$ **(e)** $Y_{OH}$

**Figure C.4.:** Additional jet flame simulation data at 30 bar

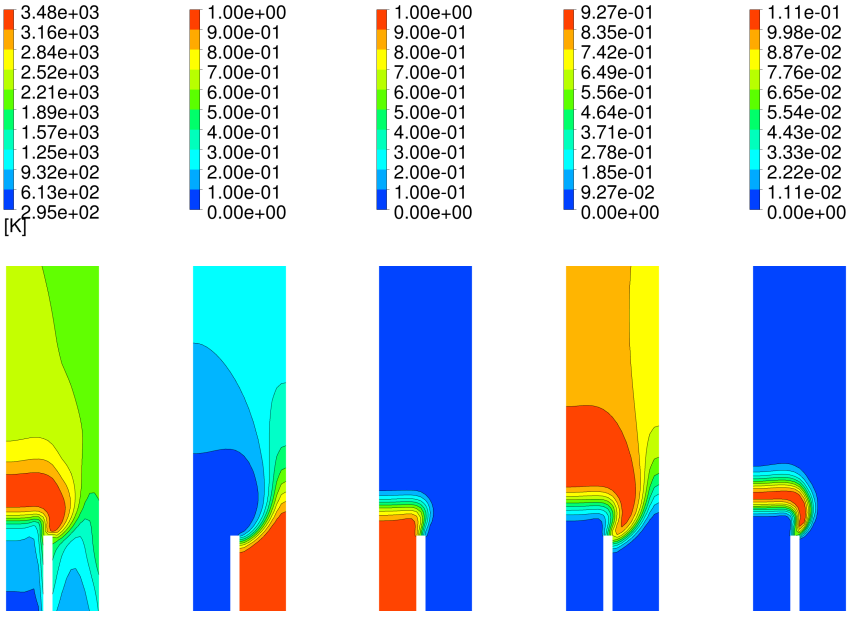


**(a)** Temperature **(b)** $Y_{H_2}$ **(c)** $Y_{O_2}$ **(d)** $Y_{H_2O}$ **(e)** $Y_{OH}$

**Figure C.5.:** Additional jet flame simulation data at 40 bar

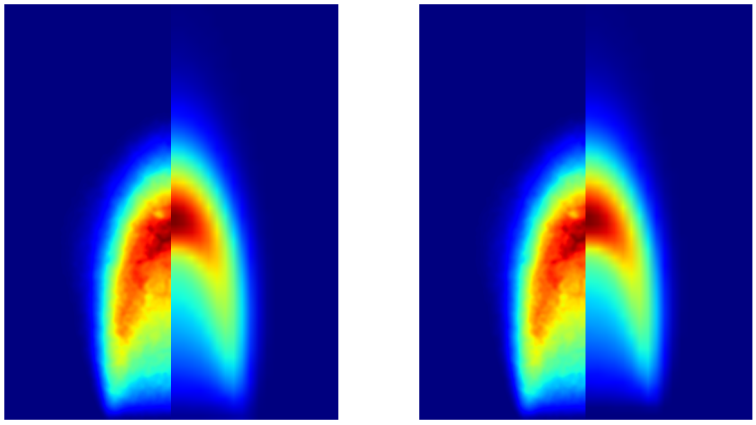

**(a)** Detailed Chemistry



**(b)** EFRM

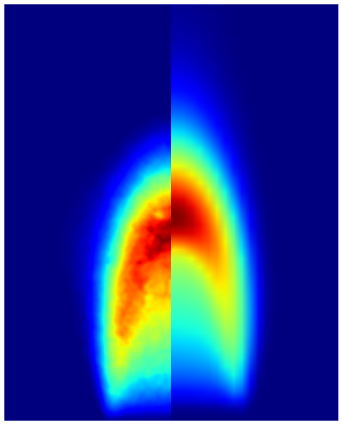

**(c)** Spectral Modeling $L$

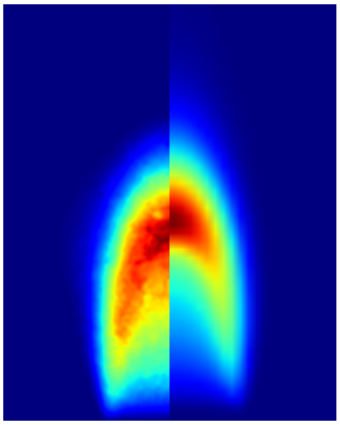

**(d)** Spectral Modeling $e$

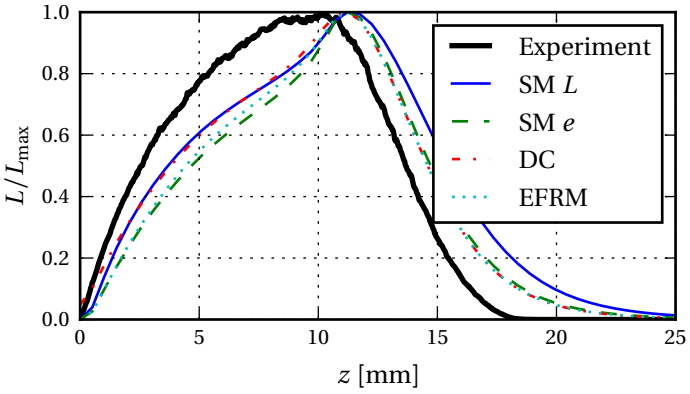


**(e)** Radially integrated radiances over flame height $z$

**Figure C.6.:** Filtered, line-of-sight integrated OH* radiances. Experimental, normalized data is shown on the left sides of the four images. The right sides show the radiance modeling data. Pressure in the experiment: 1 bar, pressure in the simulation: 1 bar.

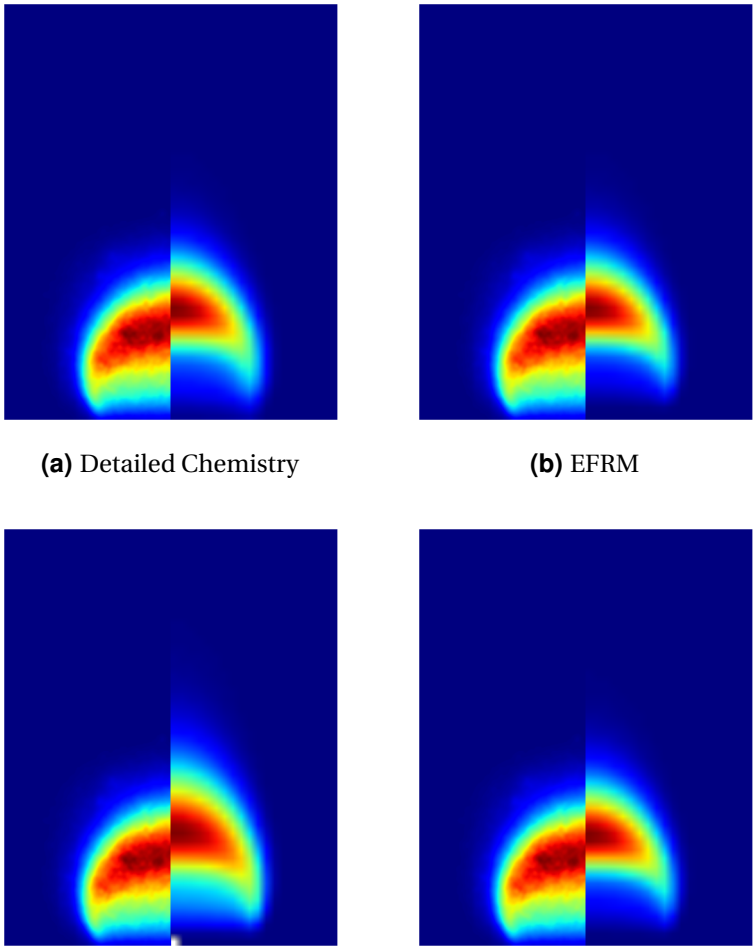

**(a)** Detailed Chemistry

**(b)** EFRM

**(c)** Spectral Modeling $L$

**(d)** Spectral Modeling $e$

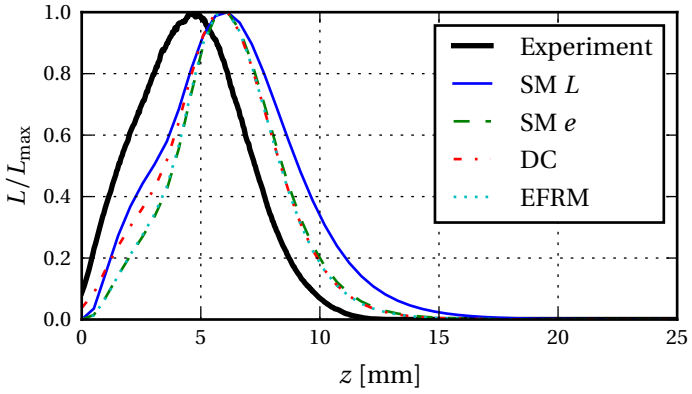


**(e)** Radially integrated radiances over flame height $z$

**Figure C.7.:** Filtered, line-of-sight integrated OH* radiances. Experimental, normalized data is shown on the left sides of the four images. The right sides show the radiance modeling data. Pressure in the experiment: 19.1 bar, pressure in the simulation: 20 bar.

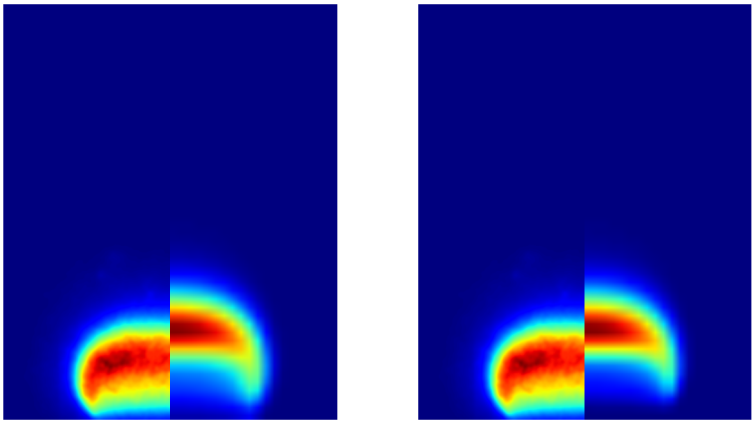

**(a)** Detailed Chemistry



**(b)** EFRM

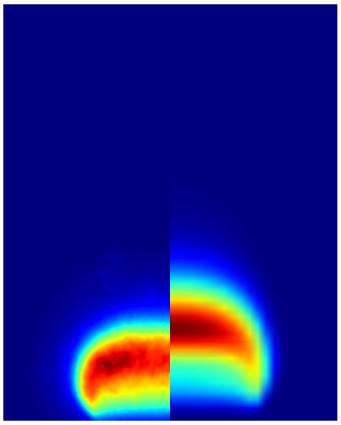

**(c)** Spectral Modeling $L$

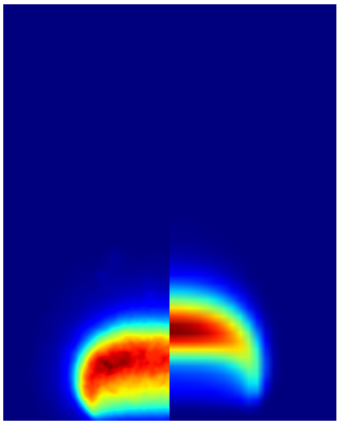

**(d)** Spectral Modeling $e$

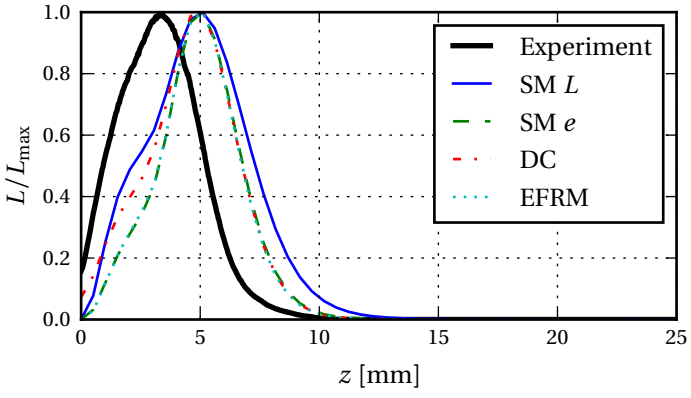


**(e)** Radially integrated radiances over flame height $z$

**Figure C.8.:** Filtered, line-of-sight integrated OH* radiances. Experimental, normalized data is shown on the left sides of the four images. The right sides show the radiance modeling data. Pressure in the experiment: 30.6 bar, pressure in the simulation: 30 bar.

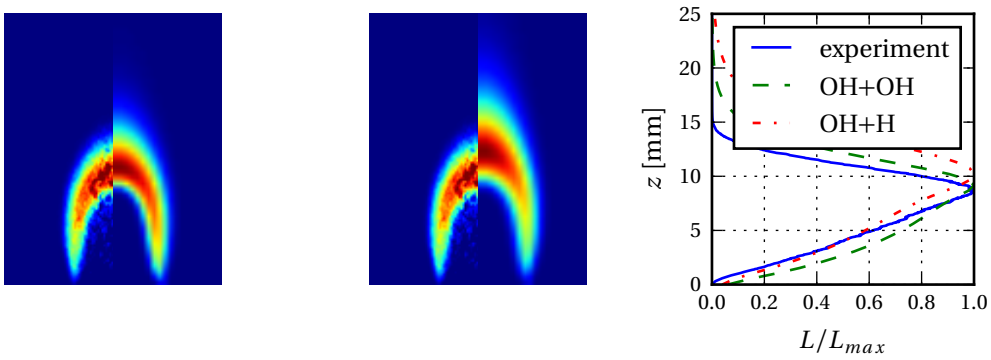


**(a)** Experiment: 5.7 bar, simulation: 5 bar

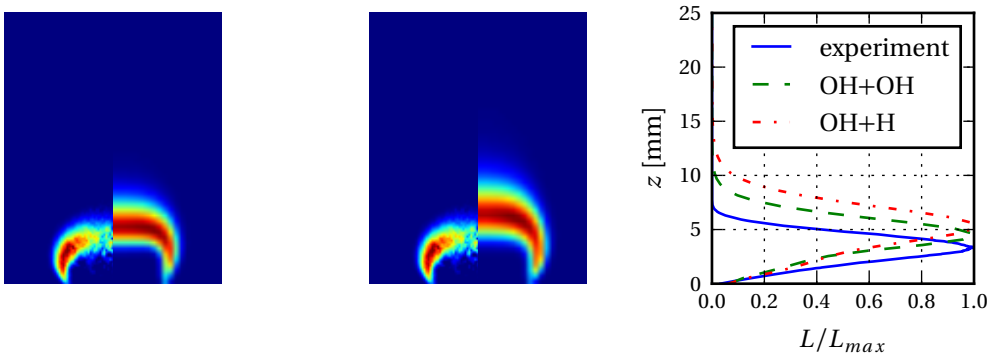


**(b)** Experiment: 29.6 bar, simulation: 30 bar

**Figure C.9.:** Radial distributions of the blue radiation at different pressures. Additional data to Figure 5.5.

## Supervised Theses

Associated with this thesis are a number of student theses (Diplomarbeiten, Bachelors' theses) as well as works performed by student researchers (HiWis, WiHis, internships) that were supervised by the author of the present work. These theses were prepared at the Lehrstuhl für Thermodynamik, Technische Universität München in the years 2011 through 2014 under the close supervision of the present author. Various issues were investigated concerning the radiation of hydrogen flames. Some parts of these supervised works may have been incorporated into the present thesis. The author would like to express his sincere gratitude to all formerly supervised students for their commitment supporting this research project.

| **Student** | **Thesis/Work packages** |
|---|---|
| Druck, Pascal | *Messung der Flammenabsorption mittels TDLAS*, Bachelors' thesis, filed 2014 [30] |
| Hollstein, Kai | *Lab work, ray tracing, radiation modeling*, HiWi, 09/2013–08/2014 |
| Kumar, Abhijeet | *Lab work, spectrum modeling*, IAESTE intern, 10/2013–03/2014 |
| Lieflaender, Markus | *Auslegung und Konstruktion eines Verbrennungsversuchsstands für Hochdruckexperimente*, Diplomarbeit, filed May 28, 2013 [87] |
| Nettinger, Michael | *Berechnung der Strahlungsabsorption in einer eingeschlossenen $H_2$-$O_2$-Flamme*, Bachelors' thesis, filed October 21, 2013 [98] |
| Rieger, Franz | *Experimentelle Bestimmung der Strahlungsabsorption in einer $H_2$-$O_2$-Flamme*, Bachelors' thesis, filed October 31, 2013 [117] |
| Rücker, Andreas | *Implementation of a Radiation Model in an one dimensional Flame Simulation in Cantera*, Bachelors' thesis, filed September 25, 2013 [122] |

# Bibliography


[1] *VDI Wärmeatlas*. Springer Berlin / Heidelberg, 10 edition, 2006.

[2] A. K. Agrawal, S. M. Cherry, and S. R. Gollahalli. Effects of Buoyancy on Steady Hydrogen Gas-jet Diffusion Flames. *Combustion Science and Technology*, 140(1):51 – 68, 1998. doi: 10.1080/00102209808915767.

[3] *ANSYS FLUENT Theory Guide*. ANSYS, INC., release 14.0 edition, 2011.

[4] P. Atkins and J. de Paula. *Physical Chemistry*. Oxford University Press, 10th edition, 2014.

[5] B. Ayoola, R. Balachandran, J. Frank, E. Mastorakos, and C. Kaminski. Spatially resolved heat release rate measurements in turbulent premixed flames. *Combustion and Flame*, 144(1-2):1 – 16, 2006. ISSN 0010-2180. doi: 10.1016/j.combustflame.2005.06.005.

[6] A. E. Bailey, D. E. Heard, P. H. Paul, and M. J. Pilling. Collisional quenching of OH ($A\,^2\Sigma^+$, $v' = 0$) by $N_2$, $O_2$ and $CO_2$ between 204 and 294 K. Implications for atmospheric measurements of OH by laser-induced fluorescence. *Journal of the Chemical Society, Faraday Transactions*, 93:2915–2920, 1997. doi: 10.1039/A701582H.

[7] M. J. Bedard, S. V. Sardeshmukh, T. Fuller, W. E. Anderson, and M. Tanabe. Chemiluminescence as a diagnostic in studying combustion instability in a practical combustor. In *50th AIAA/ASME/SAE/ASEE Joint Propulsion Conference*. American Institute of Aeronautics and Astronautics, 2014. doi: 10.2514/6.2014-3660.

[8] F. E. Belles and M. R. Lauver. Origin of OH Chemiluminescence during the Induction Period of the H2–O2 Reaction behind Shock Waves. *The Journal of Chemical Physics*, 40(2):415–422, 1964. doi: 10.1063/1.1725129.

[9] R. Bleekrode. *Absorption and emission spectroscopy of $C_2$, CH and OH in low-pressure oxyacetylene flames*. PhD thesis, University of Amsterdam, 1967.

[10] U. Boltendahl. *Spektroskopische Bestimmung der Temperatur- und OH-Konzentrationsverteilung in einer laminaren H2-O2-Diffusionsflamme*. PhD thesis, RWTH Aachen, 1974.

[11] J. Boulanger. Laminar round jet diffusion flame buoyant instabilities: Study on the disappearance of varicose structures at ultra-low Froude number.

*Combustion and Flame*, 157(4):757 – 768, 2010. ISSN 0010-2180. doi: 10.1016/j.combustflame.2009.12.005.

[12] A. Brockhinke, J. Krüger, M. Heusing, and M. Letzgus. Measurement and simulation of rotationally-resolved chemiluminescence spectra in flames. *Applied Physics B: Lasers and Optics*, 107(3):539–549, 2012. ISSN 0946-2171. doi: 10.1007/s00340-012-5001-1.

[13] I. N. Bronstein, K. A. Semendjajew, G. Musiol, and H. Mühlig. *Taschenbuch der Mathematik*. Verlag Harri Deutsch, 6 edition, 2005. ISBN 3-8171-2006-0.

[14] A. Bülter, U. Lenhard, U. Rahmann, K. Kohse-Höinghaus, and A. Brockhinke. LASKIN: Efficient simulation of spectra affected by energy transfer. In *Laser Applications to Chemical and Environmental Analysis*. Optical Society of America, 2004.

[15] A. Burcat and B. Ruscic. Third Millennium Ideal Gas and Condensed Phase Thermochemical Database for Combustion with Updates from Active Thermochemical Tables. Technical Report ANL-05/20, Argonne National Laboratory, 2005.

[16] S. P. Burke and T. E. W. Schumann. Diffusion Flames. *Industrial amp; Engineering Chemistry*, 20(10):998–1004, 1928. doi: 10.1021/ie50226a005.

[17] M. C. Burrows. Radiation processes related to oxygen-hydrogen combustion at high pressures. *Symposium (International) on Combustion*, 10(1):207 – 215, 1965. ISSN 0082-0784. doi: 10.1016/S0082-0784(65)80165-5. Tenth Symposium (International) on Combustion.

[18] M. C. Burrows and L. A. Povinelli. Emission spectra from high-pressure hydrogen-oxygen combustion. Technical Report NASA-TN-D-1305, NASA Lewis Research Center, jul 1962.

[19] M. C. Burrows and R. Razner. Relation of emitted ultraviolet radiation to combustion of hydrogen and oxygen at 20 atmospheres. Technical Report NASA-TN-D-2548, NASA Glenn Research Center, dec 1964.

[20] M. Charest, C. Groth, and Ö. Gülder. Effects of Pressure and Gravity in Laminar Coflow Ethylene Diffusion Flames. In *49th AIAA Aerospace Sciences Meeting including the New Horizons Forum and Aerospace Exposition*, number 412. American Institute of Aeronautics and Astronautics, 2011. doi: 10.2514/6.2011-412.

[21] M. Charton and A. G. Gaydon. Excitation of Spectra of OH in Hydrogen Flames and Its Relation to Excess Concentrations of Free Atoms. *Proceedings of the Royal Society of London. Series A. Mathematical and Physical Sciences*, 245(1240):84–92, 1958. doi: 10.1098/rspa.1958.0068.

[22] T. P. Clark and D. A. Bittker. A Study of the Radiation from Laminar and

Turbulent Open Propane-Air Flames as a Function of Flame Area, Equivalence Ratio, and Fuel Flow Rate. Technical Report RM E54F29, NASA Lewis Flight Propulsion Laboratory, aug 1954.

[23] T. Daguse, T. Croonenbroek, J. C. Rolon, N. Darabiha, and A. Soufiani. Study of radiative effects on laminar counterflow H2/O2N2 diffusion flames. *Combustion and Flame*, 106(3):271 – 287, 1996. ISSN 0010-2180. doi: 10.1016/0010-2180(95)00251-0.

[24] D. S. Dandy and S. R. Vosen. Numerical and Experimental Studies of Hydroxyl Radical Chemiluminescence in Methane-Air Flames. *Combustion Science and Technology*, 82(1):131 – 150, 1992. doi: 10.1080/00102209208951816.

[25] H. G. Darabkhani and Y. Zhang. Methane Diffusion Flame Dynamics at Elevated Pressures. *Combustion Science and Technology*, 182(3):231 – 251, 2010. doi: 10.1080/00102200903418252.

[26] M. G. Davis, W. K. McGregor, and A. A. Mason. OH chemiluminescent radiation from lean hydrogen-oxygen flames. *The Journal of Chemical Physics*, 61(4):1352–1356, 1974. doi: 10.1063/1.1682059.

[27] J. Diederichsen and H. G. Wolfhard. Spectrographic Examination of Gaseous Flames at High Pressure. *Proceedings of the Royal Society of London. Series A, Mathematical and Physical Sciences*, 236(1204):89–103, 1956. ISSN 00804630. doi: 10.1098/rspa.1956.0114.

[28] G. H. Dieke and H. M. Crosswhite. The ultraviolet bands of OH Fundamental data. *Journal of Quantitative Spectroscopy and Radiative Transfer*, 2(2):97 – 199, 1962. ISSN 0022-4073. doi: 10.1016/0022-4073(62)90061-4.

[29] W. L. Dimpfl and J. L. Kinsey. Radiative lifetimes of OH(A2[Sigma]) and Einstein coefficients for the A-X system of OH and OD. *Journal of Quantitative Spectroscopy and Radiative Transfer*, 21(3):233 – 241, 1979. ISSN 0022-4073. doi: 10.1016/0022-4073(79)90014-1.

[30] P. Druck. *Messung der Flammenabsorption mittels TDLAS*. Bachelor's thesis, Technische Universität München, 2014.

[31] S. Farhat, W. Ng, and Y. Zhang. Chemiluminescent emission measurement of a diffusion flame jet in a loudspeaker induced standing wave. *Fuel*, 84 (14–15):1760 – 1767, 2005. ISSN 0016-2361. doi: 10.1016/j.fuel.2005.03.020.

[32] T. Fiala and T. Sattelmayer. Non-Premixed Counterflow Flame Simulations: Scaling Rules for Fast Batch Simulations. In *Proceedings of the European Combustion Meeting*, number P1-71, 2013. ISBN 9789163721502.

[33] T. Fiala and T. Sattelmayer. A Posteriori Computation of OH* Radiation from Numerical Simulations in Rocket Combustion Chambers. In *5th European*

*Conference for Aeronautics and Space Sciences (EUCASS), Munich*, jul 2013. ISBN 9788494153105. doi: 10.13140/2.1.1852.0966.

[34] T. Fiala and T. Sattelmayer. Nonpremixed Counterflow Flames: Scaling Rules for Batch Simulations. *Journal of Combustion*, page 7, 2014. doi: 10.1155/2014/484372.

[35] T. Fiala, R. Kathan, and T. Sattelmayer. Effective Stability Analysis of Liquid Rocket Combustion Chambers: Experimental Investigation of Damped Admittances. In *Proceedings of the 62nd International Astronautical Congress*, number IAC11-C4.3.11. International Astronautical Federation, 2011. doi: 10.13140/2.1.2866.6243.

[36] T. Fiala, M. Nettinger, F. Rieger, A. Kumar, and T. Sattelmayer. Emission and Absorption Measurement in Enclosed Round Jet Flames. In *16th International Symposium on Flow Visualization, Okinawa, Japan*, number 1138, 2014. doi: 10.13140/2.1.3424.9609.

[37] L. Figura and A. Gomez. Laminar counterflow steady diffusion flames under high pressure (P<=3 MPa) conditions. *Combustion and Flame*, 159(1):142 – 150, 2012. ISSN 0010-2180. doi: 10.1016/j.combustflame.2011.06.013.

[38] W. Finkelnburg. *Kontinuierliche Spektren*, volume 20 of *Struktur und Eigenschaften der Materie*. Springer Berlin Heidelberg, 1938. ISBN 978-3-642-49638-7. doi: 10.1007/978-3-642-49932-6_5.

[39] A. N. Fletcher and C. A. Heller. Chemiluminescence Quenching Terms. *Photochemistry and Photobiology*, 4(6):1051–1058, 1965. ISSN 1751-1097. doi: 10.1111/j.1751-1097.1965.tb09295.x.

[40] E. Frankland. On the Combustion of Hydrogen and Carbonic Oxide in Oxygen under Great Pressure. *Proceedings of the Royal Society of London*, 16: 419–422, 1867. doi: 10.1098/rspl.1867.0089.

[41] E. Freitag, H. Konle, M. Lauer, C. Hirsch, and T. Sattelmayer. Pressure influence on the flame transfer function of a premixed swirling flame. In *ASME Turbo Expo 2006: Power for Land, Sea and Air*, number GT2006-90540 in Proceedings of GT2006. ASME, 2006.

[42] W. C. Gardiner, K. Morinaga, D. L. Ripley, and T. Takeyama. Shock-Tube Study of OH (Sigma — Pi) Luminescence. *Physics of Fluids*, 12(5): I–120–I–124, 1969. doi: 10.1063/1.1692590.

[43] *SpectralCalc manual*. GATS Inc., 2014. URL `http://www.spectralcalc.com`.

[44] A. G. Gaydon and I. Kopp. Predissociation in the spectrum of OH; a reinterpretation. *Journal of Physics B: Atomic and Molecular Physics*, 4(5): 752, 1971. doi: 10.1088/0022-3700/4/5/020.

[45] A. G. Gaydon and H. G. Wolfhard. Spectroscopic Studies of Low-Pressure Flames. V. Evidence for Abnormally High Electronic Excitation. *Proceedings of the Royal Society of London. Series A. Mathematical and Physical Sciences*, 205(1080):118–134, 1951. doi: 10.1098/rspa.1951.0021.

[46] A. G. Gaydon and H. G. Wolfhard. Predissociation in the Spectrum of OH; the Vibrational and Rotational Intensity Distribution in Flames. *Proceedings of the Royal Society of London. Series A. Mathematical and Physical Sciences*, 208(1092):63–75, 1951. doi: 10.1098/rspa.1951.0144.

[47] A. G. Gaydon and H. G. Wolfhard. The Spectrum-Line Reversal Method of Measuring Flame Temperature. *Proceedings of the Physical Society. Section A*, 65(1):19, 1952. doi: 10.1088/0370-1298/65/1/303.

[48] A. G. Gaydon. *Spectroscopy and Combustion Theory*. Chapman Hall, 1942.

[49] A. G. Gaydon. *The Spectroscopy of Flames*. Chapman and Hall, 2nd edition, 1974. ISBN 0412128705.

[50] J. R. Gillis, A. Goldman, G. Stark, and C. P. Rinsland. Line parameters for the $A^2\Sigma^+ - X^2\Pi$ bands of OH. *Journal of Quantitative Spectroscopy and Radiative Transfer*, 68(2):225 – 230, 2001. ISSN 0022-4073. doi: 10.1016/S0022-4073(00)00011-X.

[51] D. G. Goodwin, H. K. Moffat, and R. L. Speth. Cantera: An Object-oriented Software Toolkit for Chemical Kinetics, Thermodynamics, and Transport Processes, 2014. URL `http://cantera.org`. Version 2.2.0.

[52] E. Goos and A. Burcat. *Rate Constant Calculation for Thermal Reactions*, chapter Overview of Thermochemistry and its Application to Reaction Kinetics, pages 1–32. John Wiley Sons, Inc., 2011. ISBN 9781118166123. doi: 10.1002/9781118166123.ch1.

[53] J. F. Grcar, M. S. Day, and J. B. Bell. Conditional and opposed reaction path diagrams for the analysis of fluid-chemistry interactions. Report LBNL-52164, Lawrence Berkeley National Laboratory, 2003.

[54] S. Gröning, M. Oschwald, and T. Sattelmayer. Selbst erregte tangentiale Moden in einer Raketenbrennkammer unter repräsentativen Bedingungen. In *Deutscher Luft- und Raumfahrtkongress*, sep 2012.

[55] D. Gutman, R. W. Lutz, N. F. Jacobs, E. A. Hardwidge, and G. L. Schott. Shock[U+2010]Tube Study of OH Chemiluminescence in the Hydrogen–Oxygen Reaction. *The Journal of Chemical Physics*, 48(12): 5689–5694, 1968. doi: 10.1063/1.1668656.

[56] L. C. Haber, U. Vandsburger, W. R. Saunders, and V. K. Khanna. An Experimental Examination of the Relationship between Chemiluminescent Light Emissions and Heat-release Rate Under Non-Adiabatic Conditions. In

*Proceedings of IGTI*, number 2000-GT-0121. ASME, may 2000.

[57] J. M. Hall and E. L. Petersen. An optimized kinetics model for OH chemiluminescence at high temperatures and atmospheric pressures. *International Journal of Chemical Kinetics*, 38(12):714–724, 2006. ISSN 1097-4601. doi: 10.1002/kin.20196.

[58] Y. Hardalupas and M. Orain. Local measurements of the time-dependent heat release rate and equivalence ratio using chemiluminescent emission from a flame. *Combustion and Flame*, 139(3):188 – 207, 2004. ISSN 0010-2180. doi: DOI: 10.1016/j.combustflame.2004.08.003.

[59] Y. Hardalupas, C. Panoutsos, and A. Taylor. Spatial resolution of a chemiluminescence sensor for local heat-release rate and equivalence ratio measurements in a model gas turbine combustor. *Experiments in Fluids*, 49 (4):883–909, 2010. ISSN 0723-4864. doi: 10.1007/s00348-010-0915-z.

[60] J. S. Hardi. *Experimental Investigation of High Frequency Combustion Instability in Cryogenic Oxygen-Hydrogen Rocket Engines*. PhD thesis, The University of Adelaide, 2012.

[61] D. T. Harrje and F. H. Reardon. *Liquid Propellant Rocket Combustion Instability*. NASA SP-194. Scientific and Technical Information Office, National Aeronautics and Space Administration, Washington, 1972.

[62] R. Herrmann and C. T. J. Alkemade. *Flammenphotometrie*. Springer, Berlin, 1960.

[63] Y. Hidaka, S. Takahashi, H. Kawano, M. Suga, and W. C. Gardiner. Shock-tube measurement of the rate constant for excited hydroxyl(A2.SIGMA.+) formation in the hydrogen-oxygen reaction. *The Journal of Physical Chemistry*, 86(8):1429–1433, 1982. doi: 10.1021/j100397a043.

[64] B. Higgins, M. McQuay, F. Lacas, J. Rolon, N. Darabiha, and S. Candel. Systematic measurements of OH chemiluminescence for fuel-lean, high-pressure, premixed, laminar flames. *Fuel*, 80(1):67 – 74, 2001. ISSN 0016-2361. doi: 10.1016/S0016-2361(00)00069-7.

[65] A. Hossain and Y. Nakamura. A numerical study on the ability to predict the heat release rate using CH* chemiluminescence in non-sooting counterflow diffusion flames. *Combustion and Flame*, 161(1):162 – 172, 2014. ISSN 0010-2180. doi: 10.1016/j.combustflame.2013.08.021.

[66] K.-P. Huber and G. Herzberg. *Molecular Spectra and Molecular Structure - IV. Constants of Diatomic Molecules*. Van Nostrand Reinhold Company, 1979. ISBN 0442233949.

[67] C. J. Jachimowski. An analytical study of the hydrogen-air reaction mechanism with application to scramjet combustion. Technical Report

NASA-TP-2791, L-16372, NAS 1.60:2791, NASA Langley Research Center; Hampton, VA, United States, 1988.

[68] E. Jones, T. Oliphant, P. Peterson, et al. SciPy: Open source scientific tools for Python, 2001–. URL `http://www.scipy.org/`. [Online; accessed 2015-03-04].

[69] H. I. Joo and Ö. L. Gülder. Soot formation and temperature field structure in co-flow laminar methane–air diffusion flames at pressures from 10 to 60 atm. *Proceedings of the Combustion Institute*, 32(1):769 – 775, 2009. ISSN 1540-7489. doi: 10.1016/j.proci.2008.06.166.

[70] A. E. Karataş and Ö. L. Gülder. Soot formation in high pressure laminar diffusion flames. *Progress in Energy and Combustion Science*, 38(6):818 – 845, 2012. ISSN 0360-1285. doi: 10.1016/j.pecs.2012.04.003.

[71] W. E. Kaskan. Abnormal Excitation of OH in $H_2/O_2/N_2$ Flames. *The Journal of Chemical Physics*, 31(4):944–956, 1959. doi: 10.1063/1.1730556.

[72] T. Kathrotia, M. Fikri, M. Bozkurt, M. Hartmann, U. Riedel, and C. Schulz. Study of the H+O+M reaction forming OH*: Kinetics of OH* chemiluminescence in hydrogen combustion systems. *Combustion and Flame*, 157(7):1261 – 1273, 2010. ISSN 0010-2180. doi: 10.1016/j.combustflame.2010.04.003.

[73] R. J. Kee, F. M. Rupley, J. A. Miller, M. E. Coltrin, J. F. Grcar, E. Meeks, H. K. Moffat, A. E. Lutz, G. Dixon-Lewis, M. D. Smooke, J. Warnatz, G. H. Evans, R. S. Larson, R. E. Mitchell, L. R. Petzold, W. C. Reynolds, M. Caracotsios, W. E. Stewart, P. Glarborg, C. Wang, and O. Adigun. *Chemkin Collection*. Reaction Design, release 3.6 edition, 2000.

[74] R. J. Kee, M. E. Coltrin, and P. Glarborg. *Chemically Reacting Flow*. Wiley-Interscience, 2003. ISBN 0471261793.

[75] D. Klimenko, J. Smith, and D. Suslov. Flame-Emission Spectroscopy at High Pressure Combustion in Combustor C. Technical Report DLR-LA-OD-RP 003, DLR Lampoldshausen, 2004.

[76] K. Kohse-Höinghaus. *Laseroptische Verfahren für die quantitative Bestimmung der Konzentration reaktiver Teilchen sowie der Temperatur in Verbrennungssystemen*. Habilitation, Universität Stuttgart, 1991.

[77] T. Koike and K. Morinaga. Further Studies of the Rate Constant for Chemical Excitation of OH in Shock Waves. *Bulletin of the Chemical Society of Japan*, 55(1):52–54, 1982. doi: 10.1246/bcsj.55.52.

[78] A. A. Konnov. Remaining uncertainties in the kinetic mechanism of hydrogen combustion. *Combustion and Flame*, 152(4):507 – 528, 2008. ISSN 0010-2180. doi: 10.1016/j.combustflame.2007.10.024.

[79] M. Kopp, M. Brower, O. Mathieu, E. Petersen, and F. Güthe. $CO_2$* chemiluminescence study at low and elevated pressures. *Applied Physics B*, 107(3):529–538, 2012. doi: 10.1007/s00340-012-5051-4.

[80] M. Lauer. *Determination of the Heat Release Distribution in Turbulent Flames by Chemiluminescence Imaging*. Dissertation, Technische Universität München, 2011.

[81] M. Lauer and T. Sattelmayer. Heat Release Calculation in a Turbulent Swirl Flame from Laser and Chemiluminescence Measurements. In *14th Int Symp on Applications of Laser Techniques to Fluid Mechanics*, jul 2008.

[82] M. Lauer, M. Zellhuber, C. J. Aul, and T. Sattelmayer. Determination of the Heat Release Distribution in Turbulent Flames by a Model Based Correction of OH* Chemiluminescence. In *Proceedings of ASME Turbo Expo 2011*, number GT2011-45105, 2011.

[83] C. K. Law. *Combustion Physics*. Cambridge University Press, 2006. ISBN 0521154219.

[84] J. G. Lee and D. A. Santavicca. Experimental Diagnostics for the Study of Combustion Instabilities in Lean Premixed Combustors. *Journal of Propulsion and Power*, 19(5):735–750, 2003. ISSN 0748-4658.

[85] M. P. Lee, R. Kienle, and K. Kohse-Höinghaus. Measurements of rotational energy transfer and quenching in OH A $^2\Sigma^+$, $v' = 0$ at elevated temperature. *Applied Physics, B*, 58(6):447–457, 1994.

[86] M. D. Leo, A. Saveliev, L. A. Kennedy, and S. A. Zelepouga. OH and CH luminescence in opposed flow methane oxy-flames. *Combustion and Flame*, 149(4):435 – 447, 2007. ISSN 0010-2180. doi: 10.1016/j.combustflame.2007.01.008.

[87] M. Lieflaender. *Auslegung und Konstruktion eines Verbrennungsversuchsstands für Hochdruckexperimente*. Diplomarbeit, Technische Universität München, 2013.

[88] G. D. Liveing and J. Dewar. On the Influence of Pressure on the Spectra of Flames. *Proceedings of the Royal Society of London*, 49:217–225, 1890. ISSN 03701662. doi: 10.1098/rspl.1890.0086.

[89] J. Luque and D. R. Crosley. Transition probabilities in the $A^2\Sigma^+$- $X^2\Pi_i$ electronic system of OH. *The Journal of Chemical Physics*, 109(2):439–448, 1998. doi: 10.1063/1.476582.

[90] J. Luque and D. R. Crosley. *Lifbase 1.9*. SRI International, 1999.

[91] A. E. Lutz, R. J. Kee, J. F. Grcar, and F. M. Rupley. *OPPDIFF: A Fortran Program for Computing Opposed-Flow Diffusion Flames*. Sandia National Laboratories, 1996.

[92] R. Mavrodineanu and H. Boiteux. *Flame Spectroscopy*. John Wiley & Sons, Inc., 1965.

[93] W. Mayer and H. Tamura. Propellant injection in a liquid oxygen/gaseous hydrogen rocket engine. *Journal of Propulsion and Power*, 12(6):1137–1147, 1996. doi: 10.2514/3.24154.

[94] G. Merziger, G. Mühlbach, D. Wille, and T. Wirth. *Formeln + Hilfen zur höheren Mathematik*. Binomi Verlag, Springe, 4th edition, 2004. ISBN 3-923923-35-X.

[95] M. I. Mishchenko. Vector radiative transfer equation for arbitrarily shaped and arbitrarily oriented particles: a microphysical derivation from statistical electromagnetics. *Appl. Opt.*, 41(33):7114–7134, Nov 2002. doi: 10.1364/AO.41.007114.

[96] M. F. Modest. *Radiative Heat Transfer*. Elsevier, 3rd edition, 2013. ISBN 978-0-12-386990-6.

[97] H. N. Najm, P. H. Paul, C. J. Mueller, and P. S. Wyckoff. On the Adequacy of Certain Experimental Observables as Measurements of Flame Burning Rate. *Combustion and Flame*, 113(3):312 – 332, 1998. ISSN 0010-2180. doi: 10.1016/S0010-2180(97)00209-5.

[98] M. Nettinger. *Berechnung der Strahlungsabsorption in einer eingeschlossenen $H_2$-$O_2$-Flamme*. Bachelor's thesis, Technische Universität München, 2013.

[99] V. Nori and J. Seitzman. Chemiluminescence Measurements and Modeling in Syngas, Methane and Jet-A Fueled Combustors. In *45th AIAA Aerospace Sciences Meeting and Exhibit*, 2007. doi: 10.2514/6.2007-466.

[100] V. N. Nori. *Modeling and Analysis of Chemiluminescence Sensing for Syngas, Methane and Jet-A Combustion*. PhD thesis, Georgia Institute of Technology, 2008.

[101] M. Ó Conaire, H. J. Curran, J. M. Simmie, W. J. Pitz, and C. K. Westbrook. A comprehensive modeling study of hydrogen oxidation. *International Journal of Chemical Kinetics*, 36(11):603–622, 2004. doi: 10.1002/kin.20036.

[102] M. Oschwald, editor. *3rd REST Workshop on Combustion Instability Modeling*, mar 2014. French-German Research on High Frequency Combustion Instability.

[103] P. J. Padley. The origin of the blue continuum in the hydrogen flame. *Trans. Faraday Soc.*, 56:449–454, 1960. doi: 10.1039/TF9605600449.

[104] C. Panoutsos, Y. Hardalupas, and A. Taylor. Numerical evaluation of equivalence ratio measurement using OH* and CH* chemiluminescence in premixed and non-premixed methane-air flames. *Combustion and Flame*, 156(2):273 – 291, 2009. ISSN 0010-2180. doi:

10.1016/j.combustflame.2008.11.008.

[105] P. H. Paul. Vibrational Energy Transfer and Quenching of OH A2.SIGMA.+(.nu.'=1) Measured at High Temperatures in a Shock Tube. *The Journal of Physical Chemistry*, 99(21):8472–8476, 1995. doi: 10.1021/j100021a004.

[106] P. Paul. A model for temperature-dependent collisional quenching of OH $A^2\Sigma^+$. *Journal of Quantitative Spectroscopy and Radiative Transfer*, 51(3):511 – 524, 1994. ISSN 0022-4073. doi: 10.1016/0022-4073(94)90150-3.

[107] N. Peters. Laminar diffusion flamelet models in non-premixed turbulent combustion. *Progress in Energy and Combustion Science*, 10(3):319 – 339, 1984. ISSN 0360-1285. doi: 10.1016/0360-1285(84)90114-X.

[108] N. Peters. *Turbulent Combustion*. Cambridge monographs on mechanics. Cambridge University Press, 2000. ISBN 9780521660822.

[109] N. Peters. *Turbulent Combustion*. Cambridge University Press, 2004.

[110] E. Petersen, D. Kalitan, and M. Rickard. Calibration and Chemical Kinetics Modeling of an OH Chemiluminesence Diagnostic. In *39th AIAA/ASME/SAE/ASEE Joint Propulsion Conference and Exhibit*. American Institute of Aeronautics and Astronautics, 2003. doi: 10.2514/6.2003-4493.

[111] E. Petersen, M. Kopp, N. Donato, and F. Güthe. Assessment of current chemiluminescence kinetics models at engine conditions. In *Proceedings of ASME Turbo Expo 2011: Power for Land, Sea and Air*, number GT2011-45914, 2011.

[112] H. Pitsch. *Entwicklung eines Programmpaketes zur Berechnung eindimensionaler Flammen am Beispiel einer Gegenstromdiffusionsflamme*. Diplomarbeit, Rheinisch-Westfälische Technische Hochschule Aachen, 1993.

[113] S. Pohl, M.-M. Jarczyk, and M. Pfitzner. A real gas laminar flamelet combustion model for the CFD-Simulation of LOX/GH2 combustion. In *5th European Combustion Meeting*, number 86, 2011.

[114] T. Poinsot and D. Veynante. *Theoretical and Numerical Combustion*. R.T. Edwards, Inc., 2nd edition, 2005. ISBN 1930217102.

[115] L. Pons, N. Darabiha, and S. Candel. Pressure Effects on Non-Premixed Strained Flames. In *Proceedings of the European Combustion Meeting*, 2007.

[116] G. Ribert, N. Zong, V. Yang, L. Pons, N. Darabiha, and S. Candel. Counterflow diffusion flames of general fluids: Oxygen/hydrogen mixtures. *Combustion and Flame*, 154(3):319 – 330, 2008. ISSN 0010-2180. doi: 10.1016/j.combustflame.2008.04.023.

[117] F. Rieger. *Experimentelle Bestimmung der Strahlungsabsorption in einer*

*$H_2$-$O_2$-Flamme*. Master's thesis, Technische Universität München, 2013.

[118] F. Roper. The prediction of laminar jet diffusion flame sizes: Part I. Theoretical model. *Combustion and Flame*, 29:219 – 226, 1977. ISSN 0010-2180. doi: 10.1016/0010-2180(77)90112-2.

[119] *COSILAB User Manual*. Rotexo, 2010.

[120] L. Rothman, S. Tashkun, S. Mikhailenko, I. Gordon, and Y. Babikov. HITRAN on the Web. 2014. URL `http://hitran.iao.ru/`.

[121] L. Rothman, I. Gordon, A. Barbe, D. Benner, P. Bernath, M. Birk, V. Boudon, L. Brown, A. Campargue, J.-P. Champion, K. Chance, L. Coudert, V. Dana, V. Devi, S. Fally, J.-M. Flaud, R. Gamache, A. Goldman, D. Jacquemart, I. Kleiner, N. Lacome, W. Lafferty, J.-Y. Mandin, S. Massie, S. Mikhailenko, C. Miller, N. Moazzen-Ahmadi, O. Naumenko, A. Nikitin, J. Orphal, V. Perevalov, A. Perrin, A. Predoi-Cross, C. Rinsland, M. Rotger, M. Šimečková, M. Smith, K. Sung, S. Tashkun, J. Tennyson, R. Toth, A. Vandaele, and J. V. Auwera. The HITRAN 2008 molecular spectroscopic database. *Journal of Quantitative Spectroscopy and Radiative Transfer*, 110(9–10):533 – 572, 2009. ISSN 0022-4073. doi: 10.1016/j.jqsrt.2009.02.013.

[122] A. Rücker. *Implementation of a Radiation Model in an one dimensional Flame Simulation in Cantera*. Bachelor's thesis, Technische Universität München, 2013.

[123] R. Schefer, W. Kulatilaka, B. Patterson, and T. Settersten. Visible emission of hydrogen flames. *Combustion and Flame*, 156(6):1234 – 1241, 2009. ISSN 0010-2180. doi: 10.1016/j.combustflame.2009.01.011.

[124] H. F. R. Schöyer. *Combustion Instability in Liquid Rocket Engines*. European Space Agency, 1993.

[125] G. P. Smith, D. M. Golden, M. Frenklach, N. W. Moriarty, B. Eiteneer, M. Goldenberg, C. T. Bowman, R. K. Hanson, S. Song, W. C. Gardiner, V. V. Lissianski, and Z. Qin. GRI-Mech 3.0. 2000. URL `http://www.me.berkeley.edu/gri_mech/`.

[126] G. P. Smith, J. Luque, C. Park, J. B. Jeffries, and D. R. Crosley. Low pressure flame determinations of rate constants for OH(A) and CH(A) chemiluminescence. *Combustion and Flame*, 131(1-2):59 – 69, 2002. ISSN 0010-2180. doi: 10.1016/S0010-2180(02)00399-1.

[127] G. P. Smith, C. Park, and J. Luque. A note on chemiluminescence in low-pressure hydrogen and methane-nitrous oxide flames. *Combustion and Flame*, 140(4):385 – 389, 2005. ISSN 0010-2180. doi: 10.1016/j.combustflame.2004.11.011.

[128] SpectralFit, S.A.S. *specair 3.0 User manual*, 2012.

[129] J. A. Stone and J. H. Zimmerman. Index of Refraction of Air. 2011. URL `http://emtoolbox.nist.gov/Wavelength/Documentation.asp`.

[130] N. Sullivan, A. Jensen, P. Glarborg, M. S. Day, J. F. Grcar, J. B. Bell, C. J. Pope, and R. J. Kee. Ammonia conversion and NOx formation in laminar coflowing nonpremixed methane-air flames. *Combustion and Flame*, 131(3):285 – 298, 2002. ISSN 0010-2180. doi: 10.1016/S0010-2180(02)00413-3.

[131] P. B. Sunderland, Z.-G. Yuan, and D. L. Urban. Shapes of Buoyant and Nonbuoyant Methane Laminar Jet Diffusion Flames. In *Fourth International Microgravity Combustion Workshop*, pages 129–134, 1997.

[132] P. B. Sunderland, J. E. Haylett, D. L. Urban, and V. Nayagam. Lengths of laminar jet diffusion flames under elevated gravity. *Combustion and Flame*, 152(1-2):60 – 68, 2008. ISSN 0010-2180. doi: 10.1016/j.combustflame.2007.08.011.

[133] M. Tamura, P. A. Berg, J. E. Harrington, J. Luque, J. B. Jeffries, G. P. Smith, and D. R. Crosley. Collisional Quenching of CH(A), OH(A), and NO(A) in Low Pressure Hydrocarbon Flames. *Combustion and Flame*, 114(3-4):502 – 514, 1998. ISSN 0010-2180. doi: 10.1016/S0010-2180(97)00324-6.

[134] K. A. Thomson, Ö. L. Gülder, E. J. Weckman, R. A. Fraser, G. J. Smallwood, and D. R. Snelling. Soot concentration and temperature measurements in co-annular, nonpremixed CH4/air laminar flames at pressures up to 4 MPa. *Combustion and Flame*, 140(3):222 – 232, 2005. ISSN 0010-2180. doi: 10.1016/j.combustflame.2004.11.012.

[135] A. Török, J. Steelant, and T. Sattelmayer. CFD modelling concept for the computation of dynamic heat release in rocket motors. In *Space Propulsion, San Sebastian*, 2010.

[136] S. R. Turns. *An introduction to combustion: concepts and applications*. Mechanical Engineering Series. McGraw Hill, 2000.

[137] M. Vanpee and R. Mainiero. The spectral distribution of the blue hydrogen flame continuum and its origin in hydrogen-nitric oxide flames. *Combustion and Flame*, 34(0):219 – 230, 1979. ISSN 0010-2180. doi: 10.1016/0010-2180(79)90097-X.

[138] M. Wade. Encyclopedia Astronautica. 2014. URL `http://www.astronautix.com/lvs/v2.htm`.

[139] X. Wang, H. Huo, and V. Yang. Supercritical Combustion of General Fluids in Laminar Counterflows. In *51st AIAA Aerospace Sciences Meeting*, number AIAA 2013-1165. American Institute of Aeronautics and Astronautics, 2013. doi: 10.2514/6.2013-1165.

[140] H. Wäsle, A. Winkler, M. Lauer, and T. Sattelmayer. Combustion noise

modeling using chemiluminescence data as indicator for the heat release distribution. In T. C. Institute, editor, *European Combustion Meeting (ECM2007), Chania, Greece*, 2007.

[141] H. Watanabe and K. K. Kendall. Flame Spectrograms: I. Common Metals. *Appl. Spectrosc.*, 9(3):132–140, Aug 1955.

[142] M. Wierman, N. Nugent, and W. Anderson. Combustion response of a LOX/LCH4 element to transverse instabilities. In *47th AIAA/ASME/SAE/ASEE Joint Propulsion Conference & Exhibit*. American Institute of Aeronautics and Astronautics, 2011. doi: 10.2514/6.2011-5549.

[143] A. Winkler. *Validierung eines Modells zur Vorhersage turbulenten Verbrennungslärms*. PhD thesis, Technische Universität München, 2007.

[144] H. G. Wolfhard and W. G. Parker. A Spectroscopic Investigation into the Structure of Diffusion Flames. *Proceedings of the Physical Society. Section A*, 65(1):2, 1952. doi: 10.1088/0370-1298/65/1/302.

[145] V. Yang and W. E. Anderson, editors. *Liquid Rocket Engine Combustion Instability*, volume 169 of *Progress in Astronautics and Aeronautics*. AIAA, 1995.

[146] P. Yeung, S. Girimaji, and S. Pope. Straining and scalar dissipation on material surfaces in turbulence: Implications for flamelets. *Combustion and Flame*, 79(3-4):340 – 365, 1990. ISSN 0010-2180. doi: 10.1016/0010-2180(90)90145-H.

[147] S. W. Yoo, C. K. Law, and S. D. Tse. Chemiluminescent OH* and CH* flame structure and aerodynamic scaling of weakly buoyant, nearly spherical diffusion flames. *Proceedings of the Combustion Institute*, 29:1663–1670, 2002.